LARGE OPTICS FOR THE NATIONAL IGNITION FACILITY

P. Baisden

January 28, 2015

Disclaimer

This document was prepared as an account of work sponsored by an agency of the United States government. Neither the United States government nor Lawrence Livermore National Security, LLC, nor any of their employees makes any warranty, expressed or implied, or assumes any legal liability or responsibility for the accuracy, completeness, or usefulness of any information, apparatus, product, or process disclosed, or represents that its use would not infringe privately owned rights. Reference herein to any specific commercial product, process, or service by trade name, trademark, manufacturer, or otherwise does not necessarily constitute or imply its endorsement, recommendation, or favoring by the United States government or Lawrence Livermore National Security, LLC. The views and opinions of authors expressed herein do not necessarily state or reflect those of the United States government or Lawrence Livermore National Security, LLC, and shall not be used for advertising or product endorsement purposes.

This work performed under the auspices of the U.S. Department of Energy by Lawrence Livermore National Laboratory under Contract DE-AC52-07NA27344.

LARGE OPTICS FOR THE NATIONAL IGNITION FACILITY

P. A. Baisden, L. J. Atherton, R. A. Hawley, T. A. Land, J. A. Menapace,

P. E. Miller, M. J. Runkel, M. L. Spaeth, C. J. Stolz, T. I. Suratwala, P. J. Wegner,

and L. L. Wong

Lawrence Livermore National Laboratory, Livermore, CA 94450

ABSTRACT

The National Ignition Facility (NIF) laser with its 192 independent laser beams is not only the world's largest laser, it is also the largest optical system ever built. With its 192 independent laser beams, the NIF requires a total of 7648 large-aperture (meter-sized) optics. One of the many challenges in designing and building NIF has been to carry out the research and development on optical materials, optics design, and optics manufacturing and metrology technologies needed to achieve NIF's high output energies and precision beam quality. This paper describes the multiyear, multi-supplier, development effort that was undertaken to develop the advanced optical materials, coatings, fabrication technologies, and associated process improvements necessary to manufacture the wide range of NIF optics. The optics include neodymium-doped phosphate glass laser amplifiers; fused silica lenses, windows, and phase plates; mirrors and polarizers with multi-layer, high-reflectivity dielectric coatings deposited on BK7 substrates; and potassium di-hydrogen phosphate crystal optics for fast optical switches, frequency conversion, and polarization rotation. Also included is a discussion of optical specifications and custom metrology and quality-assurance tools designed, built, and fielded at

supplier sites to verify compliance with the stringent NIF specifications. In addition, a brief description of the ongoing program to improve the operational lifetime (i.e., damage resistance) of optics exposed to high fluence in the 351-nm (3ω) is provided.

I. INTRODUCTION

The National Ignition Facility (NIF) laser is not only the world's largest laser, it is also the largest optical system ever built.[1] Its 192 beams contain 7648 large-aperture optics (~0.5 to 1.0 m) with approximately 85% of these optics are located in the 1ω Main Laser System (MLS) section, while the remaining optics are exposed to predominately 3ω light in the Final Optic Assembly (FOA). This paper describes the multiyear, multi-supplier, development effort that was undertaken to develop the advanced optical materials, coatings, fabrication technologies, and associated process improvements necessary to manufacture the wide range of NIF optics. Also included is a discussion of optical specifications and the custom metrology and quality-assurance tools that were designed, built, and fielded at supplier sites to verify compliance with stringent NIF specifications.[2]

II. OPTICAL LAYOUT OF THE NIF

The optical layout of one of NIF's 192 beamlines is shown schematically in Fig. 1. Each beamline contains a series of xenon (Xe) flashlamp-pumped, neodymium (Nd)-glass amplifiers operating at 1053 nm (1ω). These amplifiers are located in two sections in the main laser: the power amplifier and the multi-pass or main amplifier. The power and multi-pass sections contain up to seven and eleven Nd-glass laser slabs per beamline, respectively. In total, the 192 beamlines of NIF contain 3072 such slabs, each weighing ~42 kg and measuring 46 cm × 81 cm × 4 cm. The slabs are mounted at Brewster's angle to minimize Fresnel surface-reflection losses and to enhance the pump efficiency of the surrounding Xe flashlamps.

The NIF utilizes four passes (i.e., two round trips) through the multi-pass amplifier section within the main laser cavity between laser mirror 1 (LM1) and the polarizer/LM2, which is controlled by a plasma electrode Pockels cell (PEPC) used in combination with a large-

aperture (1-m) polarizer.[3-5] Each of the PEPC apertures contains a 1-cm-thick potassium di-hydrogen phosphate (KDP) crystal optic, called a switch crystal (SC), cut normal to the crystal z-axis. Two spatial filters (the cavity and transport spatial filters) nominally 25 and 60 m in length, respectively, act as image relay telescopes. Using pinholes, these components also act as low-pass filters removing high spatial frequency noise from the propagating beam.[1, 6]

Multi-layer, high-reflectivity, dielectric coatings deposited on BK7 substrates serve as mirrors throughout the NIF. The coating layers are alternating layers of e-beam evaporated hafnia (HfO_2) and silica (SiO_2).[7-9] The mirrors are installed in two main locations on the NIF. The first location is the multi-pass cavity where two mirrors (LM1 and LM2) define the ends of the main amplifier cavity and a third, the LM3 elbow mirror, is paired with the polarizer in the periscope assembly (Fig. 1). The mirror located on the amplifier end of the cavity is a deformable mirror composed of a matrix of 39 precision actuators installed on the rear surface of the substrate.[10] These actuators can modify the surface topography of the mirror to correct for system optical aberrations. The second cavity mirror (LM2) consists of the same multi-layer coating design, but it is deposited on a static substrate. The LM2 mirror is used in conjunction with a fast optical switch, which comprises a polarizer and a PEPC, to direct the beam in or out of the multi-pass amplifier cavity.

The second major location where mirrors are installed is in two large bays called the "switchyards."[1] Mirrors LM4–6, located in the switchyards, along with LM7–8, located in the target bay (Fig. 1), reformat the two-dimensional (2-D) array of 192 output beams of the main laser into the 3-D spherical configuration required by the target chamber. These mirrors also use HfO_2/SiO_2 multi-layer stacks, although the specific design is optimized depending on the use angle of the mirror.[11, 12]

All fused silica and KDP transmissive optics are dip- or spin-coated with antireflection (AR) coatings. The coatings consist of a porous layer of silica nanoparticles;[13-15] they are ~50% porous with an effective refractive index of 1.23 ± 0.02 and have a single-surface transmission of > 99.5% on SiO_2 (n = 1.45) and KDP (n = 1.5).

The NIF target area houses a 10-m-diameter aluminum vacuum target chamber that contains 48 laser entry ports where the FOAs are located. Each FOA consists of a fixed-hardware interface to the target chamber and four integrated optics modules (IOMs) that house the final optics for four (a "quad") of the NIF beamlines. The IOMs are precision opto-mechanical systems that combine a number of critical functions into a single compact package: frequency conversion, focusing, color separation, polarization rotation, diagnostic beam sampling, vacuum isolation, and shielding from debris created by imploding targets. The FOAs accept the amplified 1ω light from the MLS, convert each of the four beams with energy as high as 30 kJ (1ω) separately to the third harmonic (3ω), and focus it with high precision into the target chamber.[1, 16] A schematic diagram of an FOA attached to the NIF target chamber and one of the four IOMs with the final optical components is shown in Fig. 2.

A schematic detailing the final optics contained within an FOA is shown in Fig. 3. The first optic in the FOA is a thick fused silica window called the target chamber vacuum window (TCVW). The TCVW provides vacuum isolation between the interior of the FOA and the surrounding ambient atmosphere. Next, there is a dual-crystal frequency converter that comprises a second harmonic generator (SHG) or doubler crystal and a third harmonic generator (THG) or tripler crystal. The SHG, which is fabricated from KDP, together with the THG, which is fabricated from deuterated-KDP, convert the 1053-nm (1ω) output of the MLS to 351 nm (3ω). The converted (3ω) light then passes through the final focusing lens. This off-axis fused

silica lens is purposely wedged to refract any unconverted 1ω (1053 nm) or 2ω (526.5 nm) light away from the target. The relative sizes of the 3ω, 2ω, and 1ω beams at the target focal plane are shown in the bottom right of Fig. 3. The last optic in the FOA is the fused silica grating debris shield (GDS). The output surface of this optic contains a full-aperture diffraction grating that diffracts ~0.2% of the beam energy to a diagnostic package that is used to measure energy of each beam and pulse shape of at least one beam in each quad. With pulse shape and energy the power can be calculated. The final optic in the beamline is a relatively low-cost optic called the disposable debris shield (DDS). The DDS is used as a physical barrier to protect the high-value optics in the FOA from target debris, radiation, and contamination. The DDSs are mounted in cassettes (10 DDS/beamline). As surface debris, solarization, and damage accumulates during successive target shots, the optical transmission of the DDS is degraded. When the transmission reaches a predetermined threshold, DDSs are automatically removed and replaced using the cassette system without disrupting normal shot operations. The GDS also serves as a backup optic to further protect the upstream optics should a DDS fail.

The FOA is also configured to allow the installation of optics that are designed to condition the beams to meet special user requirements.[17] Many of the NIF experiments require a spatially smoothed, super-Gaussian, far-field spot. These far-field profiles can be produced using a custom designed full-aperture, fused silica optic called a continuous phase plate (CPP). Each CPP is imprinted with a prescribed topology on one of its surfaces and can be installed in either the 1ω or 2ω section of the FOA.[18] Another user-specified optic that participates in beam smoothing in NIF is a "polarization rotator" (PR).

A summary of the optics required for NIF by optic type and key materials of construction is provided in Table I.

To aid the reader, a list of abbreviation and acronyms can be found in Appendix A.

III. OPTICAL SPECIFICATIONS AND METROLOGY AND QUALITY ASSURANCE TOOLS

The NIF, compared to previous high-power solid state laser systems developed at LLNL such as Nova, was designed to push laser technology to the limits of performance where nonlinear optical phenomena are known to occur.[19] Because imperfections in the optical components can lead to problems at certain spatial frequencies such as scatter and beam divergence as well as intensity modulations that undergo non-linear gain, the specification of the optics played a critical role in the design of NIF. In particular, the increased performance requirements for NIF drove not only the need for more detailed information about the spatial frequency of phase errors, but the need for better measurement capabilities and analytic techniques to quantify the spatial frequency content of optical surfaces as well.[20-24] The specifications for NIF optics were established on the basis of experience gained during the design and operation of earlier laser systems (e.g., Janus (1971), Argus (1973), Shiva (1974-76), Novette (1983) Nova (1980-85), and Beamlet (1991-94)) and the use of design tools developed for these laser system between the early 1970s and the early 1990s.[25-27] The wavefront quality of the optics used on these previous large laser systems were specified and measured over only two widely separated spatial frequency regions largely due to the metrology tools available at the time. The first region covered the full aperture and specified the wavefront in terms of the standard aberration parameters: sphere, coma, and astigmatism, etc. (i.e., the low order Zernike terms). The second region was at high spatial frequencies and specified the surface micro-roughness. Fortunately, when the wavefront requirements for the surface figure of NIF optics were being established, a new class of phase-measuring interferometers (PMIs) with mega-pixel

cameras became available. With this new technology it was possible to measure phase aberrations across a continuum of spatial scale lengths (spatial frequencies) ranging from μm to m ($μm^{-1}$ to m^{-1}). Although no single metrology tool could cover the full range, a combination of tools could. For example, the capability of measuring phase aberrations (wavefront quality) over the entire range could be realized using large-aperture PMIs covering the low- to mid-frequency region in combination with small-aperture surface-measuring phase interferometers measuring the high-frequency region. The implementation and scale-up of new metrology technologies enabled the NIF Project to specify wavefront quality and perform metrology on large optics at levels of precision higher than were previously possible.

Further details regarding the design of NIF, the flowdown of requirements that led to the optical specifications, and a discussion of the function of the various optical components can be found in an accompanying paper entitled "Description of the NIF Laser" in this special issue of *Fusion Science and Technology*.[28]

III.A. NIF Optical Specifications

Because of the increased performance requirements for NIF and advancements in optical metrology just described, the wavefront quality of the NIF optics was specified over a continuous range of spatial frequencies from 1×10^2 to 2.5×10^{-3} mm^{-1} as shown in Fig. 4.[26] This range was further subdivided into four separate bands delineated from each other on the basis of the diagnostic instrument that could be used to measure the features in each range. These bands, from low to high spatial frequencies or conversely, from high to low spatial wavelengths are called RMS Gradient, Waviness-1 or power spectral density (PSD-1), Waviness-2 or PSD-2, and Roughness and are described in more detail below. Since the fractional area of the optic that is sampled determines the size of the feature that can be measured, different diagnostic instruments

sample different size regions. For example, the entire optic is tested using a transmitted wavefront measurement when evaluating the root mean square (rms) gradient and PSD-1 specification. Much smaller regions of the surfaces are sampled for evaluation of the PSD-2 or Roughness specifications. For these two, a set of nine samples in a 3×3 array are typically measured on each optical surface. The instruments as well as the size of the sampled region used to measure the various spatial frequency bands for large NIF optics are also shown in Fig. 4.

RMS Gradient (2.5×10^{-3} to 3.0×10^{-2} mm^{-1})

The wavefront quality over this range is specified in terms of a maximum peak-to-valley (P-V) error and a maximum rms phase gradient. For all glass optics, the P-V specification is $< \lambda/3$ and the gradient is $< \lambda/90$/cm measured at $\lambda = 633$ nm. This region controls the spot size at the target plane. The NIF's deformable mirror (LM1 in Fig. 1) located at the end of the multi-pass cavity can fully correct for these wavefront aberrations.

Waviness (3.0×10^{-2} to 8.3 mm^{-1})

In this spatial frequency range, a maximum "waviness" (also called ripple) is defined in terms of a PSD. The PSD represents the square of the phase noise amplitude (nm^2) over a certain spatial frequency (mm^{-1}) and thus has the unusual set of units (nm^2/mm^{-1}) or (nm^2 mm), see Fig. 4. Since no single PMI is capable of spanning this entire PSD spatial frequency region, this region is divided into two parts: Waviness-1 or PSD-1 (3.0×10^{-2} to 0.4 mm^{-1}) and Waviness-2 or PSD-2 (0.4 to 8.3 mm^{-1}).

The waviness (PSD) is defined in two ways. First, the power associated with any given Fourier component (spatial frequency) cannot exceed a certain limit labeled as the "not-to-exceed line" shown in Fig. 5 for finished glass and crystal optics. Second, the integral of the measured PSD over the associated spatial frequency band cannot exceed a given value where the

integral is equivalent to the rms waviness and represents the magnitude of the phase noise over that region. This and other aspects of the data-reduction procedure and associated algorithms have previously been described in detail by Williams.[27]

Physically, the rms and not-to-exceed specifications ensure (1) that the total scattered light due to the waviness in this frequency band does not exceed a given value (the rms phase noise specification does this) and (2) that the quantity of light scattered due to any one spatial frequency is below a fixed value (i.e., there is no "grating effect"). This latter point roughly defines the limiting amplitude at a given spatial frequency beyond which subsequent nonlinear growth in the phase noise becomes unacceptable at high operating intensities.

Roughness (8.3 to 100 mm^{-1})

The fourth spatial frequency band represents the micro-roughness region. This measurement is carried out over nine subapertures (0.5×0.5 mm^2) and specified as an average rms value for the glass optics (BK7 and fused silica optics < 0.4 nm; amplifier slabs < 1.0 nm). For the crystal optics both an average (< 1.5 nm) and a peak (< 2.5 nm) roughness for the nine subapertures is specified.

Additional Specifications for Crystals

The crystals have additional specifications that account for features in the material that naturally occur as a result of the growth process. Specifically, the crystals often show distinct boundaries between the surfaces on which the crystal grows, the "prism" {1,0,0} and "pyramid" {1,1,1} faces.[29, 30] Variations can also occur along a given growth direction due to changes in growth parameters caused by factors such as cation impurity levels, growth rate, rotation speed, etc. Evidence for these boundaries is a measurable "phase jump" when viewed in an interferometer. The magnitude of the allowed phase jump depends on the distance over which it

occurs. A sharp phase change implies a high gradient, which is much more problematic than a slowly varying change (i.e., lower gradient). The NIF crystal growth parameters are controlled to assure that crystals pass the phase jump requirements.

Other Wavefront Specifications

There are several subtle aspects of the NIF optics wavefront specifications that should be mentioned. First, at high intensities the phase noise can grow non-linearly for certain spatial frequencies. Therefore, the effect on the laser performance can be much worse if the rms noise is compressed into one narrow band rather than being spread across the entire spectrum. Consequently, an rms noise limit (i.e., the integral of the measured PSD curve) is specified that is less than the integral under the not-to-exceed line.

Second, the specifications have been formulated to account for the fact that some optics are more difficult to manufacture than others. Therefore, the values of the not-to-exceed parameters and the rms phase noise over certain bands are less stringent for the more difficult optics. The crystals are one example of this. The not-to-exceed limit and rms gradient are somewhat higher to account for the higher gradients in crystals, as previously discussed, as well as the greater level of waviness that is produced by the current state-of-the-art machine tools used to finish the crystals. Another example is the spatial filter lenses; because of the long back-focal lengths of these lenses and the use of small-tool figuring, the wavefront was specified over two regions: the central 85% of the aperture and the outer remaining 15%. The central region is easier to manufacture and is specified to the limits as shown in Fig. 5. The outer area has a less stringent PSD-1 rms requirement (2.7 vs. 1.8 nm) and the not-to-exceed limit is higher ($A = 1.5$ vs. 1.0). The ability to slightly relax the specifications of the more difficult optics gives

considerable cost savings without sacrificing performance. This is because the quality, on average, of all the NIF optics is better than our specifications, as shown in the next section.

III.B. Metrology and Quality Assurance Tools

The production of large NIF optics required the development, construction, and installation of a number of custom optical metrology tools for measuring NIF-size optics. Developing the entire suite of metrology tools for NIF was a tour de force in its own right and was highly dependent on successfully completing prerequisites:

- Scaling-up existing metrology tool technologies such as interferometers and photometers to the required aperture;

- Applying measurement technologies from other arenas such as coordinate measuring machines to profile the surfaces of lenses;

- Adapting existing techniques to the requirements of NIF for tasks such as frequency conversion crystal tuning; and

- Utilizing new measurement techniques such as point diffraction phase shifting interferometry to characterize surface defects.[31]

At the time of NIF commissioning, the suite of metrology and quality-assurance (QA) tools numbered at least 32 separate systems located both at the optic supplier sites and at LLNL. Maintenance of these tools represented a significant capital investment and required a dedicated staff of up to 15 scientists, engineers, and technicians, not including supplier personnel who operated the equipment on a daily basis. The majority of these tools are listed in Table II.

The extensive nature of optic testing using this suite of tools can be seen in Table III, which relates optic type to the typical tests performed.

The centerpieces in the suite of metrology tools were the large-aperture interferometers. These commercial instruments were located at supplier production sites and at LLNL and included two 18–in. aperture units operating at 1064 nm developed by Zygo Corp.; seven 24–in. aperture, phase-shifting units developed by Wyko (Veeco Instruments, Inc) operating in the visible; and three 24-in. aperture, phase-shifting units also developed by Zygo. Every large-aperture optic on the NIF was measured for wavefront distortion using these instruments. Analysis of interferometric data from the different types of interferometers was done using LLNL-developed software. This software started as individual programs that were eventually merged together to accommodate each optic type. The core analysis program is composed of nearly 10,000 lines of code. Individual versions of the code were written for specific high-volume computational needs such as DDS wavefront analysis.

The other critical, high-volume metrology tool was the Crystal Alignment Test System (CATS).[32] This laser-based system was designed and built by LLNL and fielded at the crystal supplier. It determined the peak of the frequency conversion curve for both doubler (SHG) and tripler (THG) crystals relative to the crystal surface with microradian accuracy. This accuracy was required because managing stray light on NIF required that frequency conversion crystals be mounted with limited ability to tune by rocking. During the fabrication process each crystal was measured on the CATS a minimum of three times.

There were also two other high-volume, laser-based, small-beam systems that were used on laser glass slabs, polarizers, and transport mirrors to improve laser-damage resistance as part of the QA effort for NIF: (Ref. 33) the laser glass damage testers (LGDT) and the Large Area Conditioners (LAC). These systems were built around commercially available, pulsed Nd:YAG lasers operating at 1 J/pulse, 30Hz with 10-ns (full-width at half maximum or FWHM) pulse

duration. The beams were delivered to precision x,y stages capable of moving large optics with sub-millimeter precision, and the optics were raster scanned in front of the beam. Since these QA systems were similar in scale and scope with the suite of optical metrology tools, they were included within the metrology operations and maintenance efforts for NIF.

There were two LGDT systems, one at each laser glass supplier. The top-hat output of the lasers was image relayed to the laser glass slab. This gave a beam diameter of a few millimeters so that the maximum achievable beam fluence would cause platinum inclusions greater than a critical size to vaporize. Vaporization would render them benign to subsequent laser exposure. This in turn meant that the slab could reach NIF design fluence without further damage and wavefront degradation. Each slab was scanned at two fluences. A more detailed discussion on fabrication of amplifiers using laser glass is in Section V.A.

The LAC systems operated in much the same way as the LGDT except the beam was propagated to the far-field at the optic plane, also resulting in a millimeter-size beam. This was necessary to achieve the beam fluences required to remove nodular coating defects in a benign fashion and increase the damage resistance to meet NIF design fluences. Each coated optic was raster-scanned two to three times, depending on optic type. Mirror and polarizer production is more fully described in Section V.B.

Because of the small beam diameters associated with each of these systems, raster scan times were long and duty cycles were high. These systems often ran 24 hour per day during the peak of optic production, corresponding to approximately 2.6 million shots per day. The reliability of these systems was reasonably good despite their high throughput and duty cycles. This is shown in Table IV.

As can be seen from the table, the 1.2% unavailability for the interferometers required very little in the way of maintenance. This was in part due to low power lasers and lack of moving parts. In contrast the CATS system required more maintenance because of its precision detectors and motor drives. The LACs and LGDTs consumed the most supplies and required more maintenance because of the high power and moving stages.

Figure 6 shows photographs of a large-aperture, 24-in. Wyko interferometer and a LAC.

IV. NIF OPTICAL MATERIALS AND FABRICATION TECHNOLOGY

Manufacturing NIF optics required an extensive multiyear, optical materials and process development effort that began in 1995. This effort was successful because LLNL partnered with a group of renowned optical materials and optics fabrication companies located around the world. This approach was built upon a 25-year tradition of working closely with the private sector to develop and manufacture optics needed for the high-energy laser systems previously constructed at LLNL starting with Janus (1971) up through and including Nova (1980–85). This same approach that was used during construction of Beamlet (1991–94) and NIF continues today to facilitate the fabrication of spare optical components.[5, 19, 34-36] The reader will recall that Beamlet was the full-scale, single-beam physics prototype laser that was built to demonstrate the laser technology and expected performance of NIF. The suppliers that participated in supplying NIF optics are shown in Fig. 7.

The multiyear, multi-vendor development effort involved four steps: (1) technology development, (2) design and construction of manufacturing facilities, (3) start-up and "pilot" production, and (4) full production. [2] The technology development stage included not only development of the optical materials, advanced manufacturing tools, and processes, but also development, fabrication, and installation of the advanced metrology tools needed to test and

verify the performance of the finished optics (see Section III). During the second step, approximately 150,000 ft^2 of dedicated optics manufacturing space was designed and constructed at the NIF supplier sites. This step also included the installation of advanced processing equipment. During the third step (pilot production) these state-of-the-art facilities were commissioned, and a small percentage (5–10%) of the required NIF optics were manufactured to shakedown and troubleshoot the processes and verify that performance and cost goals could be met. The final step was full production, which included manufacturing the large optics needed for completing NIF at the rate required to meet the commissioning schedule of all 192 NIF beamlines.

The multiyear, multi-supplier effort resulted in major improvements in the bulk properties (e.g., absorption, water content, and homogeneity) of the different materials, the uniformity and damage resistance of multi-layer dielectric coatings, and the surface finishing processes used to fabricate the optics as described in Section V. These improvements translated directly into better optical performance. For example, the optical performance of the 1ω optics significantly exceeded the original design specifications required for the 1ω MLS. This is illustrated in Fig. 8 where the design specifications are compared to typical measured values for the 1ω optics for two critical parameters, the passive optical losses and the cumulative rms gradient.[2] This data clearly shows that optical losses for each of the 1ω optics in the MLS is lower, and in some cases much lower, than the original design criteria. Optical damage in the MLS has been quite low as the result of both careful system design and careful fabrication efforts, as described in a companion paper is this issue entitled "Mechanisms Avoided or Managed for NIF Large Optics."[37] Therefore, only a modest number of optical components in the MLS have been replaced to date. In contrast, the 3ω portion of the laser routinely operates

above the damage threshold of fused silica. To enable operations under such conditions, a number of unique operational and optical processing techniques have been developed that are described in another companion paper in this issue entitled "Optics Recycle Loop Strategy for NIF Operations above the UV Laser Induced Damage Threshold."[38] Of particular note is the use of techniques such as chemical etching and laser annealing of damage sites for the 3ω fused silica optics, both of which significantly improved the damage resistance of the GDS and wedged focus lens (WFL). This resulted in a laser system with an overall performance that meets the original design specifications with respect to optical performance and at the same time is much more tolerant of high fluence 3ω operation.

Section V provides a detailed description of all of the optical components by material type that were required to build the NIF. Included in this section are highlights and discussions of the critical technologies and improvements that were made during the multiyear, multi-supplier development and fabrication effort.

V. NIF OPTICAL COMPONENTS BY MATERIAL TYPE

V.A. Laser Glass Amplifiers

Nd-doped metaphosphate glasses are the preferred gain medium for high-peak-power lasers used for fusion energy research for several reasons. These glasses have a lower non-linear coefficient and thus are less prone to self-focusing; they are manufacturable; they have a saturation fluence that allows efficient energy extraction; and they have adequate optical energy storage density.[5, 26] The NIF currently utilizes 3072 amplifier slabs (16 out of a possible 18 slabs) in each of the 192 beamlines (Fig. 9). The amplifier slabs are made from two commercially available Nd-doped metaphosphate glasses, LHG-8 from Hoya Corporation, USA and LG-770

glass from Schott Glass Technologies. The composition together with the optical, laser, thermal, and mechanical properties of these glasses are listed in Table V.[36, 39]

Fabrication of the laser amplifier slabs was jointly funded by Commissariat à l'énergie atomique et aux énergies alternatives (CEA), which also needed slabs for their planned Laser MegaJoule (LMJ) facility, and by LLNL.[40] Two of the economic challenges were to decrease laser glass cost by a factor of 5 and to increase the slab production rate by a factor of 20 relative to the conventional batch melting fabrication method.

V.A.1 Amplifier Blanks

Economic challenges for NIF laser slabs were achieved while also meeting tight homogeneity and quality requirements for the bulk glass. Meeting these goals led to adoption, for the first time, of a continuous melting technique for production of the phosphate glass needed for the high-energy laser amplifiers; approximately 150 tons of this glass was needed for NIF alone. The LMJ facility required a similar amount of glass. Figure 10 outlines the steps of the continuous pour process that was implemented by both laser glass companies, Hoya and Schott.[36] The viscosity of these glasses becomes adequate for mixing and forming at 1000–1200°C. However, at such temperatures the glass is corrosive to most refractories, hence requiring the use of platinum (Pt)-lined vessels.

The technical improvements needed to make continuous melting successful were the result of a six-year, joint research and development effort between LLNL, Schott, and Hoya. The major technological developments included the following:

1. **Pt-inclusion removal**: Microscopic metallic Pt particles (≤ 10 μm) in the laser glass can absorb laser light and cause fracturing of the glass (laser-induced damage). Research on the formation and dissolution of Pt inclusions led to a redox-controlled process for

minimizing the number and size of inclusions in the glass.[41-44] Specifically, under oxidizing conditions and in the presence of chloride ions, which are formed in-situ by the addition of chlorine containing gases such as Cl_2 or CCl_4, the metallic (Pt^0) is oxidized and dissolves into the glass matrix. Spectroscopic evidence strongly suggests that this is due to the formation of the highly stable hexachloroplatinate ($PtCl_6^{2-}$) anion, where each Pt^{4+} ion is surrounded by six chloride (Cl^-) ions within an octahedrally symmetric coordination sphere.

2. **OH removal**: Hydroxyl (OH) groups in the glass quench the fluorescence of the Nd^{3+} ion and reduce the laser output energy. Research on the chemical mechanism of OH removal (dehydroxylation) using reactive gas bubbling, raw material pre-drying using rotary calciners, and the incorporation of this information into numerical process models led to a 10-fold reduction in the OH content of continuously melted glass (Fig. 11).[45-47]

3. F**racture prevention**: Phosphate laser glasses are prone to fracture due to their low fracture toughness, high coefficient of thermal expansion, and chemical reactivity with moisture at elevated temperatures. The latter is a unique mechanism by which moisture from the environment during annealing diffuses into the glass surface, resulting in a tensile surface layer and hence surface cracking.[48] Finite element heat transport and stress analysis, identification of various stress sources, and research into crack growth led to improvements in the annealing and fabrication processes that eliminate fracturing.[48-50]

4. **Impurity minimization**: Metal-ion impurities (such as Fe^{2+} and Cu^{2+}) at levels $\gtrsim 10$ parts per million (ppm) can increase the optical absorption of the glass above acceptable limits. Analytical techniques, such as inductively coupled plasma mass spectrometry (ICP-MS) were used to quantify impurity levels. This information was combined with research on

the absorption characteristics of these impurities and led to much improved specifications and quality-control procedures for both the laser glass and the raw materials.[52, 53]

5. **Homogeneity**: Laser glass requires a refractive index uniformity (i.e., optical homogeneity) of about 1 ppm, requiring advanced forming technologies.

6. **Metrology and quality assurance (QA)**: A number of unique metrology and quality-assurance tools have been developed to measure and inspect large optical glass plates at a high rate. These tools include large-aperture (24-in.) PMIs used for measuring wavefront quality and laser-based, small-beam systems called laser glass damage testers (LGDT) used to raster-scan laser glass slabs over the full aperture to identify Pt inclusions.[54] A more detailed discussion on these tools is in Section III.B.

The photograph in Fig. 12 (left) depicts a strip of phosphate glass as it exits the coarse annealing lehr of the continuous glass melter at Hoya. Figure 12 (right) is a similar photograph taken at Schott. The total length of glass strips required by NIF is approximately two miles. After coarse annealing and being rough-cut to size, the glass slabs are inspected for Pt inclusions. The slabs are then fine annealed and assessed for residual stress-induced birefringence (typically to < 10 nm/cm). After additional sizing operations each slab is ground and inspection-polished in preparation for its first interferometric measurement of internal homogeneity. The final blank typically has the following internal homogeneity value: power < 0.15λ, astigmatism < 0.11λ, higher orders < 0.07λ, and rms gradient < 0.004 λ/cm measured at 633 nm.[55]

V.A.2 *Amplifier Finishing and Cladding*

Amplifier blanks meeting specifications were then packaged and sent to the finishing supplier, Zygo Corporation. There the edges were first ground to final dimension and after cleaning, the copper-doped edge cladding was applied to each edge using a specially developed

index-matched epoxy adhesive.[56] Following cladding, the faces of each slab were ground to final form and optically polished (see Fig. 13) using the same processes and equipment used to the finish NIF mirrors (see Section V.B.2 for more details). The final transmitted wavefront of the slab met the stringent requirements of P-V of $< \lambda/3$ with an rms gradient of $< \lambda/90/cm$ measured at 633 nm. A final finished amplifier slab undergoing final visual inspection is shown in Fig. 9 (left). In this photograph, the blue-green copper doped cladding is readily visible on the edges of the amplifier slab. The final amplifier slabs have a mass of ~42 kg and measure 46 cm × 81 cm × 4 cm.

V.A.3 Amplifier Weathering

Significant technical advances were made not just for developing a high-yield finishing process (including the cladding attachment process and transmitted wavefront control), but also in developing technologies required to minimize haze on the finished amplifier surface and reduce humidity-induced weathering. Due to the high reactivity of the cerium oxide-polishing slurry with the phosphate glass, even a minute amount of residual slurry left on the final finished optic can result in a reaction at the particle-glass interface, ultimately leading to the formation of shallow (~15-nm deep) pits on the glass surface, which can be observed as haze.[57] Cleaning methods were developed and implemented immediately after the final polishing step to minimize this effect. This in turn significantly reduced the pitting, improved the surface micro-roughness, and reduced optical scattering.

Exposure of the laser phosphate glass to humidity leads to weathering of the glass surface. Weathering is a chemical reaction between H_2O and the phosphate glass surface that leads to scission of the metaphosphate molecular chains.[58] Degradation is caused when the resulting low molecular weight reaction products recrystallize on the surface of the glass. To

prevent degradation of the optical surface due to weathering, each slab was packaged together with a molecular-sieve desiccant in a packaging system designed to protect the integrity of the slab surface for up to 30 years, as might be required for uninstalled spare optics. For the same reason, exposure of the slabs to humidity was minimized during laser assembly and installation operations, and a dry atmosphere is utilized within the NIF amplifier section of the laser itself.

V.A.4 Amplifier Installation in NIF

Each of the 192 NIF beamlines is capable of accommodating up to 18 amplifier slabs, with a maximum of 11 slabs in the main amplifier (MA) and 7 slabs in the power amplifier (PA), see Fig. 14. When installed, the amplifier slabs are mounted at Brewster's angle to minimize Fresnel reflection losses and to enhance the pump efficiency from the surrounding flashlamps. The iconic beamline at the top of Fig. 14 includes the identification of all large 1ω optics in a single NIF beamline. Figure 14 also illustrates the orientation, location, and nomenclature associated with the installed amplifier slab in each beamline. Adjacent slab locations alternate between two mirror-image configurations (referred to as "even" and "odd").

To maximize laser performance, the location of each slab within the amplifiers is optimized.[28] Specific parameters that drive the location of a given amplifier slab include (1) maximizing the amplifier slab life, which could be limited by growth of pre-initiated Pt damage sites in the glass; (2) maintaining a reasonable gain balance between beamlines; and (3) minimizing the beam "walk off". Based on off-line laser testing of Pt damage sites initiated by the QA scanning process, there is a possibility that initiated sites can grow beyond their original post-scan size during subsequent use in the NIF laser. The probability of damage growth increases as a function of laser fluence. Growth of such a site to 3–4 mm could cause an

intensity spike that might initiate damage on downstream optics. In addition, the scattered light

from such damage sites increases the fluence on the low-pass pinhole in the spatial filter and

raises the risk for pinhole closing. The Large Optic Inspection System (LOIS) is used to monitor

Pt damage sites in the slabs; thus, a site that begins to grow can be detected, allowing its host

slab to be replaced before the site grows to a problematic size.[28] To date no slabs have required

replacement due to unacceptable growth of Pt damage sites.

Owing to a small disparity in the emission cross-section of each supplier's amplifier glass

(3.9×10^{-20} cm^2 for LG-770 and 3.6×10^{-20} cm^2 for LHG-8), variations in the number of slabs of

each glass type can result in a beam-to-beam gain variation. To maintain gain balance, a similar

number of slabs of each particular glass type are used in each beamline.

V.B. Mirrors and Polarizers

The NIF has 1408 large-aperture mirrors and 192 polarizers.[8, 59] These mirrors are used in

a number of ways. Laser mirror 1, LM2, and LM3 are essential elements in the multi-pass main

laser cavity; LM1 also provides wavefront correction for the MLS. Laser mirrors 4–8 transport

the 1ω light from the MLS to the target chamber while preserving polarization purity. Laser

mirrors 5 and 8 work in concert to align the beams to the target. Mirrors are as large as 417 mm

$\times$ 807 mm $\times$ 90 mm and are manufactured from BK7 or equivalent materials for a total weight of

84 metric tons and 510 m^2 of surface area. To meet the stringent specifications for these

components, a development and facilitization program occurred in the 1990s so that

manufacturing of the components could commence with a production schedule of 2000 to 2009.

Today, fewer than 3% of the total mirrors are replaced annually to support NIF operations.

Mirrors are used in a few different locations on NIF, as illustrated in Fig. 1. Within the

NIF multi-pass main amplifier section are the deformable mirror (LM1), cavity mirror (LM2),

elbow mirror (LM3) and the polarizer (PL). These optics are located in a dry-air environment that is required to prevent weathering of the amplifier slabs. The transport mirrors are in the switchyard (LM4–6) and the target bay (LM7–8) and are used in an argon environment to minimize stimulated rotational Raman scattering (SRRS).

V.B.1 Mirror and Polarizer Blanks

The mirror and polarizer blanks for NIF were melted using commercial BK7 or equivalent glass. Three suppliers, Ohara, Pilkington, and Schott provided glass blanks for the build and continued operation of NIF. Eighty-four metric tons of glass were continuously poured and fine annealed to meet requirements for inhomogeneity (5 ppm) and stress birefringence (< 5 nm/cm). Although these specifications are more stringent than those of typical mirror blanks, some non-reproducible reflected wavefront changes were observed due to the temperature cycling during e-beam coating. This was overcome by allowing subtraction of up to $\lambda/3$ waves of power in the reflected wavefront after coating measured at 1064 nm. The decollomation that resulted was corrected by a combination of the deformable mirror and the wedged focus lens.

BK7 was selected as the mirror material for three reasons:

1. It is a commodity glass that has a significantly lower cost-per-unit volume compared to fused silica.

2. Its thermal expansion coefficient is approximately 13 times higher than fused silica. This property aids in the manufacture of e-beam coatings that have low coating stress in a low-humidity environment without the risk of crazing of excessively tensile coating stress.

3. It can be darkened by color center formation using gamma radiation for a marginal cost of ~$1000 per mirror blank; the final transport mirrors (LM7 & LM8) must be darkened to absorb backscattered light from the target.

V.B.2 Mirror and Polarizer Finishing

In the mid-1990s Zygo Corporation developed subscale finishing technologies designed to improve the deterministic nature of finishing mirrors and polarizers. By the end of the 1990s Zygo Corporation was facilitized to manufacture meter-size mirrors at a rate of approximately 20 mirrors per month. Deterministic finishing technologies were implemented: computer numerical control (CNC) machines for shaping and edging, electrolytic in-situ dressing (ELID) as a fixed-abrasive grinding step to achieve flatness, high-speed synthetic lap polishing for polish out, and computer-controlled lap polishing for rapid figure convergence.[60]

Computer numerical control machines were used to generate the length and width of the optics. High-fluence coated optics traditionally have polished edges to facilitate cleaning. To minimize cost, ground edges with a translucent finish were examined, and damage tests of coated optics with translucent ground edges were found to meet the fluence requirement of 22 J/cm^2 at 3 ns. With CNC machining, side- and rear-surface pockets were added into the mirrors to facilitate mounting without obstructing any of the mirror surface area.

Before polishing, fixed-abrasive grinding was used to render a mirror blank to very close to its required thickness. It was difficult to generate reproducibly flat surfaces using fixed-abrasive grinding and thus, a manual loose-abrasive grinding step was added to achieve the required figure before polishing began. During fixed-abrasive grinding, the grinding wheel became dull due to the accumulation of swarf (small bits of ground glass) and the wheel required "redressing". Redressing the wheel removed the swarf as well as a thin layer of the metallic matrix, exposing fresh abrasive material (usually diamond particles) for grinding. This constant redressing resulted in non-uniform material removal and inconsistent surface figure.

Electrolytic In-Situ Dressing (ELID) was first developed in Japan on subscale optics.[61] It was successfully scaled up by Zygo to fabricate meter-scale amplifier slabs, mirrors, and polarizers (see Fig. 15). With ELID, a current was applied to the fixed-abrasive wheel to form a surface oxide layer. The surface oxide layer then eroded, preventing the buildup of swarf and constantly exposing fresh diamond particles on the surface of the wheel. This "self-dressing" of the fixed-abrasive wheel resulted in a consistent grinding rate and a predictable surface figure. This eliminated the need for a manual loose-abrasive grinding step.

Once the optic was machined to size and fine ground it was polished. The removal rates during pitch polishing for final figuring were too low for economical finishing. Therefore, high-removal-rate synthetic lap polishing was implemented at Zygo to polish out the ground surfaces and to remove subsurface damage. The specific removal amounts and rates are proprietary to the finishing supplier. The final polishing step implemented at Zygo was pitch polishing on one of three 168-in. granite-ring polishing laps, as shown polishing an amplifier slab in Fig. 13. A closed-loop thermal system and computer controls were utilized on these polishing machines to achieve an extremely stable platform, as illustrated in Fig. 16. Because of the stability of the polishing machine, optics that previously required an average of over ten iterations to achieve reflected wavefront requirements of $\lambda/3$ P-V and $\lambda/90$ rms gradient measured at 633 nm converged in only a few iterations.

The polarizers have reflected and transmitted wavefront specifications of $\lambda/3$ P-V and $\lambda/90$ rms gradient measured at 633 nm. Two approaches were explored to meet the transmitted wavefront requirements. First, high-homogeneity BK7 blanks (< 1 ppm) were finished to specification using the finishing process described in this section. However, additional iterations were required to meet specifications, which drove up the time and cost for finishing. Second,

lower-cost, lower-homogeneity BK7 blanks (< 2 ppm) were finished to < 1 λ P-V transmitted wavefront, and then ion-beam figuring (a highly deterministic small-tool figuring process) was used to meet specifications. It was found that polarizers figured using ion beams tended to be at least a factor of two better than specification.[62] The improved performance and overall lower cost resulted in 98% of the polarizers being fabricated with ion-beam figuring.

V.B.3 Mirror and Polarizer Coating

The coatings on NIF mirrors and polarizers are multi-layer, high-reflectivity, dielectric coatings deposited using alternating layers of e-beam evaporated hafnia (HfO_2) and silica (SiO_2). These coating materials were selected because they have an adequate difference in the index of refraction and because they tend to yield the highest laser resistance at 1053 nm. This high resistance is the result of their high bandgap, low absorption, high melting temperatures, and low defect densities.[63] Electron-beam (e-beam) deposition was the optical coating process developed for NIF mirrors and polarizers because e-beam coatings tend to have the highest laser resistance at the laser wavelength of 1053 nm. Additionally, e-beam coatings are easily scaled to meter-class optics. Metallic hafnium was used as the starting material for hafnia layers because of improved laser resistance, reduced defect densities, and improved plume stability for better layer-thickness control.[64-66] The silica layers were applied using high-purity silica granules as starting material. The NIF large mirrors and polarizers were coated at two suppliers, Spectra-Physics and Laboratory for Laser Energetics (LLE).

One of the challenges during mirror production was introduced by temperature cycling of the mirrors during e-beam coating. This cycling resulted in inconsistent P-V errors in mirror surfaces. The NIF could accept mirrors with up to λ/3 power measured at 1064 nm because the

decollimation introduced by this power could be compensated in the MLS by adjusting the actuators of LM1 (the deformable mirror) and in the FOA by adjusting the position of the WFL.

To prepare the finished substrates for coating, they are manually cleaned, ultrasonically cleaned, and then air-dried in a clean room. After deposition, the optics are laser-conditioned using the LACs described in Section III.B and then visually inspected as shown in Fig. 17. Laser conditioning is a process used to increase the effective laser resistance of a mirror coating by removing coating imperfections (nodules.) This is done by raster scanning a laser beam over the optic surface, starting at low and increasing to higher fluences. With incrementally increasing fluences, loosely bound coating nodules can be ejected without disrupting the surrounding coating and substrate. This process leaves behind a pit that is stable with respect to growth upon subsequent exposure to higher fluences. Since these pits are small, typically microns in diameter, there is minimal impact of the pit to a meter-size laser beam. However, if the same nodule is removed initially at a higher fluence, the disrupted area is larger and rougher (sharper edges). This leads to electric field enhancements and higher levels of damage that could grow with subsequent scans or shots.[67-69] Laser conditioning was performed off-line by raster scanning mirrors past a 1-mm-diameter laser beam. Three laser scans of increasing fluence (10, 14, and 18 J/cm^2, 3 ns equivalent, respectively) were performed on all NIF transport beam mirrors.[70]

V.B.4 Metrology of Mirrors and Polarizers

After laser conditioning, the coated optics are measured for compliance with specifications. Cavity mirrors and polarizers only have spectral requirements at 1053 nm, which were validated using the Bauer photometer. The polarizers have an additional transmitted wavefront specification compared to the cavity and transport mirrors. Transport mirrors, however, have extremely complex spectral requirements, which are validated with the Bauer

laser photometer (Fig. 18, left) over the optic full aperture at 1053, 527, and 351 nm and with broadband UV-Vis spectrometer on a coating witness sample.[71] The transport mirrors steer 1053-nm laser light to the FOA as well as 375-nm laser light for alignment of the 351-nm light on target.[10] Therefore, high reflectivity is required at these two wavelengths for transport mirrors. To meet the reflection requirements at both wavelengths, the coatings are intentionally spectrally miss-centered within the high reflector band at 1053 nm. To prevent backscattered light from damaging a diagnostic pickoff mirror within the transport spatial filter, the transport mirrors are designed to suppress backscattered light from the target. Therefore, low reflectivity is required at stimulated Brillion scattering (SBS) wavelengths near 351 nm and at stimulated Raman scattering (SRS) wavelengths that can range from 400–700 nm. For this measurement, a UV-Vis spectrometer is used to measure a witness sample from a coating run. Shown in Fig. 18 (right) is the averaged spectral characteristics over the wavelength range of 300–1200 nm for 22 NIF transport-mirror coating runs.

The reflected wavefront of NIF mirrors is controlled for the use environment by appropriately tuning the oxygen flow during silica deposition.[72] Because the reflected wavefront is also sensitive to humidity, the wavefront control loop of the deformable mirror is designed and used to maintain an acceptable reflected wavefront in the low-humidity section ($< 2\%$) of NIF. It is in this section where distortion of the reflected wavefront due to humidity is expected to be the greatest. The transport mirrors, on the other hand, are not part of the deformable mirror correction loop and humidity can be a problem. In the transport mirror section where the mirrors are in an argon environment, the relative humidity level is held at a much higher level ($40 \pm 6.5\%$) to ensure mirror stability. Under these conditions, minimal reflected wavefront distortion of the transport mirrors has been observed. Because errors in the reflected wavefront can result in

beam defocusing, provisions have been made to repositioning of the wedged focus lens to correct for some beam defocus. Therefore, up to λ/3 waves of power measured at 1064 nm is allowed to be subtracted during reflected wavefront measurements of the transport mirrors.

All cavity and transport mirrors are measured at their use angle and wavelength. Measuring in this way minimizes error due to phase distortions caused by multi-layer interference coatings. The coating suppliers were provided with phase measuring interferometers, converted to operate at a wavelength of 1064 nm, so they could measure mirror performance during fabrication at their use angle. Measurements at use angle avoided confusion that can be caused by non-linear interference when outside of the reflection band and not at use angle. To reduce the facilitization costs, it was decided that using existing subscale 18-in. interferometers would be adequate because the dominate wavefront distortion term in optical coatings is power (or spherical curvature) due to coating stress. An 18-in. phase measuring interferometer operating at 1064 nm is shown in Fig. 19, measuring the reflected wavefront of a deformable mirror after coating.

Because SBS and SRS back-reflected light from the targets is transmitted through the coating on the transport mirrors, it was necessary to darken the BK7 substrates for the final two transport mirrors, LM7 and LM8, after coating to protect the metallic mounting and alignment hardware located behind these mirrors.[73] Gamma radiation from a cobalt-60 source used for sterilization of medical devices was used for this purpose. Gamma radiation causes the formation of color centers in BK7 glass, leading to a visual darkening of the glass as illustrated in Fig. 20 (left optic). Studies have shown little degradation in the 351-nm and 1053-nm laser resistance of the optical coating for nanosecond pulse lengths after exposure to gamma radiation.[73] Minimal

reflected wavefront distortion is observed, provided that both sides of the mirror are uniformly irradiated to prevent differential compaction effects.

V.C. Fused Silica Lenses and Windows

As shown in Table VI, a total of 2112 fused silica optics are installed on NIF. This includes 576 thick flats, 960 lenses, and 576 thin flats.

The thick flats are used as robust vacuum windows at three locations within each NIF beamline (see Fig. 1).[74] These include a pair of switch windows (SWs) and a single TCVW. The SWs provide a pair of vacuum barriers that isolate the low pressure required for operation of the PEPC from the ambient beamline environment.[75, 76] Similarly, the TCVW is used as the primary vacuum barrier between the ambient pressure within the beamline and the low-pressure region of the FOA.[16]

Also shown in Fig. 1, a total of five lenses are installed in each NIF beamline. The first four are located in the 1ω section of the laser while the fifth, the final focusing lens, is installed in the 3ω section of the laser. The four 1ω lenses consist of two matched pairs of long focal-length (nominally 12-m and 30-m) equi-biconvex lenses to which a small aspheric correction has been applied to one face. Each of the matched pairs of lenses is used to construct the spatial filter assemblies that are present along every NIF beamline. The spatial filters are telescopes with a unity magnification. They serve to relay image the flat amplitude field, which originates at the output of the regenerative amplifier, to locations of other optical surfaces along the beamlines. These large spatial filters include pinholes located at the foci of the lenses for stripping high spatial frequency noise from the propagating beams. More details on the relay planes and features of the pinholes is given in the article "Damage Mechanisms Managed or Avoided for NIF Large Optics" in this issue of *FS&T*.[37]

The fifth and final lens in each of NIF's 192 beamlines is an off-axis WFL having a 7.7-m focal length. The off-axis aspheric plano-convex element serves multiple functions. In addition to focusing the 3ω beam of light to the target chamber center (TCC), the prismatic design of a WFL separates residual 1ω and 2ω light from the 3ω focus. A combination of the angular orientation of the lens within the IOM and the wedge design also serves to manage ghost reflections by steering them to beam dumps.

In addition to the thick vacuum windows and lenses described above, three thin ($\approx$10-mm) fused silica flat optics are also installed in each of NIF's 192 beamlines (see Fig. 1 and Table VI). These optics include the diagnostic beam splitter (DBS), the CPP, and the GDS.

The DBS, which is a slightly wedged flat optic, is installed just beyond the output of the transport spatial filter (TSF) and reflects $\approx$0.1% of the output light from each NIF beam to a set of 1ω beam diagnostics. In addition to an integrating sphere and a dedicated energy measuring photodiode, the light sampled by each DBS is also subsequently available to the output sensor package (OSP) which can be configured for use as an alignment sensor, a 1ω optics inspection system, or a 1ω system shot diagnostic.

NIF CPPs are full aperture diffractive optics that are used, in conjunction with the final focusing lens, to modify the size, shape, and to increase the uniformity of the far field focal spot delivered by each beam-line (see Fig. 21). NIF CPPs are custom optics with designs based upon the far-field requirements needed for experiments conducted on NIF and are designed for a Fourier plane that is 7.7-m ahead of the WFL. The decreased peak intensity and uniformity provided by the CPP reduces losses that would otherwise be encountered due to laser-plasma interactions (LPI) that can become important during inertial confinement fusion (ICF) implosions.[16, 17, 77, 78]

The final thin fused silica optic in each beamline is the GDS (see Fig. 1). At 1 cm the GDS is more than three times as thick as the DDS. Thus the GDS serves as a final, robust, mechanical barrier that protects upstream optics from impact damage due to high-velocity debris that can originate from the exploding target. To date this capability has never been called into service. The GDS also serves as a vacuum barrier between the FOA, which is maintained at 10 Torr of clean dry air (CDA) and the hard vacuum ($\approx 10^{-6}$ Torr) of the target chamber. Finally, the GDS is also used to diffractively sample a small fixed ($\approx 0.2\%$) fraction of the main 3ω beam and divert it to the drive diagnostic (DrD) system (see Fig. 3) located in the FOA.[28]

V.C.1 Lens and Window Blanks

All of the lenses, windows, and diffractive optics in NIF (see Table VI) are fabricated from fused silica, with the exception of the thin (1–3 mm), relatively inexpensive DDSs that are the final optic in each beamline. The choice of fused silica was dictated by several economic and technical considerations: its chemical stability is excellent; its optical, mechanical, and thermo-mechanical properties are favorable; and extraordinarily high-quality fused silica is commercially available from a number of leading manufacturers (see Fig. 7).[82-86] The availability of material meeting the size and quality specifications consistent with NIF requirements was of considerable importance given the large (> 30 tons) quantity required for fabrication of the fused silica optics needed for NIF.

One very important additional consideration leading to the choice of fused silica is its resistance to laser damage when exposed to both high fluence and high power 1ω and 3ω light. Experience beginning with the Novette laser at LLNL indicated that fused silica synthesized by conventional chemical vapor deposition (CVD) techniques (Ref. 83) could be successfully used to manufacture optical components transmitting 1ω light. This continues to be the material of

choice for the fabrication of 1ω components within NIF's MLS. Fused silica has proven to be robust relative to both filamentation (a process that occurs in the bulk) and surface damage.[87-90] The NIF beamlines were designed to avoid intensity levels where filamentation might become important and commercial surface-finishing processes were adequate at the time to prevent surface damage at 1ω.

Optics in the FOA (Ref. 16) such as the WFL and GDS are subject to high-fluence 3ω in addition to 1ω and 2ω light. In such cases the experience is quite different. For these components, it was found that index inhomogeneities resulting from the dissolution of refractory particles dispersed throughout conventional CVD fused silica can lead to pseudoscoping imaging, a process that causes light to focus in either the same or subsequent optics along the beampath.[91] This pseudoscopically focused light most often damages the optics on their exit surfaces, their most vulnerable location. Thus, for fabrication of the 3ω windows and lenses, an inclusion-free grade of CVD fused silica is required.[84-86]

V.C.2 Optical Damage Considerations Related to Finishing

While the use of inclusion-free fused silica substrates is necessary to minimize optically induced surface damage of the fused silica components operating in the ultraviolet (3ω), it is by no means sufficient. The *NIF Functional Requirements & Primary Criteria* require NIF to operate at fluence levels that are more than twice the damage-growth threshold of fused silica. To operate in this regime a series of unique diagnostic, operational, and processing techniques were developed and implemented. These innovations are discussed in the paper entitled "Optics Recycle Loop Strategy for NIF Operations above the UV Laser Induced Damage Threshold", in this issue of *FS&T*.[38] Successful operation of the NIF Optics Recycle Loop requires both the ability of the optics to operate at relatively high fluence levels before a damage site is initiated

and the ability to find and mitigate growing sites after their initiation. Because the Optics Recycle Loop comprises many processing steps that are capable of addressing only a relatively small number (< 50) of individual damage sites on a given optic, it was necessary to improve significantly the damage resistance of fused silica surfaces. On a 40×40 cm^2 aperture optics typical of NIF, 50 sites are equivalent to a damage density of ≈ 0.03 sites/cm^2 (see Fig. 22).

As shown in Fig. 22, to bring the damage density of 3ω optics operating at NIF relevant fluences to a level compatible with the Optics Recycle Loop, it was necessarily to reduce the damage density of finished optics by a factor of $\approx 10^4$ relative to the performance of optics that were available in 1997. Although a comprehensive discussion of the optically induced damage process is beyond the scope of this paper, it is useful to consider some of the key aspects of the problem that are relevant to the finishing and performance of optics on the NIF laser, which uses nanosecond-scale ultra-violet (UV) pulses at fluences of 5–10 J/cm^2. As one progresses from the infrared (IR) to the UV, the propensity for optical damage typically increases dramatically. In a well-designed system fabricated from high-quality materials (see above), surface rather than bulk damage is the dominant form of laser-induced damage.

Ultimately surface laser damage in this regime typically scales with fluence rather than intensity, and it is the result of a localized thermal runaway.[95] Due to its high band-gap (9.0 eV), bulk fused silica is transparent to the 3.5-eV near-UV photons generated in the 3ω section of the NIF laser. At the intensities characteristic of the NIF laser, optical damage results from the presence of extrinsic laser-damage precursors that lie at or within the near surface layer of the optic. Such laser-damage precursors are small, highly absorptive centers that reach high local temperatures when exposed to high fluence light. When tightly coupled to the surrounding silica matrix, the thermal energy associated with the heated precursor diffuses into the surrounding

glass.[96] Once the temperature of fused silica reaches ~5000°C, the bulk material itself becomes absorptive, leading to local runaway heating that continues until the end of the laser pulse. A series of laser-damage precursors capable of strongly absorbing sub-band gap light and spawning optical damage have been identified. These precursors include photoactive impurities such as ceria in the polishing layer and electronic defects associated with fracture surfaces.[97-101] More recently even small residues of both organic and inorganic impurities on optical surfaces have been identified as damage precursors at high fluences.[94, 102]

Upon further exposure to high fluence light, the high absorption associated with surface cracks can cause damage-initiated sites to grow in size.[103-105] The continued growth of a damage site can ultimately lead to an unacceptable obscuration or even the catastrophic failure of a lens or window that is used as a vacuum barrier.[74] The identification and subsequent management of damage precursors throughout optical fabrication (see Section V.C.3) and pre-installation processes ultimately led to large decreases in the densities of initiation sites that enable the operation of the NIF laser at fluences that meet and exceed its original 1.8-MJ design goal.

V.C.3 Lens and Window Finishing

It is useful to divide the optical fabrication process into two general activities, specifically optical finishing and metrology operations.[106, 107] In this context, optical finishing refers to the material-removal steps of grinding and polishing that converts an optical blank (also called a substrate) into the desired final optical component. Similarly, metrology refers to the host of mechanical and optical measurements that are used throughout the grinding and polishing operations to validate that the optical component meets in-process and final mechanical and optical performance requirements.

The first step in the finishing process involves shaping the rough-cut, fused silica substrate by grinding (see Fig. 23). During grinding, abrasive particles are used to rapidly (0.2–2 μm/min) remove material from the substrate. One or more additional fine-grinding steps using successively smaller abrasives are often used. In addition to refining the basic shape of the substrate, a well-executed, fine-grinding process replaces all traces of the surface fractures introduced by the previous rough-grinding step, with a shallower fracture layer corresponding to the smaller abrasive size.

Empirical or semi-empirical guidelines have traditionally been used for making decisions on the depth of material that should be removed by subsequent grinding (or polishing) steps. These rules considered parameters such as the size of the abrasive grit used during the previous operation or the roughness of the ground substrate.[108-111] Since the defect layer associated with even minute fractures results in laser damage when exposed to high fluence UV light, such practices are inadequate for the production of optical components for use on the NIF laser.[98, 100, 101]

In place of such empirical rules, a series of physics-based studies were conducted to characterize and understand the underlying principles that control the depth of the mechanical subsurface damage associated with both fixed- and loose-abrasive grinding operations.[112-114] The depth of mechanical damage produced during grinding was assessed using the following method. Working with each of NIF's industry partners, representative substrates were ground using the same production tools, abrasive grits, and feed rates used for fabrication of NIF optics. Using a magneto-rheological finishing (MRF) polisher, a series of tapers of varying slope and depth were then polished into each substrate. To enhance the visibility of the residual fracture network, the substrates were subjected to a shallow hydrofluoric acid etch, and photomicrographs were

recorded along the areas of the substrates that had been polished to varying depths. As shown in Fig. 24, the extent of subsurface mechanical damage for a given grinding process can be determined by plotting the obscuration resulting from the network of remaining fractures (cracks) as a function of the local depth removed during the tapered MRF polish. This method provides a quantitative tool for determining the depth of material that must be removed by subsequent grinding or polishing steps to ensure that no remnants of subsurface damage remain from previous processes. With the aid of this MRF polished-taper technique, statistically relevant data on the depth of fracture networks imparted by various grinding processes can readily be recorded that is statistically relevant over more than five orders of magnitude.

Following the final grinding step, optics are polished to remove the thin layer of fractured material remaining and to impart the final figure (shape) onto the optical element. The thick windows (flats) used in the main (1ω) laser system are finished using either full-aperture synthetic pad laps or traditional pitch laps. Similarly, conventional full-aperture polishing is used to prepare lenses for final polishing. Small-tool computer-controlled optical surfacing (CCOS) or MRF finishing techniques are used for final polishing of lenses (see Fig. 25). In particular, alternate cycles of polishing using CCOS or MRF and full-aperture interferometry are used to deterministically converge to the transmitted wavefront quality required of each NIF lens.

"Rogue" particles can be problematic during both the grinding and polishing operations associated with optics fabrication. Rogue particles refer to particles that are anomalously large relative to the typical distribution of grinding or polishing particles in contact with the surface of the optic during a given grinding or polishing operation. In the case of grinding, the presence of rogue particles increases the variability and depth of the fractured layer (subsurface damage). In the case of polishing, rogue particles lead to polishing scratches (isolated surface fractures).

The presence of either residual fractures from the grinding process or polishing scratches is a particularly important issue for NIF optics because the electronic defects associated with fracture surfaces are known to be laser-damage precursors.[100, 101] Thus, for optics that encounter high fluence and high-intensity light, particularly at 3ω, it is especially important to minimize the number and size of surface and subsurface fractures. Using guidance resulting from the MRF taper-polishing studies (see Fig. 24), NIF finishing suppliers were provided with the material-removal requirements needed to ensure that even the last remnants of grinding damage is removed from NIF 3ω optics during polishing.

The key to reducing damage-inducing scratches during polishing is to eliminate or significantly reduce the number of rogue particles present in the polishing slurry. Eliminating such anomalously large particles from the polishing slurry minimizes both the number and size of surface scratches. The specific role that rogue particles play with respect to forming scratches is described below. Although this analysis is described in terms of a polishing operation, the same concepts are equally applicable to grinding as well.

The formation of surface scratches can be understood by considering the presence of a rogue particle at the interface between an optic and a polishing lap.[115] In a configuration shown in Fig. 26, the total load of an optic on the polishing lap is typically supported by an ensemble of particles that lie between the optic and the lap. The load present at the interface between any single particle and the optic surface can be shown to increase in proportion to the size of that particle. As a result, rogue particles can lead to local loads (P_1) that exceed the threshold required to initiate a fracture on the surface of the glass.[116, 117] The length of the resulting trailing indentation fracture (or scratch) is ultimately related to the time it takes for the highly loaded rogue particle (responsible for fracture initiation) to sink into the compliant lap, thus

redistributing the load among numerous other particles. As shown in Fig. 26, the presence of rogue (heavily loaded) particles introduces significant variability in the extent of material damage in terms of the number, length, and depth of cracks imparted to the optic during a processing step.[116, 117]

Eliminating rogue particles and thus removing the cause of scratching during polishing is very challenging. This is because (1) the particles present in polishing slurry are small and (2) scratches typically extend to depths that are large relative to the rate at which material is removed during polishing. Rogue particles can originate from a variety of sources, including environmental contamination, residue from grinding operations, or even an unfavorable initial particle-size distribution in the polishing slurry. Similarly, damaging rogue particles can be generated during the polishing operation itself. This is most often the result of the agglomeration and subsequent drying of polishing compound that makes its way back onto the polishing lap. In addition to the use of high-quality materials, environmental controls, and careful attention to cleanliness, the use of slurry dispersants and filtration have proven to be an effective means of minimizing polishing scratches.[118, 119]

Because surface scratches are laser-damage precursors, their presence on 3ω optics is of significant concern. Therefore, it is important to identify the source and cause of rogue particles that are responsible for producing a specific scratch onto the surface during polishing. Given the presence of a scratch, it must be determined if it is more advantageous to remove the scratch by additional polishing or by regrinding and repolishing the substrate. The key to answering these questions requires the ability to observe and interpret the fracture markings present on the surface of an optic. To aid in the interpretation of such markings, a series of surface fractures were created using both static and dynamic Vickers (sharp) and Brinell (blunt) indenters (Ref.

120) that are typical of commonly encountered indentations and scratches during polishing. To enhance the visualization of these fractures, the surface was lightly etched (e.g., < 1 μm) with acidic solution containing fluoride ions, such as hydrofluoric acid (HF) or a buffered oxide etch.[120, 121] Because the etching process just described removes the polishing layer from the glass surface and increases the scratch dimensions, it makes them more visible and easier to detect during inspection. Based on observations of fractures created under these well-controlled conditions, a series of diagnostic rules were established that relate the morphology of etched fractures to useful parameters such as the probable size and depth of the fracture and the direction of travel of the indenter (rogue particle) relative to the optic surface.[116, 117, 122] These rules resulted in a valuable in-process diagnostic tool that greatly aided in improving the yield, quality, and rate of optics production.

In addition to enhancing the ability to observe and thus interpret isolated surface fractures on polished surfaces, fluoride-based etching has also reduced the time required for polishing a surface compared to the time required for a ground but unetched surface. When a ground surface containing a high density of fractures is etched, a series of cusps corresponding to the enlargement of each individual fracture on the surface of the substrate is created. Given sufficient etching time, these individual cusps coalesce with one another and leave a surface that requires significantly less polishing time than would otherwise be needed. Figure 27 shows a computer simulation illustrating this effect.

V.C. 4 Finishing of Thin Flats

After grinding, the thin substrates that are ultimately used for fabrication of the DBSs, CPPs, and GDSs are initially polished using conventional synthetic laps. The remaining finishing steps that are applied to each substrate are dependent upon the end use of the optic. For example,

the DBSs, which are used to sample the 1ω portion of the laser, are typically ion figured (Ref. 62) to achieve the low roughness and gradient specifications required of this optic. Similarly, the thin substrates that are ultimately used in the FOA section of NIF (the CPP or the GDS) are typically finished using MRF polishing and then subjected to a hydrofluoric acid etch to remove residual iron and Ce contaminates introduced during the polishing of the substrate.[123] Once the polished substrates are prepared, CPPs or GDSs are imprinted with a diffractive pattern prior to final use. The CPP diffractive pattern is imprinted using MRF technology at the supplier site as described in section V.C.5. The diffractive grating on the GDS is applied at LLNL using an interference lithography process (see Section V.C.7).

V.C.5 Fabrication of CPPs

The earliest phase plates introduced to perform rudimentary beam conditioning on the NOVA laser system in 1991 employed a resist-masking and acid-etching process to imprint first a binary rectangular/hexagonal phase plate structure (Refs. 123-125) and later a 16-level kinoform phase structure (Refs. 126,127) onto the fused silica substrates. This approach to phase plate fabrication was later replaced by masking and resistive-ion-etching techniques that were capable of imprinting higher efficiency patterns onto optics for use at LLE (Refs. 128, 129) and the Laser MegaJoule facility.[130]

In contrast, the topographical features of the CPPs for NIF are polished directly onto one surface of the optic. The use of polishing eliminates wavefront discontinuities and high contrast inherent in discrete (stepped) plate designs. Moreover, the continuously varying topology of polished CPPs provides the ability to tailor the energy contours at the high-power focal plane as required by target designers. For example, by manipulation of the near-field topography of the CPP (see Fig. 28), the far-field beam can be designed to convert a square or circular laser beam

footprint to an elliptical or circular spot of prescribed lateral dimensions. Other spot shapes such as triangles, squares, or other closed polygons are also possible. In this manner the beam footprint at the focal plane can be manipulated and optimized as required to support a variety of experimental configurations. Such configurations include both indirect and direct drive implosion cone beams as well as back-lighter/backscatter diagnostic beam drivers. As such, CPPs are considered NIF user-prescribed optics and are tailored for each particular experiment.

All NIF CPPs are manufactured using MRF polishing. MRF finishing is a small-tool optical polishing process that combines the use of interferometry, and precise numerically controlled polishing equipment. The technique was pioneered by William Kordonski and his colleagues at the Luikov Institute of Heat and Mass Transfer in Minsk. The process was later refined by Kordonski, Steve Jacobs, and Don Golini and co-workers at the University of Rochester's Center for Optics Manufacturing. Ultimately MRF equipment was commercialized by Golini, who subsequently founded QED technologies.[131] Methods for imprinting CPPs using MRF were jointly developed by QED and LLNL.

MRF finishing involves the use of a sub-aperture polishing tool whose removal shape is generated by the interaction of a magnetic field and an iron-based magnetorheological fluid, which contains microscopic abrasive particles such as ceria or nano-diamonds. A schematic diagram illustrating a typical MRF polishing system is shown in Fig. 29. As shown in the figure, the optic is positioned a fixed distance from a moving spherical wheel. An electromagnet located below the wheel surface generates a magnetic field in the gap between the wheel and the optic. When the MR fluid is delivered to the wheel, it is pulled against the surface of the wheel by the magnetic field where it becomes a sub-aperture polishing tool.

Computer algorithms determine a "polishing schedule" as a function of velocity as the optic translates through the polishing zone in either a rotating or raster pattern. When combined with interferometry, which is used to characterize the amount of material that must be removed to achieve a desired surface topology, MRF is a deterministic polishing technique. Because MRF involves the use of a small-scale polishing tool, it is well suited for figuring the phase aberrations required for CPP fabrication.

MRF offers a direct approach for imprinting smooth topographical features onto optics without the use of lithographic masks or master plates. Its deterministic polishing capability, wide array of available removal functions, and close interplay with interferometry enable the imprinting of diffractive phase structures that vary continuously across the entire beam aperture without inducing sharp discontinuities or phase anomalies that could lead to downstream optical damage.

The CPPs fabricated by NIF's MRF capability are primarily designed for use in either the infrared (1053 nm) or visible (532 nm) sections of the laser systems or are designed for manipulating the far-field characteristics of ultraviolet (351 nm) beams.[16, 18] CPP designs themselves, however, are nearly achromatic and can be used at any wavelength with nearly equivalent results. When small changes in the far-field characteristics do arise they are typically small ($\approx$2% between the IR and UV wavelengths), and can be attributed to the ratio between the refractive index of the substrate at the use wavelength and the original design wavelength. Differences in the far-field characteristics of this magnitude typically fall within application tolerances and can often be ignored. The main difficulty to overcome in using CPPs in high-power UV applications is the preparation of a substrate that has sufficient optical damage

resistance in the UV. This requires fabrication protocols which combine MRF imprinting processes and UV laser-resistant fabrication techniques.[123]

The imprinting of a surface topography, such as that required for CPPs fabrication, is a non-traditional application of MRF technology. As a prelude to CPP manufacturing, LLNL performed a series experiments to understand the relationship between the removal function and imprint fidelity, as illustrated in Fig. 30.[127, 132] Such work indicated that the efficiency of the MRF imprinting process is directly related to the width of the MRF removal function. The width of the removal function limits the spatial bandwidth of the surface topography due to Nyquist critical-sampling issues. The removal function contains a band of Nyquist critical-sampling frequencies between its narrowest and widest footprint dimensions. As spatial periods decrease, wider portions of the removal function become ineffective and lead to longer polishing times and greater material removal requirements owing to collateral polishing and topographical erasure.

Experiments such as these resulted in several important finding regarding techniques required to successfully fabricate CPPs. First, to achieve the desired topographical fidelity the imprinting process often requires a multi-pass approach. Each pass incorporates a different size removal function that maximizes material removal over the topographical scale length being imprinted. Large removal functions are used early in the fabrication process, while the small removal functions are used in the final stage of fabrication to apply small scale topographical corrections. Secondly to optimize phase-front corrections, in-process interferometry must be used as an integral part of the fabrication process. Finally, superposition should be used during imprinting to simplify the CPP prescription and to accommodate process breakpoints necessary for testing.

The large-aperture MRF system required for imprinting full aperture (430 mm × 430 mm) NIF CPPs is shown Fig. 31. This custom-built system uses two wheels, a large (370-mm diameter) wheel and a small (50-mm diameter) wheel together with optimized computer control algorithms to provide the capability to finish the wide range spatial scale length features required of NIF CPP designs. This MRF machine is capable of polishing rectangular optics up to 750 mm × 1000 mm in size.

Prior to imprinting, substrates are polished using the large polishing wheel, in raster mode, which allows material to be removed at rates of up to 1 mm³/min. This translates into the ability to uniformly remove on the order of 1μm of material from a full aperture fused silica optic in about nine hours. Final figure correction of the substrates, prior to imprinting, is performed to achieve a TWF of < 200 nm PV and an rms gradient of < 7 nm/cm within the clear aperture.

The basic methodology used to manufacture large aperture CPPs is similar to that used for the production of small (50 x 300 mm) CPPs.[131] The first step in the imprinting process is to generate a removal map which corresponds to the amount of material that must be removed from each spatial location to bring the TWF of the polished optic into congruence with the CPP design prescription. Removal maps are calculated as the difference between the interferometrically measured TWF of the optic prior to each polishing iteration and the TWF specified by the CPP design. Once the removal map has been generated, the necessary topological features can begin to be polished into the substrate.

As outline above, the imprinting process starts using large (≈1 mm³/min) removal functions which are used to polish low spatial frequency features into the optical surface. Iterative raster scans with smaller removal functions are then used to imprint features having

smaller spatial periods into the optic and to refine the gradients present in the pattern. Following each polishing iteration the TWF of the CPP is measured and used to generate a new removal map for the subsequent MRF polishing step. The imprinting process is complete when the TWF converges to that required by the specification. The technology routinely produces topographical profiles having rms errors of < 30 nm relative to the idealized CPP prescription. Optical surface finish, specified in terms of rms roughness, is typically maintained at < 4 Ångstroms. Material removal rates are a function of the polishing function utilized and typically range between 0.025 and 1 mm3/m which facilitates the production of full NIF aperture CPPs in 50–75 hours.

The manufacture of damage-resistant CPPs for use in the UV (351 nm) follows a similar imprinting protocol, starting with substrates manufactured for use in the UV. The primary difference being that the optics that are to be exposed to high fluence UV light must be HF acid etched after MRF imprinting is complete to remove contaminants imparted during the MRF polishing process.[123]

During ICF experiments the far-field spot size in must be precisely controlled. This control is needed to keep the laser beam from impinging upon critical components in the target area, to ensure that the total delivered laser energy falls within the prescribed range, and to establish the proper projection angles onto the target during indirect drive experiments. ICF specifications typically require the far-field spot size to be within ± 15 μm at selected radii, typically encircled energy values of 80%, 90%, and 95%.

Figure 32 and Table VII illustrate the far-field characteristics of three representative CPP designs that have been fabricated and tested at LLNL, for subsequent deployment on NIF. As shown in this figure the far-field spots have super-Gaussian beam edges of orders that are typically > 6 and have a maximum deviation of ± 5 μm from nominal. The typical CPP spot sizes

shown in Fig. 32 and Table VII fall well within the tolerances described above and illustrate that CPPs can be routinely manufactured that meet the stringent specifications necessary for high-power laser ICF experiments.

To date twenty unique CPP designs, and more than 350 CPPs, have been manufactured and tested for use on NIF and other laser systems. NIF currently has five large aperture MRF tools capable of imprinting large-aperture CPPs which corresponds to a capacity to imprint up to about 200 CPPs a year. Current efforts include the design and manufacturing optimization for Polar Direct Drive ignition experiments in collaboration with LLE.

V.C.6 Metrology of Lenses

Each optic fabricated for the NIF laser was characterized over a continuous range of spatial scale lengths ranging from full-aperture down to 10 μm using a series of optical metrology tools as described in section III.B.[2] It was also necessary to characterize the focal length of each lens to a high degree (0.01%) of precision. This was done using a custom-designed and built Lens Optical Test System (LOTS).[133] Using this system, the lens under test is inserted into an optical test cavity created between a full-aperture (24-in.) phase shifting interferometer and a retro-sphere. Once inserted into the cavity, all interference fringes are nulled by appropriate translation of the lens under test. The back focal length (BFL) of each lens is then determined relative to a master lens of known BFL. This is done by replacing the optic under test with a master lens and then again nulling all fringes by translation of the master lens within the optical cavity. Measuring the difference between the null points of the master lens and the lens under test provides a direct measurement of the difference in BFLs between the test lens and the master lens.

To facilitate production of each lens type (Cavity SF, Transport SF, or off-axis WFL) required for NIF (see Table VI) the LOTS system is equipped with a high-precision turret system, allowing the use of any of four different retro-spheres.

V.C.7 Post Fabrication Processing of Fused Silica Optics

Following fabrication, fused silica lenses and windows are sent to LLNL's OPF for final processing and assembly. Each 1ω optic used in the MLS is cleaned, inspected, and coated. The AR coatings for large, transmissive, fused silica optics are based on a quarter-wave porous silica coating, which is applied to the 1ω optics and 3ω off-axis WFL by dip coating.[13, 15, 134] These sol-gel coatings provide outstanding AR properties at their use wavelength (<< 0.25% reflection per surface) while also providing the required resistance to optical damage. After coating, the optics are exposed to an ammonia and water vapor-rich environment. This post-processing step both reduces the porosity of the sol-gel coating and crosslinks the coating through the formation of siloxane (Si-O-Si) linkages. This results in a coating that is more adherent and less susceptible to pore filling by airborne organic contaminants. Sol-gel coatings are characterized using ellipsometry to measure film thickness and refractive index thus allowing inference of spectral performance. Sol-gel coating defects, if present, are first identified using the line-scan image mapping system IMS (line-scan IMS) and then further characterized for phase modulation using phase shifting diffraction interferometry (PSDI).[135]

Prior to coating, both the 3ω off-axis WFLs and the GDSs are treated using LLNL's Advanced Mitigation Protocol (AMP) to reduce the density of optical-damage precursors on the surfaces of fused silica optics exposed to high-fluence UV light.[38, 92, 93] After initial AMP processing, one side of the GDS is imprinted with a shallow (~15-nm) grating with a period ranging from 1 to 3 microns. A two-beam laser interference lithography system that mimics the

in-use geometry of NIF is used to write the GDS pattern into the photoresist.[136, 137] To achieve

the required photoresist uniformity over the large-aperture substrate, a meniscus coating

technique is used. After exposure, the GDS pattern is transferred from the photoresist to the

substrate using a buffered oxide etch. Subsequent to grating fabrication, a scanning photometer

called DOFAST is used to simultaneously measure the transmitted and diffracted energy. This

allows the spatial uniformity and the diffraction (sampling) efficiency to be accurately

determined. The measured diffraction efficiency and uniformity of the GDS is nominally ~0.3%

and < 5% rms, respectively. Spin coating is then used to apply a hexamethyl-disilazane (HDMS)

treated sol-gel AR coating to the unetched surface of the GDS.[138]

V.D. Crystals

V.D.1 Crystal growth

One of the many challenges of building NIF was developing crystal-growth technology

that could produce large crystal boules yielding the 41- and 42-cm per side single-crystal optics

needed for NIF while also meeting NIF's cost and schedule goals. Crystal optics are used in two

places in NIF. In the 1ω section a switch crystal (SC) is used for fast optical switching in the

PEPC. The PEPC is used in combination with a large-aperture (~0.5-m × 1-m) polarizer to

enable multi-passing the beam through the main amplifier. The second location of crystal optics

is in the FOA. There the crystals provide second and third harmonic frequency conversion (SHG

and THG) and polarization rotation. Nova, the previous large laser system at LLNL, used 27 cm

$\times$ 27 cm^2 KDP crystal optics for both frequency doubling and tripling in 3 × 3 arrays for

coverage of its round, 72-cm-diameter clear aperture beams. The Nova crystal optics were cut

from "traditionally" grown boules, crystals grown from a large seed crystal in a saturated

aqueous solution by the temperature-drop method. As the temperature of the solution is reduced,

the concentration of KDP/deuterated KDP (DKDP) above its equilibrium solubility provides the driving force for crystal growth. Using the traditional method with growth rates on the order of 1.5 mm/day, crystals of the needed size took approximately a year to grow. By the end of Nova construction, Cleveland Crystals Incorporated (CCI) was able to grow KDP and DKDP boules large enough to yield 30-cm^2 finished crystal optics. The crystal optics for Beamlet were larger, at 37 cm × 37 cm, but were still traditionally grown. With the success of Beamlet and the expectation of NIF construction, LLNL intensified its attention to crystal growth and production technology. To meet the increase in both the number and size of optics required for NIF construction, considerable advancements in the rate at which crystals could be grown was required.

Dr. Natalia Zaitseva came to LLNL in the mid-1990s from Russia after pioneering techniques for increasing the growth rate of this family of crystals.[139] By early 1998, rapid growth of NIF-size boules had been demonstrated in principle, and ongoing work was directed toward improving crystal quality.[140] A method for continuous filtration of the growth solution was developed to grow crystals with improved laser-damage resistance.[141] High growth rate requires constant replenishment of KDP-rich solution at the growing face. Rotation of the crystal within its water-based growth solution became an essential feature of the rapid-growth approach. Continuation of Zaitseva's work at LLNL led to rapid growth of > 40-cm crystal optics, with growth rates of ~1 cm/day.[142] By late 1998, although large crystals could be grown, the yield was still unacceptably low. Rapid-growth technology was transferred to CCI and Inrad for implementation as a commercial process, with CCI ultimately selected as the NIF crystal supplier. Work at LLNL was focused on improving the yield of growth runs. All of the large KDP boules produced at LLNL as part of this effort were shipped to CCI for fabrication.

The main challenge for rapid growth of KDP was production of crystal boules of sufficient quality and size to yield doubler (SHG) crystals for NIF. Figure 33 illustrates the relationship between boule orientation and the manner in which crystal optics can be cut from the boules. A "standard" boule of 55 cm × 55 cm × 55 cm is used for illustrative purposes; actual boule dimensions vary. Plasma electrode Pockels cell switch crystals, 41 cm × 41 cm, require the smallest size boules, with material yield possible from boules with base dimensions as small as 43 cm × 43 cm. The orientation of polarization rotator optics in the boule is similar to that for switch crystals. As a result of the complex orientation of the SHG crystal within the boule, the greatest crystal production challenge for NIF was growth of crystal boules large enough to yield SHG crystal optics. Producing SHGs requires crystal boules that are at least 51 cm × 51 cm × 51 cm.

The technical advances needed to get KDP boules with high yield using the rapid-growth process, both in terms of optic-yielding boules and larger number of optics per boule, were one result of a sustained R&D effort by both LLNL and CCI. In addition to having disciplined procedures to ensure run-to-run repeatability, precise control of the declining tank temperatures profile, reagent purity, and tank conditions, specific technical advances needed to be made in understanding KDP crystal growth on a fundamental level. Potassium di-hydrogen phosphate is a complex but well-studied system. Growth occurs on two faces, pyramidal (quasi-triangular faces) and prismatic (rectangular faces). Based on microscopic-scale studies these faces have been shown to grow very differently from each other, and their growth rates vary in a complex way because the growth parameters for each face are affected differently by supersaturation. In addition, growth (step velocity) on the prismatic face is very sensitive to the presence and level of certain elements that exist as impurities in the growth solution. Adding to the complexity are

the effects of temperature on the kinetics of step growth and impurity incorporation, both of which intimately affect step velocity and overall growth rates. In order to grow a crystal with the desired shape it is critical to control the relative growth rates of the two faces during the growth run. Conditions must be judiciously chosen (i.e., impurity level, supersaturation, and rotation parameters) to affect the growth rates and achieve the desired crystal dimensions. The following were key advances made in controlling crystal growth for yield optimization:

1. **Preventing Secondary Nucleation.** Secondary nucleation (i.e., formation of a second KDP crystal) within the solution growth tank system is detrimental because it will grow, migrate, and dislodge more crystals that eventually contact the main growing boule, prematurely ending the growth run. Sources for secondary heterogeneous nucleation include cracks and joints within the crystal-growth system, drying of the salt on the container walls, and impurity particles (either already present within the growth system or migrating in from the external environment). As the crystal gets larger during a growth run, other system changes occur. The larger the crystal the more it begins to act like a paddle and agitate the solution, causing a large, turbulent surface wave in the crystallizer. This turbulence in turn causes splashing of the solution onto surfaces in the headspace above the solution. If these surfaces are too hot or too cold, the droplets evaporate or condense and can become sites for nucleation. Secondary nucleation was initially the primary cause of growth-run failure; it needed to be understood for successful rapid-growth of KDP crystals. Another contributor of secondary nucleation is the stress induced on the crystal by the rotating platform, which can result in the generation of small flakes off the crystal that serve as nuclei. As the crystal becomes larger and the force from acceleration becomes greater this exacerbates stress risers in the crystal that

cause small fragments to break off. Several modifications to the crystallizer were important in reducing secondary formation during growth:[143]

    a. Added fluorinated (i.e., Teflon-like) coatings on the growth platform and liners on glass tank interior as a barrier to heterogeneous nucleation sites;

    b. Installed a continuous solution filtration system (CFS) to reduce impurity particle seeds;

    c. Improved sealing of the growth system and applied an overpressure of the tank atmosphere to prevent the entry of external particle seeds;

    d. Cooled the top part of the tank above the solution level to create condensation and wash down the tank walls to prevent drying of inadvertently splashed solution.

2. **Minimizing Liquid Inclusions**. During the crystal growth, small (micron-sized) pockets of solution can form on the growth face, leading to bulk liquid inclusions with unacceptable scatter in the final fabricated optic. The trapping of solution in these inclusions is due to poor mass transfer or pinning of elementary growth steps by impurity metal cations.[144–148] Better control of the solution mass transfer reduced liquid inclusions. His control was provided by:[149, 150]

    a. Modifying the platform rotation rates as a function of the different face sizes of the growing boule;

    b. Rapidly alternating the direction of rotation, thus accelerating the flow across the crystal faces;

c. Reducing the solution impurity cation concentration by using fluorinated coatings and liner barriers, high-purity raw materials, and ethylenediaminetetraacetic acid (EDTA) as an impurity getter.

3. **Controlling Crystal Habit**. Depending on the optic type (switch crystal, doubler, tripler), the size and aspect ratio of the final boule determines the number of optics it yields (Fig. 33). The final aspect ratio is governed by the overall relative growth rate of the prism and pyramid faces of the crystal. Several key mechanisms and behaviors were understood that aided in developing techniques to control the final crystal aspect ratio:

a. The influence that metallic cations have on the growth rate of prism and pyramid growth faces;

b. The influence of the dislocation number density on a growth face on the growth rate; and

c. The influence of temperature on the asymmetric growth rate of these faces.[148, 151, 152]

One problem in particular was control of impurities during the growth process. Many unwanted impurities are derived from the growth system glass containers and they can adversely affect the optical quality and aspect ratio (shape) of the crystals. Previous studies had shown that even trace concentrations ($\sim10^{-9}$ M) of impurities affect growth and even "insignificant" species can have a major impact. These studies also revealed that impurities affect the two growth faces of KDP very differently. Traces of trivalent metal impurities such as Fe^{3+}, Cr^{3+}, and Al^{3+} in solution are known to inhibit growth of the prismatic {100} faces of KDP while having little effect on the growth of the pyramidal {101} faces. This differentiation opened the possibility of intentionally adding

select ions to control the aspect ratio of the crystal to obtain a more advantageous shape. Prior to mid-2003, rapid growth of KDP crystals was performed in glass tanks. The presence of the glass solution interface allowed glass components to enter the growth solution. Trace elements from glass can influence the course of a growth run. The dissolution of the glass growth vessel made control of the exact chemical composition of the growth solution problematic. Since crystal growth habit is a function of trivalent cation concentration and the glass contained significant quantities of trivalent aluminum, determining the influence of process variables on growth geometry was difficult. Investigations begun in FY02 focused on control of impurities through the use of engineered barriers. In FY03 an FEP Teflon liner was developed and tested in large-scale experimentation. Since 2005, all rapid-growth KDP boules have been produced in Teflon-lined growth tanks (> 25 boules). The lining removed the problem of glass dissolution into the growth solution.

The first crystals grown in lined tanks had very low aspect ratios, which resulted in an unfavorable plate yield. The lined tanks allowed the exploration of the use of selective "impurity" addition to control the crystal aspect ratio. Aluminum was added to the growth solution at controlled levels without negatively affecting the material quality while improving the aspect ratio. Final resulting aspect ratio control techniques included the following:

 a. Using starting seeds of different aspect ratios to influence the final aspect ratio of the boule;

 b. Minimizing uncontrolled impurity levels (described above) and feeding controlled Al^{3+} impurities during the growth run; and

c. Incorporating an auxiliary tank of additional salt solution to allow for minimizing the temperature drop during growth, therefore minimizing variation in prismatic and pyramid growth faces.

In addition, a mathematical model for predicting the final aspect ratio of the boule based on its observed aspect ratio ~10 days into its growth was developed to aid in process adjustments during the growth run.[150,153–156]

4. **Preventing Boule Fracture.** Potassium di-hydrogen phosphate has a low fracture toughness (~0.1 MPa m$^{1/2}$) and high thermal expansion coefficient (~4×10^{-5} K^{-1}), resulting in poor thermal shock resistance and higher susceptibility to fracture. The boules were particularly susceptible to fracture at the end of a growth run when they were removed from the growth tank. At that time, the temperature differences between the interior of the crystal and its faces was the result of two contributing factors: a rapid drop in the temperature of the thermal environment around the boule as it was moved from the warm growth tank into the cooler room and the drop in the temperature of the crystal surfaces due to heat loss as the residual salt solution evaporated from the faces of the recently removed boule. Boule fractures were ultimately prevented by reducing the rate of temperature drop as the boule was brought to room temperature and by maintaining a high-humidity environment around the boule until room temperature was reached.[157, 158]

As rapid-growth tanks such as that shown in Fig. 34 were brought into production, a number of problems with yield were addressed and quickly solved. Initially, the formation of multiple spurious crystals was significantly reduced with the introduction of a streamlined, Halar®-coated, aluminum growth platform. With the Halar coating, the rotation rate could be

increased to provide faster and more uniform mass-transfer rates at all growing faces. With the

faster transfer rates, one of the problems with solution inclusions was significantly reduced. The

acceleration provided by rapidly alternating the direction of rotation prevented formation of

another type of inclusion that was associated with constant flow in one direction across the

crystal surface. Platform rotation rate was slowed when a crystal became very large to minimize

surface waves and associated splashing. An attempt was made to introduce polycarbonate growth

tanks to further improve the stability of conditions around the growing crystal. It was found,

however, that small bubbles in the polycarbonate wall interior would break open, resulting in

conditions favorable for growth of spurious crystals. Teflon liners for the growth tanks were

finally found to give the smoothest, least problematic wall conditions.

By the year 2000 a single growth supplier had been selected, and growth tanks at both

LLNL and CCI were put into production for growing enough crystals in time to meet the NIF

schedule. The boule shown in Fig. 35 was harvested from its tank in January 2001. After

growing for 52 days, it weighed in at 701 lb (a mass of 319 kg), with dimensions of 66.9 cm ×

52.9 cm × 59.4 cm on each side, yielding 14 SHG optics. A photograph of 7 harvested rapid-

growth KDP crystal boules is shown in Fig. 36.

When the issue of spurious nucleation was finally resolved through cooling and tank

over-pressurization, the focus shifted to maximizing the boule yield through improved control of

boule size and aspect ratio. The three main developments that helped control the aspect ratio

were listed in section V.D.1.3. Controlling Crystal Habit. The use of tall seeds combined with

controlled melt back and regrowth served to effectively set the growth aspect ratio early in the

growth process. Intentional doping with Al^{+3} impurities helped slow the growth of the prismatic

face relative to the pyramid, thus further improving the aspect ratio. Incorporation of an auxiliary

tank used to supply additional saturated KDP solution through the constant filtration system provided the means to supply additional KDP salt for crystal growth, as well as to maintain the growth system in the temperature regime determined to be the most favorable to maximize yield. Under these conditions the largest boule grown at LLNL was produced in 2005, with dimensions of 66.7 × 65.4 × 53.5 cm and weighing 347 kg (763 lb). This boule yielded 10 SHG crystals.

A significant parallel effort to use rapid-growth technology for production of tripler crystal boules of ~70% deuteration was also undertaken at LLNL. Although partially successful in producing NIF-sized boules, the resulting material did not routinely meet all NIF specifications, and the process was not suitable for commercialization. In the end, all of the DKDP material used in NIF for triplers and for some of the polarization rotators was grown using traditional techniques.

V.D.2 Relation between KDP growth and bulk damage

From prior experience at LLNL it was known that bulk damage could be a limiting mechanism for operation of an ICF laser at high energy. Thus, in parallel with development work on the growth of large crystal boules, studies were undertaken to look for possible relationships between boule growth conditions and the resistance of the crystal material to bulk damage. The immediate focus was on bulk rather than surface damage, because at that time, so many more bulk than surface sites were being formed. The resulting millions of bulk sites were capable of scattering an amount of light that would raise the spatial intensity contrast of the transmitted light and thus the risk of damage to downstream optics.

Bulk damage in KDP crystals occurs when precursors to damage are rapidly heated by the laser pulse, causing "mini-explosions". These result in small empty voids, called pin-points, which are surrounded by modified material. For NIF-like pulse durations, the diameter of the

voids is ~3 μm. As work started for NIF, the bulk damage resistance of available as-grown crystal material was below that needed for operation at design fluence levels for each of the wavelengths important for NIF, for 1ω, 2ω and 3ω. Images and more information on the characteristics of bulk damage are available in the paper "Damage Mechanisms Managed or Avoided for NIF Large Optics," also in this issue of *Fusion Science and Technology.*

From previous experience at LLNL, it was also known that the resistance of crystal optics to bulk damage could be significantly improved by first conditioning them with laser light.[159–161] During laser conditioning, a crystal optic is illuminated by a sequence of laser pulses with the fluence level of the first pulse set to just below that which will cause bulk damage at a density of ~10^{-3} /mm^3. Subsequent pulses in the sequence follow in a step-wise fashion with fluence steps of ~1 to 1.5 J/cm^2, up to a fluence level just below where the optic is expected to be used. The crystal optics used in all LLNL ICF lasers prior to NIF had been on-line conditioned.

Early in the NIF design phase (circa 1992) concerns about bulk damage motivated work toward a broader understanding of both bulk damage and possible alternate conditioning techniques.[162] This work was directed toward the PEPC switches operating at 1ω and the frequency converters needed for 2ω and 3ω. Fortunately, as the need for a better understanding of bulk damage became more urgent, much less expensive and easier to implement PC-based automation technology also became available. Study of bulk damage prior to that time, from the 1970s to the early 1990s, had been limited by the inherently slow nature of manual data collection and analysis. Newer automated systems had the ability to test hundreds of sites on test samples with results that could be readily displayed as S/1 and R/1 damage probability curves. A description of these types of probability curves and their interpretation is also included in the paper "Damage Mechanisms Managed and Avoided for NIF Large Optics" in this special issue

of *Fusion Science and Technology*. As work on rapid growth of crystals expanded, a dedicated automated test station was set up and operated solely to support this effort.

In the early to mid-1990s as large-scale, rapid-growth KDP crystal development was beginning, it was thought that bulk damage might be associated with hard particulates of absorbing materials that had been incorporated into the bulk of the crystals during the growth process. Diagnostics with micron resolution were built to test this theory but a correlation between embedded particulates and bulk laser damage was not observed except in cases of high particulate concentration.[163,164] During the same time frame, parametric studies of crystal growth were being conducted using small growth tanks with short turn-around cycles. These growth studies also provided a large number of crystal samples to evaluate in the search for correlations between the growth parameters and resistance to bulk damage. The parameter space for crystal growth included: temperature of the growth solution, impurity doping, solution filtration, the pattern of crystal rotation, platform material and others. Test samples from the small boules were fabricated into z- plates (the configuration for PEPC switch crystals), and into plates with the orientations of SHG and THG optics. The results of these tests indicated that the damage mechanism in KDP is considerably more complicated than can be explained by a simple absorber model. Specifically, it was discovered that:

1. THG and SHG crystals had approximately 1.5 times lower damage resistance than a z-cut optic[165]

2. Crystals grown at lower temperatures had higher damage resistance even in the presence of high concentrations of certain ionic impurities[166]

3. Variations in bulk damage resistance were found for different locations within a growing boule. This work and follow-on work with production material demonstrated that late-growth material had the highest damage resistance.[159]

Thermal annealing studies were also conducted. These studies showed that holding samples from the less-damage-resistant regions of KDP boules at 160°C for several hours could raise their damage resistance up to that of the late-growth material, but at the risk of material decomposition. As a result, thermal annealing was not recommended for NIF production of z-cut and SHG crystal optics. Fortunately, the variations related to location within the boule were small enough to be tolerated and good yield of optics from the KDP boules could still be obtained. After recognition that none of the alternatives studied to that date could reduce the importance of bulk damage for NIF operation, work intensified on investigating the parameters of laser conditioning.

A particularly important finding of the laser conditioning work centered on using a shorter wavelength laser to improve the damage resistance of crystal optics operating at a longer wavelength. As shown in Fig. 37 (a), it was found that 3ω conditioning of PEPC switch crystals would make them essentially damage proof at their 1ω use wavelength. The NIF project subsequently built two XeF-eximer-laser raster-scanned work stations (operating at 351 nm) for conditioning of all PEPC switch crystals, prior to their installation in NIF.[167]

Laser conditioning of crystals for use at 3ω was considerably more challenging. Conditioning at wavelengths shorter than 351 nm was found to induce bulk absorption via color center formation at impurity ions, thus shorter wavelength conditioning could not be used.[168] Further, conditioning with 3ω at higher fluence using pulse durations in the 3 to 20 ns range was

limited by surface damage.[169, 170] In 2002, a study was initiated to identify the optimum

pulselength for 3ω conditioning of crystal optics to be used at 3ω. The optimum pulse duration

was found to lie in the range between ~300 and ~900 ps, bounded on the short pulselength side

by the ability of the conditioning laser to deliver adequate energy and on the long pulselength

side by damage to the material being conditioned.[170] Although an approximately 500 ps off-line

pilot conditioning capability, called the SubNanosecond Laser (SNL) was demonstrated in 2007,

this station was not used in a production mode until recently.[171] Thus, as done previously for ICF

laser systems at LLNL, all frequency converter crystals in NIF were on-line conditioned as the

system was being brought into operation. Prudent start-up of such a large system involves

gradually increasing the operating point and on-line conditioning is a natural by-product of this

approach. Because each NIF bundle of 8 beams was brought up individually, if conditioning

were started at a very low fluence level and step sizes were chosen conservatively, on-line

conditioning would consume a large number of shots. In 2007, work began on an Absorption

Distribution Model (ADM) directed toward a better phenomenological understanding of bulk

damage and conditioning. The ADM is based on hypotheses about precursor behavior and

insights gained from a large data set of R/1 measurements for one particular crystal boule.[172, 173]

With empirical S/1 and R/1 data for all of the boules awaiting use in NIF, ADM provided

practical guidance for optimizing the on-line conditioning protocol to be used. As seen in Fig.

38, the selected protocol was able to accomplish on-line conditioning of both the doublers and

the triplers with only 5 conditioning shots compared to previous expectations that 9 conditioning

shots would be required. This more efficient on-line conditioning protocol was an important

contributor to meeting the tight commissioning schedule of NIF.

A number of off-line conditioning protocols were also experimentally evaluated for the doubler crystals. In operation, doubler crystal optics "see" 1ω light on their input side and a combination of 1ω and 2ω light at their output face. Figure 39 summarizes the results of conditioning tests for use of KDP at 2ω. Successful use of on-line conditioning of the doubler crystals in NIF is consistent with the black dots of Fig. 39 that give the bulk damage resistance imparted by conditioning with 2ω to 12 J/cm^2 using 3 ns pulses. This level of resistance to bulk damage is also quite similar to the 2ω protection provided by conditioning at 3ω with the 8.3 ns pulses (up to 10 J/cm^2) available from the excimer laser. (On Fig. 39, this graph line is identified as an "estimate" because the results were obtained for a similar but different sample plate of KDP). Protection for operation at 2ω with conditioning at 3ω was found to improve dramatically as the conditioning pulse duration was shortened, down to 300 ps. For example, if doublers were to be off-line conditioned on the SNL station, no bulk damage would be expected over the entire range of possible operational fluence levels, including those that might be encountered if NIF were to be operated in a pure 2ω mode. Fortunately, as NIF is being operated today at 3ω, the doubler crystals have proven to be very reliable and relatively damage free. For regular 3ω operation of NIF, there has been no need for replacing the doublers and thus no subsequent need for off-line conditioning of replacement doubler crystals.

The off-line SNL 3ω conditioning station is now being used to prepare pre-conditioned replacements for damaged tripler optics removed from NIF. Additional information regarding 3ω conditioning of crystals can also be found in the "Damage Mechanisms Managed or Avoided for NIF Large Optics" in this special issue of *Fusion Science and Technology*.[37]

V.D.3 Crystal Finishing

Potassium dihydrogen phosphate and DKDP crystals are not finished using the grinding and polishing techniques for glass optics described previously. Rather, crystals are first cut to just over their final size on a bandsaw, as shown in Fig. 40.

Next, they are finished with a single-point diamond tool set in a flywheel to skim cut the entire surface of the optic. Experience with this approach was first gained by LLNL engineers and transferred to CCI for delivery of the crystal optics for Nova. A specialized, 10,000-ft^2 fabrication facility was constructed at CCI for fabrication of crystals for NIF. The facility included fabrication equipment developed at LLNL capable of working with surfaces as large as 490 mm × 490 mm.[176] Design of a lightweight flycutter was instrumental in improving performance in the PSD-2 band (0.5–0.12 mm).[177] With these improvements, the optical quality of the finished surfaces was dramatically improved; the power spectral density (see Fig. 5) was improved by a factor of ten, significantly reducing the threat of damage to downstream optics.

The large diameter-to-thickness ratios of NIF optics, along with the low fracture toughness of KDP required the use of stringent temperature control during flycutting, while the high water solubility of KDP precluded the use of aqueous processing.[32] The NIF performance specifications were covered by both material homogeneity and finishing quality. The variation in impurity incorporation for the type of growth (prismatic vs. pyramidal) affects material homogeneity, influencing finishing quality. During the initial period of crystal fabrication, evaluation of the finished material noted the occurrence of fluorescent defects associated with subsequent laser damage in the THG (DKDP) crystals.[178] Investigation of the process parameters for flycutting of KDP and DKDP suggested that the occurrence of subsurface defects depended upon whether the material was being operated on in the ductile or brittle regime. Additionally, the transition from ductile to brittle material removal was found to occur at significantly different

finishing parameters depending upon growth method and crystal cut. The ductile to brittle transition occurs at the smallest chip thickness with rapid-growth SHG material. The rapid-growth THG material can tolerate a significantly larger chip thickness before encountering the transition zone, and the traditional-growth THG material an even larger chip thickness.[179] Implementation of a carefully defined cutting schedule developed between LLNL and CCI eliminated the occurrence of these types of defects in NIF finished crystals.

Also of concern during crystal finishing was the introduction of digs during the finishing process. Small particles of KDP material could become trapped between the vacuum chuck side of the crystal and the chuck lands, leading to small fractures (digs) caused by pressure non-uniformities introduced by KDP debris. The relationship between dig size and subsequent crystal damage was evaluated with eventual acceptance of criteria that allowed 300-micron digs on switch crystals, and digs less than 200 microns on frequency-conversion crystals.

V.D.4 KDP Crystal Antireflective Coatings

Potassium di-hydrogen phosphate and DKDP crystals used on the Nova laser were coated with a silica sol-gel AR coatings developed by LLNL.[13, 180] Sol-gel AR coatings have laser damage thresholds two to three times higher than other AR coatings, making them particularly appropriate for high-power laser operations.[13] Sol-gel coatings consist of a layer of porous quasi-spherical silica particles with diameters of ~30 nm. The optical thickness is tailored to the meet the requirements of the various surfaces being coated. Thus the switch crystals, which see only 1ω (1054-nm) light, require a 1/4 wavelength coating with an effective optical thickness of ~263 nm. The frequency conversion crystals, where the input and output surfaces of the crystals experience successively shorter wavelengths, require different coating thicknesses on the input and exit surfaces. Application of these coatings is performed using spin coating. In addition, the

output of the SHG and the input of the THG must be optimized to pass both 1053-nm and 525-nm light, requiring the use of a broadband AR coating. This compromise coating consists of a layer of UV-cured silicone topped with porous silica sol-gel.

Silica sol-gel AR coatings were also used on the fused silica optics; they were applied by dip coating followed by ammonia-curing to harden and crosslink the coating using a process developed by CEA.[181] When applied to crystals, this coating is relatively soft because it cannot be ammonia hardened due to sensitivity of the crystal surface to ammonia/water. The coating is also porous, allowing water to penetrate and react with the crystal surface.[182] Exposure to moisture (humid air) resulted in the formation of etch pits, causing scatter and degradation of optical performance.[183] Addition of a thermally cured silicone layer helped minimize etch-pit formation, but did not completely solve the problem. However, it did permit the use of a colloidal silica sol as a 1–2ω compromise coating, necessary on the SHG output and THG input.[184] Because of the thermal sensitivity of the KDP and especially the DKDP crystals, the thermal-cure process was replaced with a UV-cured silicone layer. Curing of the silicone layer was necessary to prevent intermixing of the silica sol AR when applied on top of the (uncured) silicone layer. Thermal annealing as a means to modify the surface characteristics of KDP to prevent etch-pit formation by forming a metaphosphate layer was explored, but it is only applicable to KDP.[185] Development of a hydrophobic colloidal silica sol resulted in significant resistance to etch-pit formation, while providing acceptable laser-damage resistance. Deuterated KDP crystals exposed to 55% relative humidity for several months did not form etch pits when coated with this hydrophobic silica sol-gel.[29] The hydrophobic sol-gel is produced by reacting the standard silica sol-gel with hexamethyl-disilazane (HMDS).[15] In this process HMDS reacts with the ~20-nm colloidal silica surfaces to form a very hydrophobic trimethylsilyl ($-Si(CH_3)_3$)

surface. The HMDS-treated coating resists vapor contamination of the pores and prevents water-condensation-induced etching of the KDP crystal surface.[186] See Ref. 29 for a detailed description of the development of AR coatings for KDP.

Like fused silica optics, sol-gel coating of crystal optics are characterized using ellipsometry to measure film thickness and refractive index thus allowing inference of spectral performance. Sol-gel coating defects on crystals, if present, are first identified using line-scan IMS and then further characterized for phase modulation using PSDI.[135]

V.E. Disposable Debris Shields

The NIF utilizes a relatively low-cost DDS as the final optic in the beamline to protect the GDS and the upstream optics from target debris, radiation, and contamination. For cost-effective NIF operation, DDS lifetimes of up to ten laser shots to targets are expected to protect the significantly more expensive FOA optics. Depending on the experimental program on NIF, as many as 8000 DDSs may be used each year, making the DDS over time the most used, and inevitably the most costly, optical component. Therefore, a viable low-cost solution to protecting the other high-value FOA optics was needed. The DDSs are thin (1–3 mm), borosilicate sheets with AR coatings on both sides. High-purity borosilicate glass was identified as a relatively low-cost DDS substrate that can deliver acceptable beam energy and focal spots to the target. Borosilicate glasses have acceptable optical transmission at 3ω, good resistance to thermal shock, and are commercially available at high volumes in sheet thicknesses and costs of interest for NIF.

V.E.1 DDS Blanks

The borosilicate glass used in NIF is called Borofloat® and is supplied by Schott AG. The float glass process used to produce the DDS glass is shown conceptually in Fig. 41. Molten

glass from a melting furnace is fed onto a bath of molten tin.[187, 188] The amount of glass is controlled by a tweel, or gate, that produces the "floated" ribbon of glass to have uniform thickness and relatively good flatness. The glass ribbon is then transported from the tin bath onto rollers where the roller speed determines its thickness. As the ribbon comes off the rollers, it is annealed in a lehr (temperature-controlled kiln) where internal stresses are relieved by a controlled rate of cooling. Upon exiting the lehr, the glass is cut into prescribed sheet sizes and inspected. To meet the NIF blank specifications, the glass melt is pre-selected for transmittance and purity, and the glass sheets are subsequently pre-screened for flatness (total thickness variation), surface and edge flaws, and bulk defects.

Borofloat® glass sheets typically exhibit very minor rippling or waviness that is attributed to vibrations experienced during the float process. However, because of the rippling, the sheets are not flat enough to meet NIF specifications; they require subsequent polishing to meet the transmitted wavefront specification. Specifically, the focal spot must meet the following requirements for encircled energy:

- 50% Encircled Energy Radius < 90 μm

- 80% Encircled Energy Radius < 132 μm

- 95% Encircled Energy Radius < 210 μm

The dominant wavefront error of the polished DDS consists of a focus term. This term is constrained to hold the shift of the focal spot to between -4 mm and 1 mm.

V.E.2 DDS Finishing

Finishing of the DDS sheets is done by Inabata (ULCOAT), a supplier that specializes in finishing similar thin glass substrates such as masks and photomask blanks for the semiconductor

industry as well as for flat panel displays for the electronic industry. Once the material removal was defined, Inabata demonstrated that their proprietary process was deterministic enough to meet the NIF DDS transmitted-wavefront requirements. With this process, Inabata is able to achieve high throughput rates on the order of several thousand DDSs per year.

V.E.3 DDS Coating

To minimize reflection of the DDS and meet NIF transmission requirements of $\geq$ 98% for 3.3-mm and $\geq$ 99% for 1.1-mm thicknesses, the optics are subsequently cleaned, and an AR coating (Refs. 15, 180, 190) is applied. The NIF worked with Schott North America to put in place a Class 100 cleanroom production facility (Fig. 42) capable of meeting the large volume demands for DDSs. This facility has the ability to clean and AR coat the finished DDSs. The cleaned and coated DDSs are also inspected for coating defects (Fig. 43), and Kapton® tape is applied around the perimeter of each optic (Fig. 44) to facilitate handling during cassette assembly. The tape also helps to contain the glass if the DDS breaks as a result of high-velocity impacts of target debris during laser shots.

Because the DDS sheets are thin, they can sag due to gravity, an issue especially pronounced for the 1.1-mm thickness optics. This sag can cause focusing ghost reflections that place other upstream optics upstream at risk. The impact of the reflected light, however, can be effectively managed by sorting the DDSs with respect to sag and grouping them properly for use in either upper- or lower-hemisphere locations in NIF. A metrology tool to determine sag was developed by LLNL and provided to Schott to measure all DDSs. The metrology tool can differentiate between high and low sag orientations of the glass, which allows Schott to serialize the DDS in a consistent orientation. The efforts at Schott to sort and serialize DDSs resulted in

considerable cost savings (labor and time) at LLNL where the final assembly of the DDSs into the automated cassettes (ADDS) and the final sag measurements were made.

At any given time a total of 1920 DDSs are installed on NIF (10 DDS per beamline). The yearly consumption of DDSs depends on the number and fluence of shots for NIF target experiments (i.e., the shot schedule). The operational experience to date on NIF gives an expected lifetime of 4 to 10 laser shots on targets. The criterion for removing a DDS is based on is its cumulative transmission loss. Although the major source of transmission loss comes from target debris impinging on the DDS, solarization due to an iron impurity in the glass and laser damage can also contribute. Currently, DDSs are replaced when the transmission is less than 95%, resulting in a relatively high annual consumption.

VI. SUMMARY AND CONCLUSIONS

To meet the cost, delivery schedule, and technical demands of NIF optics, a multiyear, multi-supplier effort was undertaken to develop the needed advanced optical materials, coatings, and novel fabrication technologies. The key results of this effort are listed below:

- Increased the optic fabrication rate (glass melting, finishing, coating) by approximately 10 times at reduced cost and with improved quality.

- Improved characterization of glass properties and developed new laser glass compositions, advanced glass-processing technology, and continuous optical glass melting technology.

- Manufactured laser damage-resistant dielectric mirrors and polarizers to stringent multi-wavelength reflection and transmission specifications.

- Improved understanding of the underlying tribology and fracture aspects of the grinding and polishing processes, including conditions responsible for the formation of surface defects.

- Developed quantitative methods for measuring the maximal depth-of-surface fractures present on ground and polished surfaces of brittle materials.

- Improved methods of inspecting optical elements for surface defects with formulation and application of defect attribution and scaling rules.

- Developed novel optical fabrication technologies using state-of-the-art grinding and deterministic figuring methods that incorporate iterative cycles of metrology and small-tool (CCOS and MRF) polishing.

- Improved fundamental understanding of laser-damage precursors responsible for damage initiation of fused silica optics when exposed to high-fluence 3ω light. Applied this knowledge to the manufacture of 3ω optics, resulting in a reduction in damage initiation by a factor of >10,000.

- Developed and applied holographic-based methods for the manufacture of large-format diffraction gratings.

- Developed and applied figuring-based methods for manufacture of large-format diffractive phase plates that incorporate continuously varying topology.

- Increased KDP boule growth rates by a factor of 10 using precise control of impurities and scientific understanding of the mechanisms controlling final crystal aspect ratio and optic yields.

- Improved understanding and control of finishing parameters affecting crystal surface damage.

- Developed a family of environmentally stable, laser damage resistant, sol-gel antireflection coatings for use on crystal (KDP) and glass (fused silica and borosilicate) optics.

- Developed relatively inexpensive disposable debris shield optics that effectively protect upstream optics from target debris damage.

- Designed, fabricated, and deployed production-compatible metrology tools to validate wavefront, spectral, laser-resistance, high-precision (0.01%), relative lens back focal length measurements and crystal-conversion tuning.

- Developed and implemented improved ergonomic techniques for handling large optics and processes to improve cleanliness during optics manufacture.

As a result of these and other improvements, NIF precision large optics were manufactured with better performance and at roughly a 5–20 times greater throughput than was achieved for Nova and Beamlet combined. The production step for the large NIF optics was completed by the beginning of 2009 to allow beamline commissioning to meet a major milestone for NIF to deliver half-energy (at least 1MJ). On March 10, 2009, NIF became the world's first megajoule laser facility by delivering 1.1 MJ of energy at 3ω (351 nm) to target chamber center using all 192 beams. Over the next three years the energy and power of NIF was systematically increased to its full design specifications. On July 5, 2012 the National Ignition Campaign conducted a symmetry capsule-implosion experiment with 192 NIF beams delivering over 1.852 MJ of energy with over a peak power of 500 TW in a precision shaped ignition pulse. This shot completed the commissioning of NIF for routine operations at its design specifications. More detailed information on the NIF design and a discussion of the function and performance of its

optical components can be found in accompanying articles entitled "Description of the NIF

Laser" and "National Ignition Facility Laser System Performance" in this special issue of *Fusion*

Science and Technology.[28, 191]

Appendix A. List of Abbreviations and Acronyms

Abb.	Definition	Abb.	Definition	Abb.	Definition
1-D	One Dimensional	HF	Hydrofluoric acid	PL	Polarizer
1ω	First harmonic (1053 nm)	HfO_2	Hafnia	PMI	Phase measuring interferometer
2-D	Two dimensional	ICF	Inertial confinement fusion		
2ω	Second harmonic (526.5 nm)	IMS	Image mapping system	PR	Polarization rotator
3-D	Three dimensional	IOM	Integrated optical module	PSD	Power spectral density
3ω	Third harmonic (351 nm)	IR	Infrared	PSDI	Phase shifting diffraction interferometer
ADDS	Automated disposable debris shield	ITT	International Telephone and Telegraph	Pt	Platinum
ADM	Absorption distribution model	KDP	Potassium dihydrogen phosphate	PV	Peak to valley
AGC	Ashai glass company	LAC	Large area conditioners	QA	Quality assurance
AMP	Advanced mitigation protocol	LGA	Laser glass amplifier	RMS	Root mean square
AR	Antireflective	LGDT	Laser glass damage test	RWF	Reflected wave front
BFL	Back focal length	LLE	Laboratory for Laser Energetics	SBS	Stimulated Brillion scattering
BOE	Buffered oxide etch	LLNL	Lawrence Livermore National Laboratory	SC	Switch crystal
CATS	Crystal alignment test system	LM1	Laser mirror 1	SF1	Spatial filter lens 1
CCI	Cleveland Crystal Incorporated	LM2	Laser mirror 2	SF2	Spatial filter lens 2
CCOS	Computer controlled optical surfacing	LM3	Laser mirror 3	SF3	Spatial filter lens 3
CDA	Clean dry air	LM4	Laser mirror 4	SF4	Spatial filter lens 4
CEA	Commissariat à l'énergie Atomique et aux énergies	LM5	Laser mirror 5	SHG	Single harmonic generator
CMM	Coordinate measuring machine	LM6	Laser mirror 6	SiO_2	Silica
CNC	Computer numerically controlled	LM7	Laser mirror 7	SIS	Slab inspection system
CPP	Continuous phase plate	LMJ	Laser MegaJoule	SNL	Sub-nanosecond laser
CSF	Cavity spatial filter	LOIS	Large optics inspection system	SRRS	Stimulation rotational Raman scattering
CVD	Chemical vapor deposition	LOTS	Lens optical test system	SRS	Stimulated Raman scattering
DBS	Diagnostic beam splitter	LPI	Laser plasma interactions	SSD	Smoothing by spectral dispersion
DDS	Disposable debris shield	MA	Main amplifier	SW	Switch window
DIS	Dig inspection system	MLS	Main laser system	TCC	Target chamber center
DKDP	Dueterated dihydrogen phosphate	MMS	Modulation measurement system	TCVW	Target chamber vacuum window
DOFAST	Diffractive optic full aperture System test	MRF	Magnetorheological finishing	THG	Third harmonic generator
DrD	Drive diagnostic	Nd	Neodymium	TIR	Total internal reflectance
EDTA	Ethylenediaminetetraacetic acid	NIF	National Ignition Facility	TSF	Transport spatial filter
ELID	Electrolytic in-situ dressing	NTE	Not to exceed	TWF	Transmitted wave front
ELV	Edge light verification	OAB	Optics assembly building	UV	Ultraviolet
FEP	Fluorinated ethylene propylene	OPF	Optical processing facility	VIS	Visible
FOA	Final optic assembly	OSP	Output sensor package	WFL	Wedged focus lens
FWHM	Full width half maximum	PA	Power amplifier		
GDS	Grating debris shield	PDS	Precision diagnostics system		
HDMS	Hexamethyl-disilazane	PEPC	Plasma electrode Pockels cell		

REFERENCES

1. E. I. MOSES, J. H. CAMPBELL, C. J. STOLZ, and C. R. WUEST, "The National Ignition Facility: The World's Largest Optics and Laser System," *Optical Engineering at the Lawrence Livermore National Laboratory, T. T. Saito and M. A. Lane, eds., Proc. SPIE*, **5001**, 1–15 (2003).

2. J. H. CAMPBELL, R. A. HAWLEY-FEDDER, C.J. STOLZ, J.A. MENAPACE, M.R. BORDEN, P.K. WHITMAN, J. YU, M.O. RILEY, M.D. FEIT, and R. P. HACKEL, "NIF Optical Materials and Fabrication Technologies: An Overview," *Proc. SPIE*, **5341**, 84–101 (2004).

3. M. A. RHODES, B. WOODS, J. J. DEYOREO, D. ROBERTS, and L. J. ATHERTON, "Performance of Large-Aperture Optical Switches for High-Energy ICF Lasers," *Appl. Opt*. **34**, 5313–5330 (1995).

4. J. GOLDHAR and M. A. HENESIAN, "Large-aperture Electrooptical Switches with Plasma Electrodes," *IEEE J. Quantum Electron*, **QE-22**, 1137–1147 (1986).

5. B. M. VAN WONTERGHEM, J. R. MURRAY, J. H. CAMPBELL, D. R. SPECK, C. E. BARKER, I. C. SMITH, D. F. BROWNING and W. C. BEHRENDT, "Performance of a Prototype for a Large-aperture Multi-pass Nd:glass Laser for Inertial Confinement Fusion," *Appl. Opt*., **36**, 4932, (1997).

6. T. G. PARHAM, C. J. STOLZ, T. BAISDEN, M. KOZLOWSKI, C. KIIKKA and D. M. AIKENS, "Developing Optics Finishing Technologies for the National Ignition Facility," *ICF Quarterly Report*, **9**, 177–191 (1999), Lawrence Livermore National Laboratory Report UCRL-LR-105821-99-20.

7. M. R. KOZLOWSKI, "Damage-Resistant Laser Coatings," *Thin Films for Optical Systems*, Marcel Dekker, Flory FR (Ed.), New York, pp. 521–549 (1995).

8. C. J. STOLZ, C. L. WEINZAPFEL, A. L. RIGATTI, J. B. OLIVER, J. TANIGUCHI, R. P. BEVIS, and J. S. RAJASANSI, "Fabrication of Meter-scale Laser Resistant Mirrors for the National Ignition Facility: A Fusion Laser," *Proc. SPIE*, **5193**, 50–58 (2003).

9. C. J. STOLZ and F. Y. GÉNIN, "Laser Resistant Coatings," *Optical Interference Coatings*, Springer Series in Optical Sciences, eds. N. Kaiser and H. Pulker, Springer-Verlag, Berlin Heidelberg (2003).

10. R. A. ZACHARIAS, N. R. BEER, E. S. BLISS, S. C. BURKHART, S. J. COHEN, S. B. SUTTON, R. L. VAN ATTA, S. E. WINTERS, J. T. SALMON, M. R. LATTA, C. J. STOLZ, D. C. PIGG, and T. J. ARNOLD, "Alignment and wavefront control systems of the National Ignition Facility," *Opt. Eng.*, **43**, 2873–2884 (2004).

11. J. B. OLIVER, J. HOWE, A. RIGATTI, D. J. SMITH, and C. J. STOLZ, "High Precision Coating Technology for Large Aperture NIF Optics," *Optical Interference Coatings*, OSA Technical Digest (Optical Society of America, Washington, DC), pp. ThD2-1 through ThD2-3 (2001).

12. C. J. STOLZ, C. L. WEINZAPFEL, G. T. ROGOWSKI, D. J. SMITH, A. RIGATTI, J. TANIGUCHI, M. VON GUNTEN, R. P. BEVIS, M. SMITH and V. IVAN, "Status of Optical Coatings for the National Ignition Facility," *Optical Interference Coatings*, OSA Technical Digest (Optical Society of America, Washington DC), pp. ThD3-1 through ThD3-3 (2001).

13. I. M. THOMAS, "High Laser Damage Threshold Porous Silica Antireflective Coating," *Applied Optics*, **25**, *9*, pp.1481–1483 (1986).

14. I. M. THOMAS, "Sol-gel Coatings for High Power Laser Optics—Past, Present and Future," *Proc. SPIE*, **2114**, 232–242 (1994).

15. T. I. SURATWALA, M. L. HANNA, E. L. MILLER, P. K. WHITMAN, I. M. THOMAS, P. R. EHRMANN, R. S. MAXWELL, and A. K. BURNHAM, "Surface Chemistry and Trimethylsilyl Functionalization of Stöber Silica Sols in Solution," *J. Non-Cryst. Sol*., **316**, 349–363 (2003).

16. P. WEGNER, J. AUERBACH, T. BIESIADA, S. DIXIT, J. LAWSON, J. MENAPACE, T. PARHAM, D. SWIFT, P. WHITMAN and W. WILLIAMS, "NIF Final Optics System: Frequency Conversion and Beam Conditioning," *Proc. SPIE*, **5341**, 180–189 (2004).

17. S. N. DIXIT, M. D. FEIT, M. D. PERRY, and H. T. POWELL, "Designing Fully Continuous Phase Screens for Tailoring Focal-plane Irradiance Profiles," *Optics Letters*, **21**, 1715–1717 (1996).

18. J. A. MENAPACE, S. N. DIXIT, F. Y. GENIN, and W. F. BROCIOUS, "Magnetorheological Finishing for Imprinting Continuous Phase Plate Structures onto Optical Surfaces," presented at Laser Induced Damage in Optical Materials, Boulder, CO, September 22, 2003, *Proc. SPIE*, **5273**, 220–230 (2003).

19. J. T. HUNT and D. R. SPECK, "Present and Future Performance of the Nova Laser System," *Opt. Eng*., **28**, 461–468 (1989).

20. J. K. LAWSON, C. R. WOLFE, K.R. MANES, J. B. TRENHOLME, D. M. AIKENS, R. E. ENGLISH, JR, "Specification of optical components using the power spectral density function," *Proc. SPIE*, **2536**, 38–50 (1995)

21. J. K. LAWSON, D. M. AIKENS, R. E. ENGLISH, JR., and C. R. WOLFE, "Power Spectral Density Specifications for High Power Lasers," *Proc. Soc. Photo-Opt. Instrum. Eng.* **2775**, 345 (1996).

22. J. K. LAWSON, J. M. AUERBACH, R. E. ENGLISH, JR, M. A. HENESIAN, J. T. HUNT, R. A. SACKS, J. B. TRENHOLME, W. H. WILLIAMS, M .J. SHOUP III, J.H. KELLY, and C. T. COTTON, "NIF Optical Specifications – The Importance of the RMS Gradient," *Proc. SPIE,* **3492**, 336–343 (1998).

23. C .J. WALSH, A. J. LEISTNER, and B. F. OREB, "Power spectral density analysis of optical substrates for gravitational-wave interferometry," *Appl. Opt.*, **38** (22), 4790–4801 (1999)

24. J. K. LAWSON, D. M. AIKENS, R. E. ENGLISH, JR., W. T. WHISTLER, W. HOUSE, and M. A. NICHOLS, "Surface Figure and Roughness Tolerances for NIF Optics and the Interpretation of the Gradient, P-V Wavefront, and RMS Specifications," *Optical Manufacturing and Testing III, H. Philip Stahl, Editor, Proc. SPIE*, **3782**, 510–517 (1999).

25. J.F. HOLZRICHTER, "Lasers and Inertial Fusion Experiments at Livermore." Lawrence Livermore Laboratory Report, UCRL-BOOK-218519 (January 2006).

26. M. L. SPAETH, K. R. MANES, C. C. WIDMAYER, W. H. WILLIAMS, P. K. WHITMAN, M. A. HENESIAN, I. F. STOWERS, and J. HONIG, "National Ignition Facility Wavefront Requirements and Optical Architecture," *Opt. Eng.*, **43**, 12, 2854–2865 (December 2004).

27. W.H. WILLIAMS, "NIF Large Optics Metrology Software: Description and Algorithms," UCRL-MA-137950, pp.1–39, Lawrence Livermore National Laboratory (Mar. 16, 2000).

28. M. L. SPAETH, K.R. MANES, D.H. KALANTAR, P.E. MILLER, J.E. HEEBNER, E.S. BLISS, D.R. SPECK, T.G. PARHAM, P.K. WHITMAN, P.J. WEGNER, P.A. BAISDEN, J.A. MENAPACE, M.W. BOWERS, S.J. COHEN, T.I. SURATWALA, J.-M. DI

NICOLA, M.A. NEWTON, J.J. ADAMS, J.B. TRENHOLME, R.G. FINUCANE, R. E. BONANNO, D.C. RARDIN, P.A. ARNOLD, S.N. DIXIT, G.V. ERBERT, A.C. ERLANDSON, J.E. FAIR, E. FEIGENBAUM, W.H. GOURDIN, R.A. HAWLEY, J. HONIG, R.K HOUSE, K.S. JANCAITIS, D.W. LARSON, B.J. LE GALLOUDEC, J.D. LINDL, B.J. MACGOWAN, C.D. MARSHALL, K.P. MCCCANDLESS, R.W. MCCRACKEN, R.C. MONTESANTI, E.I. MOSES, M.C. NOSTRAND, J.A. PRYATEL, V.S. ROBERTS, S.B. RODRIGUEZ, R.A. SACKS, J.T. SALMON, M.J. SHAW, S. SOMMER, C.J. STOLZ, R. ZACHARIAS, "Description of the NIF Laser," this issue of *Fusion Science and Technology.*

29.   J. J. DEYOREO, A. K. BURNHAM, and P. K. WHITMAN, "Developing KH2PO4 and KD2PO4 Crystals for the World's Most Power Laser," *International Materials Review*, **47**, 113−152 (2002).

30.   N. ZAITSEVA and L. CARMAN, "Rapid Growth of KDP-type Crystals," *Prog. Cryst. Growth Charact. Mater.*, **43**, 1−118 (2001).

31.   F. L. RAVIZZA, "Imaging of phase objects using partially coherent illumination," LLNL-TH-648062, Master's Thesis, University of Arizona (2013).

32.   R. HAWLEY-FEDDER, P. GERAGHTY, S. LOCKE, M. MCBURNEY, M. RUNKEL, T. SURATWALA, S. THOMPSON, P. WEGNER, and P. WHITMAN, "NIF Pockels Cell and Frequency Conversion Crystals," *Proc. SPIE*, **5341**, 121−126 (2004).

33.   S. SCHWARTZ, R. T. JENNINGS, J. F. KIMMONS, R. P. MOUSER, C. L. WEINZAPFEL, M. R. KOZLOWSKI, C. J. STOLZ, and J. H. CAMPBELL, "Vendor-Based Laser Damage Metrology Equipment Supporting the National Ignition Facility," *Solid State Lasers for*

Application to Inertial Confinement Fusion, W. Howard Lowdermilk, ed., *Proc. SPIE*, **3492**, 933–938 (1999).

34. W. W. SIMMONS and R. O. GODWIN, "Nova Laser Fusion Facility—Design, Engineering and Assembly Overview," *Nuclear Technol. Fusion*, **4**, 8–24 (1983).

35. J. LINDL, *Inertial Confinement Fusion: The Quest for Ignition and Energy Gain Using Indirect Drive,* Springer-Verlag (1998).

36. J. H. CAMPBELL, T. I. SURATWALA, C. B. THORSNESS, J. S. HAYDEN, A. J. THORNE, J. M. CIMINO, A. J. MARKER III, K. TAKEUCHI, M. SMOLLEY, and G. F. FICINI-DORN, "Continuous Melting of Phosphate Laser Glasses," *Journal of Non-Crystalline Solids, 263&264, 342–357 (2000).

37. K. R. MANES, M. L. SPAETH, J.J. ADAMS, M.W. BOWERS, J.D. BUDE, C.W. CARR, A.D. CONDER, D.A. CROSS, S.G. DEMOS, J.M.G. DINICOLA, S.N. DIXIT, E. FEIGENBAUM, R.G. FINUCANE, G.M. GUSS, M.A. HENESIAN, J. HONIG, D.H. KALANTAR, L.M. KEGELMEYER, Z.M. LIAO, B.J. MACGOWAN, M.J. MATTHEWS, K.P. MCCANDLESS, N.C. MEHTA, P.E. MILLER, R.A. NEGRES, M.A. NORTON, M.C. NOSTRAND, C.D. ORTH, R.A. SACKS, M.J. SHAW, L.R. SIEGEL, C.J. STOLZ, T.I. SURATWALA, J.B. TRENHOLME, P.J. WEGNER, P.K. WHITMAN, C.C. WIDMAYER, and S.T. YANG, "Damage Mechanisms Avoided or Managed for NIF Large Optics," this issue of *Fusion Science and Technology.*

38. M. L. SPAETH, P. J. WEGNER, T. I. SURATWALA, M. C. NOSTRAND, J. D. BUDE, A. D. CONDER, J.A. FOLTA, J. E. HEEBNER, L.M. KEGELMEYER, B. J. MACGOWAN, D. C. MASON, M. J. MATTHEWS, and P. K. WHITMAN, "Optics Recycle Loop

Strategy For NIF Operations Above UV Laser-Induced Damage Threshold, this issue of *Fusion Science and Technology*."

39. J. H. CAMPBELL and T. I. SURATWALA, "Nd-doped Phosphate Glasses for High-Energy/High Peak Power Lasers," Journal of Non-Crystalline Solids, 263&264, 318–341 (2000).

40. J. -L. MIQUEL, C. LION and P. VIVINI, "The LMJ program: Overview and Status of LMJ & PETAL Projects, *CLEO:2013*, OSA Technical Digest (online), Optical Society of America, San Jose, California, pp. ATu1M.4.

41. J. CAMPBELL, E. WALLERSTEIN, J. HAYDEN, D. SAPAK, D. WARRINGTON, A. MARKER, H. TORATANI, H. MEISSNER, S. NAKAJIMA, T. IZUMITANI, "Elimination of Platinum Inclusions in Phosphate Laser Glasses" UCRL-53932 Lawrence Livermore National Laboratory Report (1989).

42. J. CAMPBELL, "Modeling Platinum-Inclusion Dissolution in Phosphate Laser Glasses," *Glasstech. Ber. Glass Sci. Technol.*, **68**, 96–101 (1995).

43. M. KARABULUT, T. SURATWALA, G. MARASINGHE, C. CLICK, E. METWALLI, R. BROW, C. BOOTH, J. BUCHER, D. SHUH, T. SURATWALA, and J. CAMPBELL, "XAFS Investigation of Platinum Impurities in Phosphate Glasses," *Journal of the American Ceramic Society*, **85**, 5, 1093–1099 (2002).

44. C. CLICK, E. METWALLI, M. KARABULUT, R. BROW, T. SURATWALA, and J. CAMPBELL, "Platinum Dissolution into Phosphate Melts," *19th International Congress on Glass. Soc. Glass Technol.*, Edinburgh, Scotland, pp. 237–238 (2001).

45. T. I. SURATWALA, J. H. CAMPBELL, P. E. MILLER, C. B. THORSNESS, M. O. RILEY, P. R. EHRMANN, and R. A. STEELE, "Phosphate Laser Glass for NIF: Production Status, Slab Selection and Recent Technical Advances," *Proc. SPIE*, **5341**, 102–113 (2004).

46. C.B. THORSNESS, T. SURATWALA, R.A. STEELE, J. H. CAMPBELL, J. S. HAYDEN, S. A. PUCILOWSKI, and K. SUZUKI, "Dehydroxylation of Phosphate Laser Glass," *Proc. SPIE*, **4102**, 175–194 (2000).

47. C. CLICK, W. REICHMAN, R. BROW, P. EHRMANN, T. SURATWALA, and J. CAMPBELL, "Influence of Hydroxyl Contamination on Neodymium Fluorescence Lifetime in Potassium-Magnesium Alumino-Metaphosphate Glasses," *Glass Science and Technology Suppl.*, **75**, 215–220 (2002).

48. J. S. HAYDEN, A. J. MARKER III, T. I. SURATWALA, and J. H. CAMPBELL, "Surface Tensile Layer Generation during Thermal Annealing of Phosphate Glass," *Journal of Non-Crystalline Solids*, **263&264**, 228–239 (2000).

49. S. CRICHTON, M. TOMOZAWA, J. HAYDEN, T. SURATWALA, and J. CAMPBELL, "Sub-Critical Crack Growth in a Phosphate Laser Glass," *Journal of the American Ceramic Society*, **82**, 11, 3097–3104 (1999).

50. T. SURATWALA, R. A. STEELE, G. D. WILKE, and J. H. CAMPBELL, "Effects of OH Content, Water Vapor Pressure, and Temperature on Sub-Critical Crack Growth In Phosphate Glass," *Journal of Non-Crystalline Solids*, **263&264**, 213–227 (2000).

51. T. I. SURATWALA, J. H. CAMPBELL, P. E. MILLER, C. B. THORSNESS, M. O. RILEY, P. R. EHRMANN, and R. A. STEELE, "Phosphate Laser Glass for NIF: Production Status, Slab Selection and Recent Technical Advances," *Proc. SPIE*, **5341**, 102–113 (2004).

52. J. H. CAMPBELL and T. I. SURATWALA, "Nd-doped Phosphate Glasses for High-Energy/High Peak Power Lasers," *Journal of Non-Crystalline Solids*, **263&264**, 318–341 (2000).

53. P. R. EHRMANN, J. H. CAMPBELL, T. I. SURATWALA, J. S. HAYDEN, D. KRASHKEVICH, and K. TAKEUCHI, "Optical Loss and Nd^{3+} Non-Radiative Relaxation by Cu, Fe, and Several Rare Earth Impurities in Phosphate Laser Glasses," *Journal of Non-Crystalline Solids*, **263&264**, 251–262 (2000).

54. J. H. CAMPBELL, J.F. KIMMONS, and S.SCHWARTZ., "Platinum particle detection in pohosphate laser glasses," Chapter 6, *Analysis of Composition and Structure of Glass and Glass Ceramics*, Vol. 7 H. BACK and D. KRAUSE, Editors, Berlin,(Springer-Verlag, 1999).

55. T. SURATWALA, C. THORSNESS, J. CAMPBELL, S. KRENITSKY, J. CIMINO, A. THORNE, J. HAYDEN, K. TAKEUCHI, K. SUZUKI, and K. YAMAMOTO, "Technical Advances in the Continuous Melting of Phosphate Laser Glass," Inertial Fusion and Sciences Applications (IFSA2001), 540–543 (2002).

56. H. POWELL, M. RILEY, C. WOLFE, R. LYONS, J. CAMPBELL, E. JESSOP, and J. MURRAY, "Composite Polymer-Glass Edge Cladding for Laser Disks," U.S. Patent 4,849,036 (1989).

57. T. SURATWALA, P. MILLER, P. EHRMANN, and R. STEELE, "Polishing Slurry Induced Surface Haze on Phosphate Laser Glasses," *Journal of Non-Crystalline Solids*, **351**, 2091–2101 (2005).

58. B. TISCHENDORF, "Interactions between Water and Phosphate Glasses," T8847, Dissertation, U. of Missouri-Rolla (2005).

59. C. J. STOLZ, J. ADAMS, M. D. SHIRK, M. A. NORTON, and T. L. WEILAND, "Engineering Meter-Scale Laser Resistant Coatings for the Near IR," in *Advances in Optical Thin Films II*, C. Amra, N. Kaiser, and H.A. Macleod, eds., *Proc. SPIE*, **5963**, 59630Y-1-8 (2005).

60. R. BOLAND, "Computer Control and Process Monitoring of Electrolytic In-Process Dressing of Metal Bond Fine Diamond Wheels for NIF Optics," in *Optical Manufacturing and Testing III*, H. Philip Stahl, ed., *Proc. SPIE*, **3782**, 61–69 (1999).

61. H. OHMORI, "Electrolytic In-Process Dressing (ELID) Grinding Technique for Ultra-Precision Mirror Surface Machining," *International Journal of the Japan Society for Precision Engineering*, **26**, 273–278 (1992).

62. L. N. ALLEN and H. W. ROMIG, "Demonstration of an Ion Figuring Process," in *Advanced Optical Manufacturing and Testing*, Gregory M. Sanger; Paul B. Reid; Lionel R. Baker, eds., *Proc. SPIE*, **1333**, 22–33 (1990).

63. C. J. STOLZ, M. D. THOMAS, and A. J. GRIFFIN, "BDS Thin Film Damage Competition" in *Laser-Induced Damage in Optical Materials: 2008*, G.J. Exarhos, D. Ristau, M.J. Soileau, C.J. Stolz, eds., *Proc. SPIE*, **7132**, 71320C-1-6 (2009).

64. D. J. SMITH, J. F. ANZELLOTTI, A. W. SCHMID, S. PAPERNOV, Z. R. CHRZAN, and S. J. VAN KERKHOVE, "Damage Fluence at 1054 nm and 351 nm of Coatings Made with Hafnium Oxide Evaporated from Metallic Hafnium," in *Laser-Induced Damage in Optical Materials: 1994*, H. E. Bennett, L. L. Chase, A. H. Guenther, B. E. Newnam, and M. J. Soileau, eds., *Proc. Soc. Photo-Opt. Instrum. Eng.*, **2428**, 319 (1995).

65. C. J. STOLZ, L. M. SHEEHAN, M. K. VON GUNTEN, R. P. BEVIS, and D. J. SMITH, "The Advantages of Evaporation of Hafnium in a Reactive Environment to Manufacture

High Damage Threshold Multilayer Coatings by Electron-Beam Deposition," in *Advances in Optical Interference Coatings*, C. Amra and H. A. Macleod, eds., *Proc. Soc. Photo-Opt. Instrum. Eng.*, **3738**, 318–324 (1999).

66.   M. R. KOZLOWSKI , C. R. WOLFE, M. C. STAGGS, and J. H. CAMPBELL, "Large Area Laser Conditioning of Dielectric Thin Film Mirrors," in *Laser-Induced Damage in Optical Materials: 1989*, H. E. Bennett, L. L. Chase, A. H. Guenther, B. E. Newnam, and M. J. Soileau, eds., *Proc. Soc. Photo-Opt. Instrum. Eng.*, **1438**, 376–390 (1989).

67.   A. FORNIER, C. CORDILLOT, D. AUSSERRE, and F. PARIS, "Laser Conditioning of Optical Coatings: Some Issues in the Characterization by Atomic Force Microscopy," in *Laser-Induced Damage in Optical Materials: 1993*, H. E. Bennett, L. L. Chase, A. H. Guenther, B. E. Newnam, and M. J. Soileau, eds., *Proc. Soc. Photo-Opt. Instrum. Eng.*, **2114**, 355–365 (1994).

68.   A. B. PAPANDREW, C. J. STOLZ, Z. L. WU, G. E. LOOMIS, and S. FALABELLA, "Laser Conditioning Characterization and Damage Threshold Prediction of Hafnia/Silica Multilayer Mirrors By Photothermal Microscopy," in *Laser-Induced Damage in Optical Materials: 2000*, G. J. Exarhos, A. H. Guenther, M. R. Kozlowski, K. L. Lewis, and M. J. Soileau, eds., *Proc. SPIE*, **4347**, 53–61, (2001).

69.   C. J. STOLZ, L. M. SHEEHAN, S. M. MARICLE, S. SCHWARTZ, and J. HUE, "A Study of Laser Conditioning Methods of Hafnia Silica Multiplayer Mirrors," in *Laser-Induced Damage in Optical Materials: 1998*, G. J. Exarhos, A. H. Guenther, M. R. Kozlowski, K. L. Lewis, and M. J. Soileau, eds., *Proc. SPIE*, **3578**, 144–152 (1999).

70.   C. J. STOLZ, M. RUNKEL, M. S. MCBURNEY, R. E. CHEEK, and J. A. MENAPACE, "Metrology of Mirrors for the National Ignition Facility," in *Optical Engineering at LLNL*

II: The National Ignition Facility, C. R. Wuest and M. A. Lane, eds., *Proc. SPIE*, **5341**, 114–120 (2004).

71.   H. LEPLAN, B. GEENEN, J. Y. ROBIC, and Y. PAULEAU, "Residual Stresses in Silicon Dioxide Thin Films: Correlation with Deposition Parameters and Aging Behavior," *J. Appl. Phys.*, **78**, 962–967 (1995).

72.   J. F. ANZELLOTTI, D. J. SMITH, R. J. SCZUPAK, AND Z. R. CHRZAN, "Stress and Environmental Shift Characteristics of HfO_2/ SiO_2 Multilayer Coatings," in *Laser-Induced Damage in Optical Materials: 1996*, H. E. Bennett, A. H. Guenther, M. R. Kozlowski, B. E. Newnam, and M. J. Soileau, eds., *Proc. SPIE*, **2966**, 258–264 (1997).

73.   C. J. STOLZ, J. A. MENAPACE, F. Y. GÉNIN, P. R. EHRMANN, P. E. MILLER, and G. T. ROGOWSKI, "Influence of BK7 Substrate Solarization On The Performance Of Hafnia And Silica Multilayer Mirrors," in *Laser-Induced Damage in Optical Materials: 2002*, G. J. Exarhos, A. H. Guenther, M. R. Kozlowski, K. L. Lewis, M. J. Soileau, and C. J. Stolz, eds., *Proc. SPIE*, **4932**, 38–47, (2003).

74.   T. I. SURATWALA, J. H. CAMPBELL, W. A. STEELE, AND R. A. STEELE, "Fail-Safe Design For Square Vacuum-Barrier Windows" *Proc. SPIE*, *Third International Conference on Solid State Lasers for Application to Inertial Confinement Fusion*, **3492**, 740 (July 23, 1999).

75.   M. A. RHODES, S. FOCHS, P. BILTOFT, T. ALGER, B. FUNKHOUSER, C. I. BOLEY, "Plasma Electrode Pockels Cell For The National Ignition Facility," *Proc. SPIE, Third International Conference on Solid State Lasers for Application to Inertial Confinement Fusion*, **3492**, 144–147 (July 1999).

76. P. A. ARNOLD; C. W. OLLIS; A. F. HINZ; C. L. ROBB; K. A. PRIMDAHL; J. J. WATSON; M. D. O'BRIEN; W. G. FUNKHOUSER; P. J. BILTOFT; R. T. SHELTON; W. C. TAPLEY; and W. J. DEHOPE, "Deployment, Commissioning, And Operation Of Plasma Electrode Pockels Cells in the National Ignition Facility," *Proc. SPIE, Commercial and Biomedical Applications of Ultrafast Lasers IV*, **5341**, 156–167 (May 2004).

77. J. PAISNER AND J. R. MURRAY, "Overview of the National Ignition Facility Project," *Proc. SPIE Conf. Solid-State Laser Apps. To ICF*, Monterey, CA, 1998.

78. P. J. WEGNER, J. M. AUERBACH, T. A. BIESIADA, JR., S. N. DIXIT, J. K. LAWSON, J. A. MENAPACE, T. G. PARHAM, D. W. SWIFT, P. K. WHITMAN, and W. H. WILLIAMS, "NIF Final Optics System: Frequency Conversion And Beam Conditioning", *Proc. SPIE, Optical Engineering at the Lawrence Livermore National Laboratory II: The National Ignition Facility*, **5341**, 180 (May 28, 2004) .

79. C. A. HAYNAM, P. J. WEGNER, J. M. AUERBACH, M. W. BOWERS, S. N. DIXIT, G. V. ERBERT, G. M. HEESTAND, M. A. HENESIAN, M. R. HERMANN, K. S. JANCAITIS, K. R. MANES, C. D. MARSHALL, N. C. MEHTA, J. MENAPACE, E. MOSES, J. R. MURRAY, M. C. NOSTRAND, C. D. ORTH, R. PATTERSON, R. A. SACKS, M. J. SHAW, M. SPAETH, S. B. SUTTON, W. H. WILLIAMS, C. C. WIDMAYER, R. K. WHITE, S. T. YANG, AND B. M. VAN WONTERGHEM, "National Ignition Facility laser performance status", *Applied Optics,* **46**, 3276–3303 (June 2007).

80. H.T. POWELL, S.N. DIXIT, M.A. HENESIAN, "Beam-Smoothing Capability of the Nova Laser," UCRL-LR-105821-91-1, *ICF Quarterly Report*, Oct.-Dec, 1990

81. Private Communication of calculated images by S.N. DIXIT, NIF Program Responsible Individual for CPP design and analysis, (March 2015)

82. J. H. CAMPBELL, J. S. HAYDEN, AND A. MARKER, "High-Power Solid-State Lasers: A Laser Glass Perspective," *International Journal of Applied Glass Science*, **2**, 3–29 (2011).

83. CORNING INCORPORATED, Semiconductor Glass Business, 334 County Route 16, Canton, NY 13617.

84. SCHOTT NORTH AMERICA, 400 York Avenue, Duryea, PA. 18642.

85. HEREAUS QUARTZ AMERICA LLC, 100 Heraeus Blvd. Buford, Ga 30518

86. ASHAI GLASS, 11175 Cicero Dr. Suite 400, Alpharetta, GA 30022.

87. M. HERCHER, "Laser-Induced Damage in Transparent Media," *Journal of the Optical Society of America*, **54**, 563 (1964).

88. A. M. RUBENCHIK and M. D. FEIT, "Initiation, Damage in Growth, and Mitigation of UV Laser-Induced Fused Silica," *Proc. SPIE*, **4679**, 79–95 (2002).

89. B.C. STUART, M. D. FEIT, S. HERMAN, A. M. RUBENCHIK, B. W. SHORE, and M. D. PERRY, "Nanosecond-to-Femtosecond Laser-Induced Breakdown in Dielectrics," *Phys. Rev. B* **53**, 1749 (1996).

90. J. H. CAMPBELL, "Damage Resistant Optical Glasses for High Power Lasers: A Continuing Glass Science and Technology Challenge," *Glass Sci. Technol.*, **75**, C1, 91–108 (2003).

91. M. C. NOSTRAND; C. J. CERJAN; M. A. JOHNSON; T. I. SURATWALA; T. L. WEILAND; W. D. SELL; J. L. VICKERS; R. L. LUTHI; J. R. STANLEY; T. G. PARHAM; C. B. THORSNESS, "Correlation of Laser-Induced Damage To Phase Objects In Bulk Fused Silica," *Proc. SPIE, Laser-Induced Damage in Optical Materials*, **5647**, 233 (2004).

92. P. E. MILLER, T. SURATWALA, J. BUDE, N. SHEN, W. STEELE, T. LAURENCE, M. FEIT, AND L. WONG, "Methods for Globally Treating Silica Optics To Reduce Optical Damage," US Patent No. 8313662, granted November 20, 2012.

93. T. SURATWALA, P. E. MILLER, J. BUDE, W. STEELE, N. SHEN, M. MONTICELLI, M. FEIT, T. LAURENCE, M. NORTON, C. CARR, AND L. WONG, "HF-Based Etching Processes For Improving Laser Damage Resistance Of Fused Silica Optical Surfaces," *J. Am. Ceram. Soc.*, **94**, 2, 416–428 (2011).

94. J. BUDE, P. E. MILLER, S. BAXAMUSA, N. SHEN, T. LAURENCE, W. STEELE, T. SURATWALA, L. WONG, W. CARR, D. CROSS, AND M. MONTICELLI, "High Fluence Laser Damage Precursors And Their Mitigation In Fused Silica," *Optics Express*, **22**, 5, 5839–5851 (2014)

95. W. CARR, J. BUDE, and P. DEMANGE, "Laser-Supported Solid-State Absorption Fronts In Silica," *Phys. Rev. B: Condens. Matter*, **82**, 184303 (2010).

96. N. SHEN, J. BUDE, AND C. W. CARR, "Model Laser Damage Precursors For High Quality Optical Materials," *Optics Express*, **22**, 3393–3404 (2014).

97. D. W. CAMP, M. R. KOZLOWSKI, L. M. SHEEHAN, M. NICHOLS, M. DORVIK, R. RAETHER, and I. THOMAS, "Subsurface Damage and Polishing Compound Affect the 355-nm Laser Damge Threshold of Fuse Silica Surfaces," *Proc. SPIE*, **3244** (1997).

98. P. E. MILLER, T. I. SURATWALA, J. D. BUDE, T. A. LAURENCE, N. SHEN, W. A. STEELE, M. D. FEIT, J. A. MENAPACE, and L. L. WONG, "Laser Damage Precursors In Fused Silica," *Proc. SPIE*, **7504**, 75040X (2009).

99. J. NEAUPORT, L. LAMAIGNERE, H. BERCEGOL, F. PILON, and J. C. BIROLLEAU, "Polishing-Induced Contamination of Fused Silica Optics and Laser Induced Damage Density at 351 nm," *Opt. Express*, **13**, 25, 10163–10171 (2005).

100. P. E. MILLER, J. BUDE, T. SURATWALA, N. SHEN, T. LAURENCE, W. STEELE, J. MENAPACE, M. FEIT, and L. WONG, "Fracture-Induced Subbandgap Absorption as a Precursor to Optical Damage on Fused Silica Surfaces," *Opt. Lett.*, **35**, 16, 2702–2704 (2010).

101. T. LAURENCE, J. BUDE, N. SHEN, T. FELDMAN, P. E. MILLER, W. STEELE, and T. SURATWALA, "Metallic-Like Photoluminescence and Absorption in Fused Silica Surface Flaws," *Appl. Phys. Lett.*, **94**, 151114 (2009).

102. S. BAXAMUSA, P. E MILLER, L. WONG, N. SHEN, R. STEELE, J. BUDE, D. CROSS, and W. CARR, "Mitigation of Organic Laser Damage Precursors from Chemical Processing of Fused Silica," *Optics Express*, **22**, 24, 29568–29577 (2014).

103. M. A. NORTON, L. W. HRUBESH, Z. WU, E. E. DONOHUE, M. D. FEIT, M. R. KOZLOWSKI, D. MILAM, K. P. NEEB, W. A. MOLANDER, A. M. RUBENCHIK, W. D. SELL, and P. WEGNER, "Growth of Laser Initiated Damage in Fused Silica at 351 nm," *Proc. SPIE*, **4347**, 468 (2001).

104. M. A. NORTON, E. E. DONOHUE, M. D. FEIT, R. P. HACKEL, W. G. HOLLINGSWORTH, A. M. RUBENCHIK, and M. L. SPAETH, "Growth of Laser Damage in SiO_2 under Multiple Wavelength Irradiation," *Proc. SPIE*, **5991**, 599108 (2005).

105. R. A. NEGRES, M. A. NORTON, D. A. CROSS, and C. W. CARR, "Growth Behavior of Laser-Induced Damage on Fused Silica Optics under UV, ns Laser Irradiation," *Opt. Express*, **18**, 19966–19976 (2010).

106. H. H. KAROW, *Fabrication Methods for Precision Optics*, Wiley-Interscience (1992).

107. D. MALACARA, ed., *Optical Shop Testing, 2nd Edition*, Wiley-Interscience (1991).

108. F. W. PRESTON, "The Structure of Abraided Glass Surfaces," *Trans. of the Optical Soc.*, **23**, 141–164 (1921-1922).

109. J. C. LAMBROPOULOS, "From Abrasive Size to Subsurface Damage in Grinding," *OSA Technical Digest*, 17–18 (2000).

110. F. K. ALEINIKOV, "The Effect of Certain Physical and Mechanical Properties on the Grinding of Brittle Materials," *Sov. Phys. Tech. Phys.*, **27**, 2529–2538 (1957).

111. D.F. EDWARDS and P.P. HED, "Optical Glass Fabrication Technology II: The Relationship Between Surface Roughness and Subsurface Damage," *Appl. Optics*, **26**, 4677–4680 (1987).

112. P. E. MILLER, T. SURATWALA, L. WONG, M. FEIT, J. MENAPACE, P. DAVIS, and R. STEELE, "The Distribution of Subsurface Damage in Fused Silica," *Proc. SPIE*, **5991** (2005).

113. T. SURATWALA, L. WONG, P. E MILLER, M. FEIT, J. MENAPACE, R. STEELE, P. DAVIS, and D. WALMER, "Sub-Surface Mechanical Damage Distributions During Grinding of Fused Silica," *Journal of Non-Crystalline Solids*, **352**, 5601 (2006).

114. J. MENAPACE, P. DAVIS, R. STEELE, L. WONG, T. SURATWALA, and P.E. MILLER, "Utilization of Magnetorheological Finishing As A Diagnostic Tool For Investigating the Three-Dimensional Structure of Fractures in Fused Silica," *Proc. SPIE*, **5991**, 599102 (2005).

115. T. SURATWALA, R. STEELE, M. FEIT, L. WONG, P.E. MILLER, J. MENAPACE, and P. DAVIS, "Effect of Rogue Particles on the Sub-Surface Damage of Fused Silica During Grinding/Polishing," *Journal of. Non-Crystalline Solids*, **354**, 2023–2037 (2008).

116. B. LAWN, *Fracture of Brittle Solids, Second Edition*, Cambridge Solid State Science Series, Cambridge University Press, New York (1993).

117. I. M. HUTCHINGS, *Tribology: Friction and Wear of Engineering Materials*, Butterworth/Heinmann (1992).

118. DYLLA-SPEARS, M. FEIT, P. E. MILLER, W. STEELE, T. SURATWALA, and L. WONG, "Method for Preventing Agglomeration of Charged Colloids Without Loss of Surface Activity," U.S. Provisional Patent Application IL-12647 (October 2012).

119. R. DYLLA-SPEARS, L. WONG, P. MILLER, M. FEIT, W. STEELE, T. SURATWALA, "Charged Micelle Halo Mechanism for Agglomeration Reduction in Metal Oxide Polishing Slurries" *Colloids and Surfaces A: Physicochem. Eng. Aspects*, **447**, 32–43 (2014).

120. L. L. WONG, T. I. SURATWALA, M. D. FEIT, P. E. MILLER and R. STEELE, "The Effect of HF/NH₄F Etching on the Morphology of Surface Fractures on Fused Silica," *Journal of Non-Crystalline Solids,* **355,** 797 (2009).

121. G. A. C. M. SPIERINGS, "Wet Chemical Etching of Silicate Glasses in Hydrofluoric Acid Based Solutions," *Journal of Materials Science*, **28**, 23, 6261–6273 (1993).

122. T. SURATWALA, P. E. MILLER, M. FEIT, and J. MENAPACE, "Scratch Forensics," *Optics and Photonics News*, **12** (September 2008).

123. J. A. MENAPACE, P. J. DAVIS, W. A. STEELE, M. R. HACHKOWSKI, A. NELSON, and K. XIN, "MRF Applications: On the Road to Making Large-Aperture Ultraviolet Laser Resistant Continuous Phase Plates For High-Power Lasers," presented at Laser Induced Damage in Optical Materials, Boulder, CO, September 25, 2006, *SPIE Proc*., **6403**, 64030N (2006).

124. B. W. WOODS, I. M. THOMAS, M. A. HENESIAN, S. N. DIXIT, and H. T. POWELL, "Large-Aperture (80-cm-diameter) Phase Plates for Beam Smoothing on Nova," G. Dube, ed., *Proc. SPIE*, **1410**, Solid State Lasers II, 47–54 (1991).

125. S. N. DIXIT, I. M. THOMAS, B. W WOODS, A. J. MORGAN, M. A. HENESIAN, P. J. WEGNER, and H. T. POWELL, "Random Phase Plates for Beam Smoothing on the Nova Laser," *Applied Optics*, **32**, 2543–2554 (1993).

126. I. M. THOMAS, S. N. DIXIT, and M. C. RUSHFORD, "Kinoform Phase Plates for Focal Plane Irradiance Profile Control," *Optics Letters*, **19**, 417–419 (1994).

127. I. M. THOMAS, S. N. DIXIT, and M. C. RUSHFORD, "Preparation of Random Phase Plates for Laser Beam Smoothing," presented at Laser Induced Damage in Optical Materials: 1994, Boulder, CO, October 24, 1994, H. E. Bennett A. H. Guenther, M. R. Kozlowski, B. E. Newman and M. J. Soileau, eds., Proc. *SPIE*, **2428**, 264–270 (1994).

128. Y. LIN AND T. J. KESSLER, "Distributed Phase Plates for Super-Gaussian Focal Plane Irradiance Profiles," Laboratory for Laser Energetics (LLE), **63**, 126–129 (1995).

129. J. A. MAROZAS, "A High-Pass Phase Plate Design for OMEGA and the NIF," *LLE Review Quarterly Report*, **89**, 11–24 (2001).

130. J. NEAUPORT, X. RIBEYRE, J. DAURIOS, D. VALLA, M. LAVERGNE, V. BEAU, and L.VIDEAU, "Design and Optical Characterization of a Large Continuous Phase Plate for Laser Integration Line and Laser Megajoule Facilities," *Applied Optics*, **42**, 13, 2377–2383 (May 1, 2003).

131. D. C. HARRIS, "History of Magnetorheological Finishing," *Proc. SPIE*, **8016**, 1–22 (2011).

132. J. A. MENAPACE, P. J. DAVIS, S. DIXIT, J. H. CAMPBELL, D. GOLINI, M. R. HACHKOWSKI, and A. NELSON, "Imprinting Continuously Varying Topographical Structure onto Large-Aperture Optical Surfaces Using Magnetorheological Finishing," *Proc. Euspen*, **II**, 181–184 (2007).

133. T. G. PARHAM, T. J. MCCARVILLE, and M. A. JOHNSON, "Focal Length Measurements for the National Ignition Facility Large Lenses," *Optical Fabrication and Testing*, **OFT2002**, OWD8 (2002).

134. I. M. THOMAS, "Method for the Preparation of Porous Silica Antireflection Coatings Varying in Refractive Index from 1.22 to 1.44," *Appl. Opt.*, **31**, 28, 6145–6149 (1992).

135. F. L. RAVIZZA, M. C. NOSTRAND. L. M. KEGELMEYER, R.A. HAWLEY, AND M. A. JOHNSON, "Process for rapid detection of fratricidal defects on optics using Linescan Phase Differential Imaging," Laser-Induced Damage in Optical Materials: 2009 *Proc. SPIE*, **7504**, 75041B1-11 (2009).

136. S. DIXIT, J. BRITTEN, R. HYDE, C. HOAGLAN, M. RUSHFORD, L. SUMMERS, and J. TOEPPEN, "Fabrication and Applications of Large Aperture Diffractive Optics," *Proc. SPIE*, **4440**, 101–108 (2001).

137. J. YU, J. A. BRITTEN, L. SUMMERS, S. DIXIT, C. HOAGLAN, M. D. AASEN, R. P. HACKEL, and R. R. PRASAD, "Fabrication of Beam Sampling Gratings for the National Ignition Facility (NIF)," presented at Conference on Lasers and Electro-Optics (CLEO), A. A. Sawchuk (ed.), Baltimore, MD, USA, 1–6 June 2003.

138. I. M. THOMAS, A. K. BURNHAM, J. R. ERTEL, and S. C. FRIEDERS, "Method for Reducing the Effect of Environmental Contamination of Sol-gel Optical Coatings," *Proc. SPIE*, **3492**, Third International Conference on Solid State Lasers for Application to Inertial Confinement Fusion, 220 (July 23, 1999).

139. N. P. ZAITSEVA, I. L. SMOL'SKII, and L. N. RASHKOVICH, "Study of Rapid Growth of KDP Crystals by Temperature Lowering," *Sov. Phys. Crystallogr.*, **36**, 113–115 (1991).

140. N. P. ZAITSEVA, J. J. DE YOREO, M. R. DEHAVEN, R. L. VITAL, K. E. MONTGOMERY, M. RICHARDSON, J. L. ATHERTON, "Rapid Growth of Large Scale (40–55 cm) KDP Crystals," *J. Crystal Growth*, **180,** 255–262 (1997).

141. N. ZAITSEVA, J. ATHERTON, R. ROZSA, L. CARMAN, I. SMOLSKY, M. RUNKEL, R. RYON, L. JAMES, "Design and Benefits of Continuous Filtration in Rapid Growth of Large KDP and DKDP Crystals," *J. Crystal Growth*, **197**, 911–920 (1999).

142. N. ZAITSEVA AND L. CARMAN, "Rapid Growth of KDP-Type Crystals," *Prog. Cryst. Growth Charact. Mater.*, **43**, 1–118 (2001).

143. R. HAWLEY-FEDDER, H. ROBEY, T. BIESIADA, M. DEHAVEN, R. FLOYD, A. BURNHAM, "Rapid Growth of Very Large KDP and KD*P Crystals in Support of the National Ignition Facility," *Proc. SPIE*, **4102**, 152–161 (2000).

144. J. DEYOREO, T. LAND, L. RASHKOVICH, T. ONISCHERIKO, J. LEE, O. MONOVSKII, N. ZAITSEVA, "The Effect of Dislocation Cores on Growth Hillock Vicinality and Normal Growth Rates of KDP {101} Surfaces," *J. Crystal Growth*, **182**, 442–460 (1997).

145. H. ROBEY AND S. POTAPENKO, "Ex-Situ Microscopic Observation of the Lateral Instability of Macrosteps on the Surfaces of Rapidly Grown KH_2PO_4 Crystals," *J. Crystal Growth*, **213**, 355–367 (2000).

146. T. THOMAS, T. LAND, W. CASEY, and J. DEYOREO, "Emergence of Supersteps on KH_2PO_4 Crystal Surfaces," *Physical Review Letters*, **92**, (21), 216103 (2004).

147. I. SMOLSKI, J. DEYOREO, N. ZAITSEVA, J.D. LEE, T. LAND, and E.B.RUDNEVA, "Oriented Liquid Inclusions in KDP Crystals," *Journal of Crystal Growth*, **169**, 4, 741–746 (1996).

148. T. A. LAND and R. A. HAWLEY-FEDDER, "Advanced Crystal Growth Technology," UCRL-210700 (March 21, 2005).

149. P. Miller, "Some Equilibria Aspects of KDP Growth Solutions," NIF 0101124, LLNL (May 20, 2003).

150. T. LAND, R. DYLLA-SPEARS, and C. THORSNESS, "Virtual Crystallizer," UCRL-TR-224527 (September 19, 2006).

151. T. LAND, T. MARTIN, S. POTAPENKO, G. PALMORE, and J. DEYOREO, "Recovery of Surfaces from Impurity Poisoning During Crystal Growth," *Nature*, **399**, 441–445 (1999).

152. M. MONTICELLI and P. EHRMANN, "Record-Sized Rapid Growth KDP Boules and Efforts to Maximize Doubler Yield," NIF 111868, LLNL (January 14, 2005).

153. T. THOMAS, T. LAND, M. JOHNSON, and W. H. CASEY, "Experiments to Identify the Molecular Properties of Step-Pinning Adsorbates on KDP," *Geochimica ET Cosmochimica Acta*, **68**, (11) A168 (2004).

154. T. THOMAS, T. LAND, J. DEYOREO, and W. H. CASEY, "In Situ Atomic Force Microscopy Investigation of the {100} Face of KH_2PO_4 in the Presence of Fe(III), Al(III), and Cr(III)," *Langmuir*, **20**, (18) 7643–7652 (2004).

155. T. LAND, J. DEYOREO, T. MARTIN, and G. PALMORE, "A Comparison of Growth Hillock Structure and Step Dynamics on KDP {100} and {101} Surfaces Using Force Microscopy," *Crystallography Reports*, **44**, (4) 655–666 (1999).

156. N. BOOTH, T. LAND, P. EHRMANN, and P. VEKILOV, "The Aspect Ratio of Potassium Di-Deuterium Phosphate (DKDP) Crystals," *Crystal Growth & Design*, **5**, (1) 105–110 (2005).

157. T. SURATWALA, C. THORSNESS, and R. STEELE, "Thermal Fracture in DKDP Crystals," NIF0082445, LLNL (May 28, 2002).

158. T. SURATWALA, C. THORSNESS, T. LAND, M. EVANS, K. FOGLE, J. KIMMONS, K. KISHIYAMA, and R. STEELE, "Summary of DKDP Boule Fracture Tests," NIF0091695, LLNL (November 15, 2002).

159. MIKE RUNKEL, STEPHEN MARICLE, RICH TORRES, JERRY AUERBACH, RANDY FLOYD, RUTH HAWLEY-FEDDER and ALAN K. BURNHAM, "The Effect of Thermal Annealing and Second Harmonic Generation on Bulk Damage Performance of Rapid-Growth KDP Type I Doublers at 1064 nm," UCRL-JC-139619, presented at Laser Induced Damage in Optical Materials, Boulder, CO, October 16, 2000, *Proc. SPIE*, **4347**, 389–399 (2000).

160. MIKE RUNKEL, KURT NEEB, MIKE STAGGS, JEROME AUERBACH, and ALAN BURNHAM, "The Results of Raster Scan Laser Conditioning Studies on DKDP Triplers Using Nd:YAG and Excimer Lasers," UCRL-JC-144299, presented at Laser Induced Damage in Optical Materials, Boulder, CO, October 1, 2001, *Proc. SPIE*, **4679**, 368–383 (2001).

161. MIKE RUNKEL, JUSTIN BRUERE, WALLY SELL, TIM WEILAND, DAVE MILAM, DOUG HAHN AND MIKE NOSTRAND, "Effects of Pulse Duration on Bulk Laser Damage in 351-nm Raster Scanned DKDP," UCRL-JC-148593, presented at Laser Induced Damage in Optical Materials, *Proc. SPIE*, **4932**, 405–414 (2002).

162. L. J. ATHERTON, F. RAINER, J. J. DE YOREO, I. M. THOMAS, N. ZAITSEVA, and F. DE MARCO, "Thermal and Laser Conditioning of Production- and Rapid-Growth KDP

and KD*P Crystals," Laser-Induced Damage in Optical Materials: 1993, *Proc. SPIE*, **2114**, 36–44 (1993).

163. B. WOODS, M. RUNKEL, M. YAN, J. J. DEYOREO, and M. KOZLOWSKI, "Optical Scatter as a Diagnostic Tool for Studying Bulk Defects Which Cause Laser Damage in Conventional and Rapid Growth KDP and DKDP," in Optical Scattering in Optics, Semiconductors, and Computer Disk Industries, *Proc. SPIE*, **2541**, J.C. Stover, ed. SPIE, Bellingham, WA, 1995.

164. M. RUNKEL, M. YAN, J. DE YOREO, and N. ZAITSEVA, "The Effect of Impurities and Stress on the Damage Distributions of Rapidly Grown KDP Crystals," Laser-induced Damage in Optical Materials: 1997, *Proc. SPIE*, **3244**, 211–222 (1997).

165. MIKE RUNKEL and ALAN K. BURNHAM, "Differences in Bulk Damage Probability Distributions Between Tripler and Z-Cuts of KDP and DKDP at 355 nm," UCRL-JC-139622, presented at Laser Induced Damage in Optical Materials, Boulder, CO, October 16, 2000, *Proc. SPIE*, **4347**, 408–419 (2000).

166. A. K. BURNHAM, M. RUNKEL, R. A. HAWLEY-FEDDER, M. L. CARMAN, R. A. TORRES, and P. K. WHITMAN, "Low-Temperature Growth of DKDP for Improving Laser-Induced Damage Resistance at 350 nm," UCRL-JC-139648, presented at Laser Induced Damage in Optical Materials, Boulder, CO, October 16, 2000, *Proc. SPIE*, **4347**, 373–388 (2000).

167. MIKE RUNKEL and MIKE NOSTRAND, "An Overview of Laser Raster Scanning for ICF-Class Laser Optics," UCRL-JC-148481, presented at Laser Induced Damage in Optical Materials, Boulder, CO, September 16, 2002, *Proc. SPIE*, **4932**, 136–146 (2002).

168. MIKE STAGGS, MING YAN and MIKE RUNKEL, "Laser Raster Conditioning of KDP and DKDP Crystals Using XeCl and Nd:YAG Lasers," UCRL-JC-140764, presented at Laser Induced Damage in Optical Materials, Boulder, CO, October 16, 2000, *Proc. SPIE*, **4347**, 400–407 (2000).

169. MIKE RUNKEL, ALAN BURNHAM, DAVID MILAM, WALTER SELL, MIKE FEIT and ALEXANDER RUBENCHIK, "The Results of Pulse-Scaling Experiments on Rapid-Growth DKDP Triplers Using the Optical Sciences Laser at 351 nm," UCRL-JC-139623, presented at Laser Induced Damage in Optical Materials, Boulder, CO, October 16, 2000, *Proc. SPIE*, **4347**, 359 (2000).

170. J. J. ADAMS, J. A. JARBOE, C. W. CARR, M. D. FEIT, R. P. HACKEL, J. M. HALPIN, J. HONIG, L. A. LANE, R. L. LUTHI, J. E. PETERSON, D. L. RAVIZZA, F. RAVIZZA, A. M. RUBENCHIK, W. D. SELL, J. L. VICKERS, T. L. WEILAND, T. J. WENNBERG, D. A. WILLARD, and M. F. YEOMAN, "Results of Sub-Nanosecond Laser Conditioning of KD2PO4 Crystals," *Proc. SPIE*, **6403**, 64031M-1 (2007).

171. J. HONIG and J. HALPIN, "Diode-Pumped 22-W Average-Power UV Laser With User-Selectable Pulse Width and > 50% Conversion Efficiency," UCRL-CONF-228881 (March 9, 2007), presented at CLEO/QELS Technical Conference, Baltimore, MD, May 6, 2007 through May 11, 2007.

172. Z. M. LIAO, M. SPAETH, K. MANES, and C. W. CARR, "Predicting Laser-Induced Bulk Damage and Conditioning for Deuterated Potassium Di-hydrogen Phosphate Crystals using Absorption Distribution Model," *Optics Letter*, **35**, 2538-2540, (2010)

173. Z. M. LIAO, R. ROUSSELL, J. J. ADAMS, M. NORTON, M. RUNKEL, W. T. FRENK, J. LUKEN, and C. W. CARR, "Influence of Growth Behavior on Laser-Induced Bulk

Damage in Deuterated Potassium Di-hydrogen Phosphate (DKDP) Crystals," *Proc. SPIE,* **8885**, 8888501-1 (2013)

174. Private Communication with Z. M. LIAO, author ADM model descriptions, March 2015

175. J. J. ADAMS, J. R. BRUERE, M. BOLOURCHI, C. W. CARR, M. D. FEIT, R. P. HACKEL, D. E. HAHN, J. A. JARBOE, L. A. LANE, R. L. LUTHI, J. N. MCELROY, A. M. RUBENCHIK, J. R. STANLEY, W. D. SELL, J. L. VICKERS, T. L. WEILAND, D. A. WILLARD, "Wavelength and pulselength dependence of laser conditioning and bulk damage in doubler-cut KH_2PO_4," *Proc. SPIE*, **5991**, 59911R (2005)

176. R. C. MONTESANTI, S. F. LOCKE, and S. L. THOMPSON, "Diamond Flycutting Machine for Producing Flat Surfaces on Half-Meter Scale Diamond-Turnable Optics," presented at Proced. ASPE 14th Annual Meeting, October 31–November 5, 1999, Monterey CA, **20**, 57–61 (1999).

177. P. GERAGHTY, "KDP Finishing Machine Flycutter Design‑Design Summary," NIF-0067247, LLNL (2001).

178. S. G. DEMOS, M. C. NOSTRAND, M. STAGGS, C. W. CAM, D. HAHN, M. R. KOZLOWSKI, L. SHEEHAN, C. BATTERSBY, and A. BUMHAM, "Investigation of Fluorescence Microscopy as a Tool for Noninvasive Detection and Imaging of Damage Precursors at 351-nm," presented at Laser-Induced Damage in Optical Materials, Boulder, CO, October 1, 2001, *Proc. SPIE*, **4679**, 347–358 (2002).

179. M. C. NOSTRAND, S. THOMPSON, W. SIEKHAUS, M. FLUSS, D. HAHN, P. WHITMAN, and A. BURNHAM, "Identification and Elimination of Fluorescent Surface-Damage Precursors on DKDP Optics," UCRL-JC-148498, presented at Boulder Damage

Symposium XXXIV: Annual Symposium on Optical Materials for High Power Lasers, Boulder, CO, September 16–18, 2002.

180. W. STOBER, A. FINK, and E. BOHN, "Controlled Growth of Mono-Disperse Silica Spheres in the Micron Size Range," *J. Colloid Interface Sci.*, **26**, 62 (1968).

181. H. FLOCH and P. BELLEVILLE, United States Patent No. 5,698,266, "Process for the Production of Thin Coatings having Optical and Abrasion Resistance Properties," Dec. 16, 1997.

182. E. K. WHEELER, P. K. WHITMAN, T. A. LAND, J. DEYOREO, C. B. THORSENSS, J. H. MCWHIRTER, M. L. CARMAN, and E. L. MILLER, "Investigation of Etch Pits on KDP Crystals with Porous Sol-Gel Coatings," UCRL-JC-142455, LLNL, *Applied Physics A*, **74**, 6, 813–823 (June 2002).

183. E. WHEELER and P. WHITMAN, "KDP Scatter Measurement Development," NIF-0023585, LLNL (1999).

184. I. M. THOMAS, "Two Layer Broadband Antireflective Coating Prepared from a Methyl Silicone and Porous Silica," UCRL-JC-126335, LLNL (1997).

185. E. MILLER, T. L. LAND, and P. WHITMAN, "Effects of Thermal Annealing on the Chemical Composition of Dihydrogen Phosphate (KDP) Surfaces," UCRL-142259, LLNL (2001).

186. P.K. WHITMAN and E. L. MILLER, "Etch Pit Formation Experiment 16: Verification of Etch Pit and Coating Performance for Thermal-Annealed KDP Doublers and Switch Crystals and for Triplers (Final Report)," NIF-0079437, LLNL (2002).

187. L. A. B. PILKINGTON, "Review Lecture. The Float Glass Process," *Proc. R. Soc. Lond. A*, **314**, 1516, 1–25 (1969).

188. L.A. B. PILKINGTON and K. BICKERSTAFF, "Manufacture of Flat Glass," Patent 2,911,759, November 10, 1959.

189. Borofloat®—Inspiration Through Quality, n.d., para. 3, retrieved from http://www.us.schott.com/borofloat/english/production (current as of April 2, 2015).

190. I. M. THOMAS, A. K. BURNHAM, J. R ERTEL, and S. C FRIEDERS, "Method for Reducing the Effect of Environmental Contamination of Sol-Gel Optical Coatings," *Proc. SPIE*, 3492, 220–229 (1999).

191. M. L. SPAETH, K. R. MANES, M. BOWERS, P. CELLIERS, J-M. DI NICOLA, P. DI NICOLA, S. DIXIT, G. ERBERT, J. HEEBNER, D. KALANTAR, O. LANDEN, B. MACGOWAN, B. VANWONTERGHEM, P. WEGNER, C. WIDMAYER, and S. YANG, "National ignition facility Laser System Performance," this issue of *Fusion Science and Technology*.

FIGURES
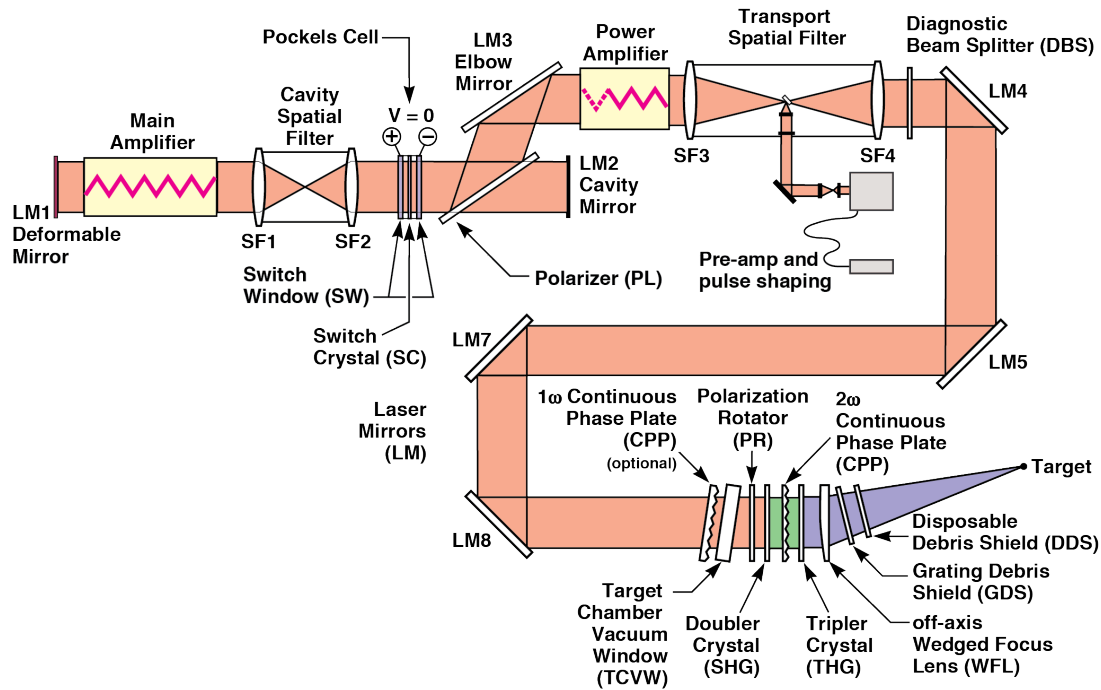
Fig. 1: Schematic representation of the optical layout of one of the 192 identical laser beamlines that comprise the NIF. For clarity, the LM6 mirrors are not shown since they are used only in 64 of the 192 beamlines.
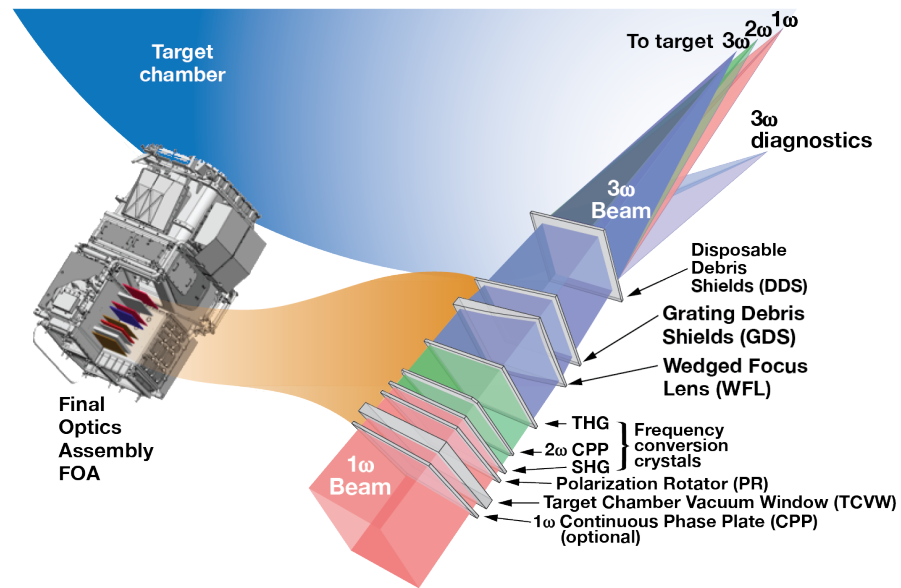
Fig. 2: A schematic diagram of (left) an FOA attached to the NIF target chamber and (right) one of the four IOMs with the final optical components.
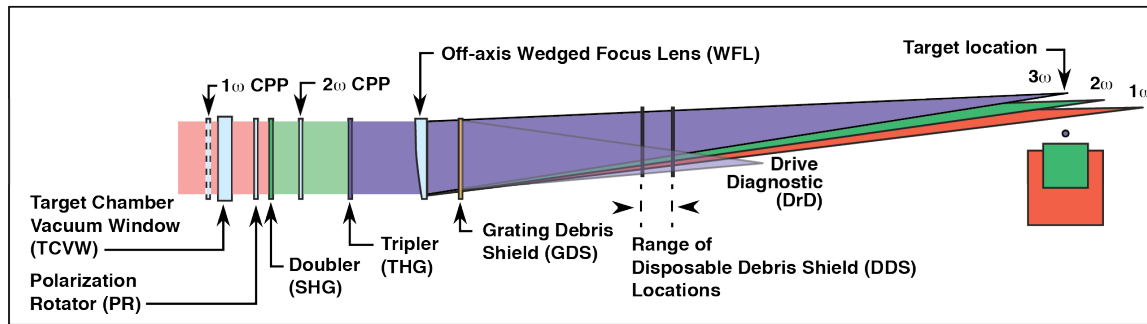
Fig. 3: Schematic of the components of the Final Optics Assembly. Note that the location of the focus for each of the wavelengths has been offset for clarity. They actually fall on a common line parallel to the axis of the light in the FOA.
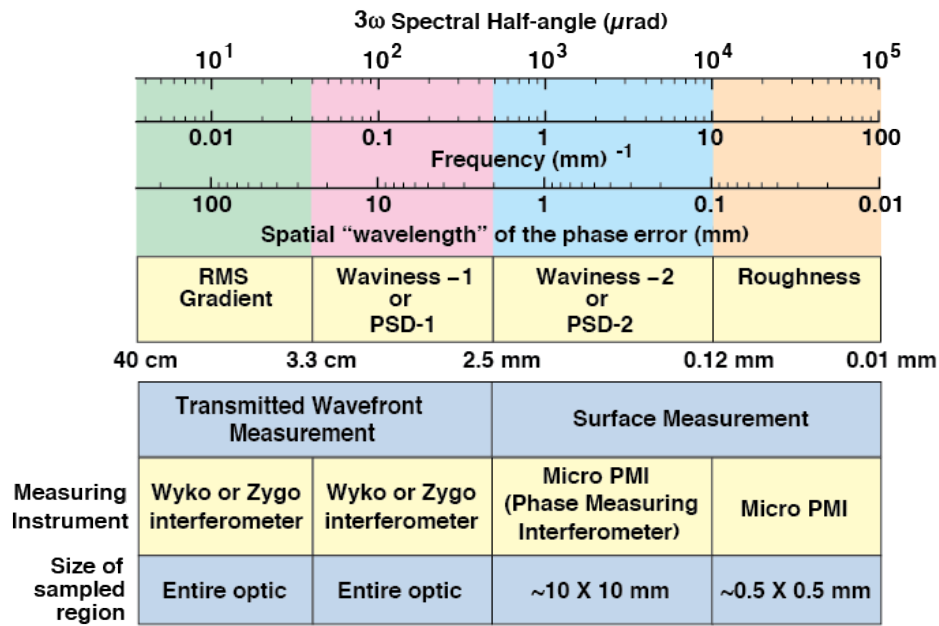
Fig. 4: The spatial frequency or spatial wavelength ranges used to specify the optical quality required of NIF optics. The different ranges are delineated from each other based on the diagnostic instruments used to measure features in each range.
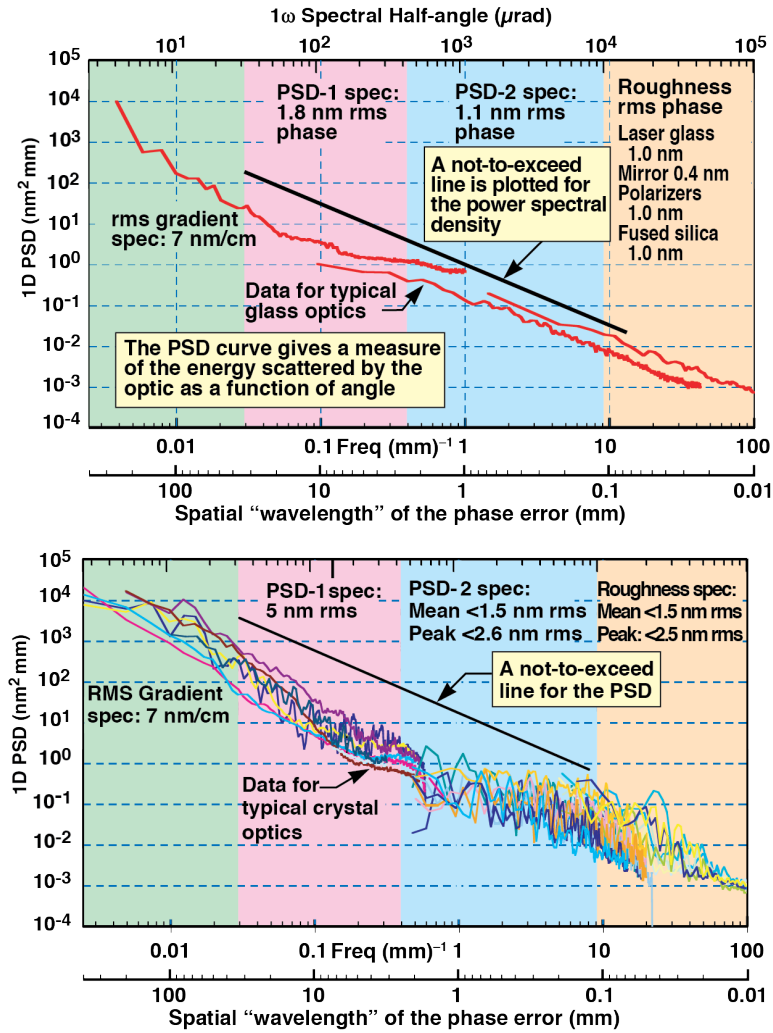
Fig. 5: The NIF specifications used for large glass optics (top) and crystal optics (bottom) expressed in terms of their 1-D PSD. There are two types of specifications for the PSD-1, PSD-2, and Roughness ranges, a specification for the rms value over a spatial area and a not-to-exceed value. Both are a function of spatial frequency. (Graphics from Ref. 26)
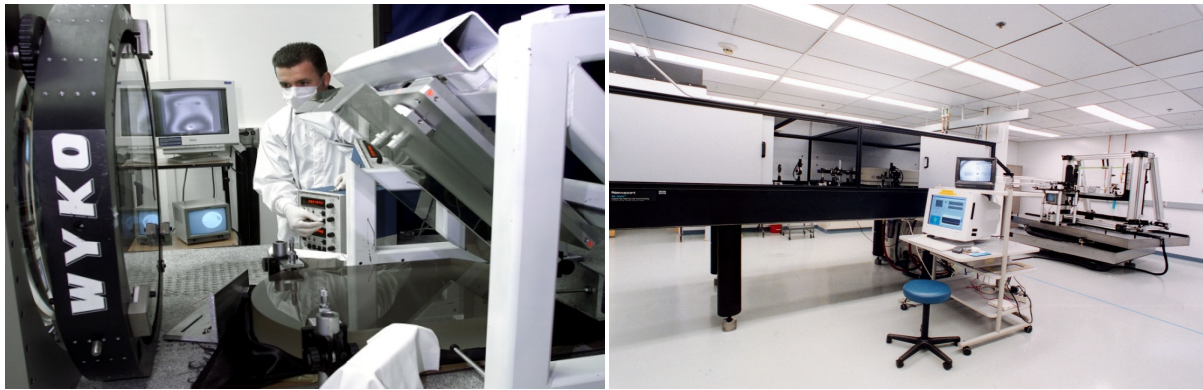
Fig. 6: The left photograph shows the Wyko 24-in. phase shifting interferometer located at LLNL. The right photograph shows a Large Area Conditioning system located at an optic supplier (University of Rochester, Laboratory for Laser Energetics).
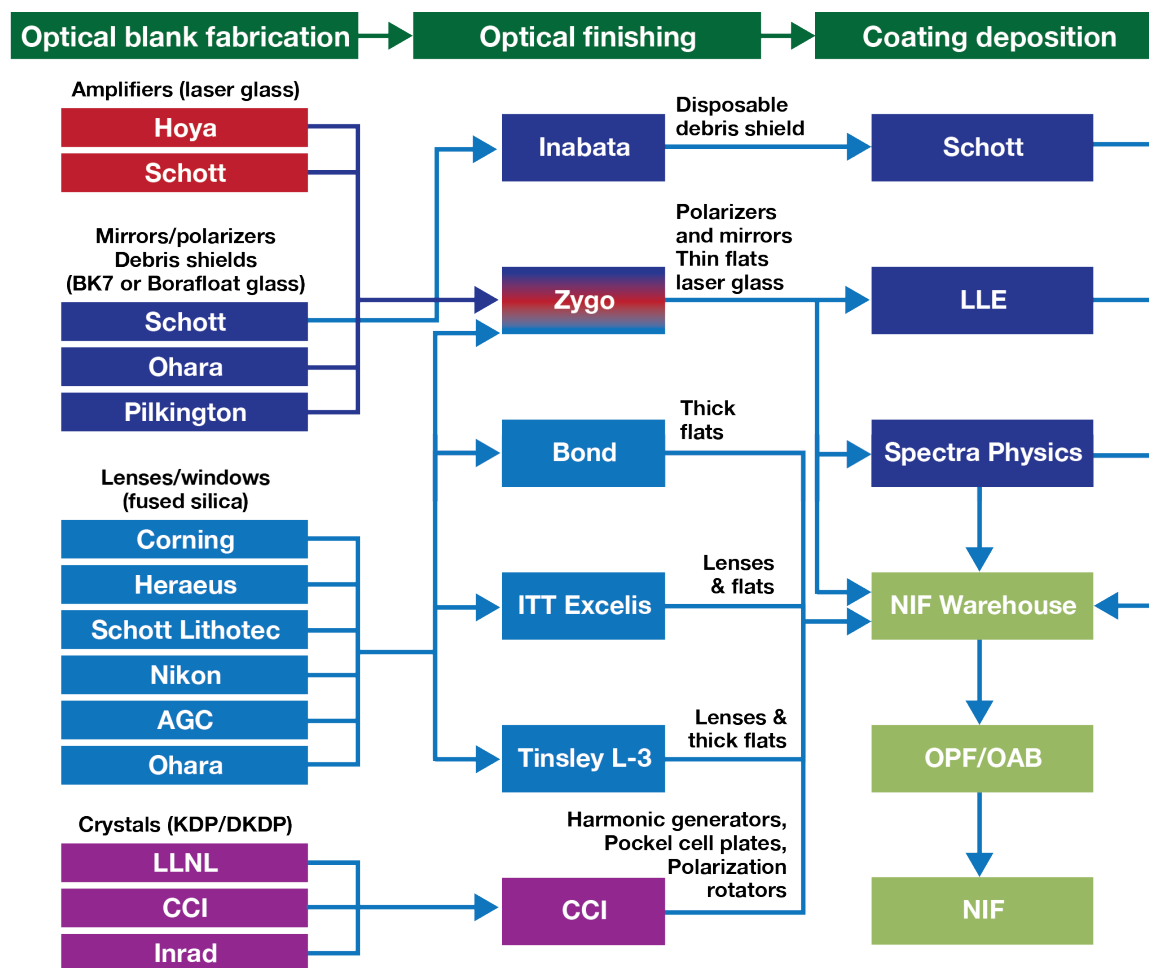
Fig. 7: Optics suppliers participating in delivery of the large optics for NIF. The following acronyms are used in this figure. Suppliers: AGC—Asahi Glass Co.; CCI—Cleveland Crystals, Inc.; ITT—International Telephone & Telegraph Excelis; LLE—University of Rochester, Laboratory for Laser Energetics. The Optics Processing Facility (OPF) and Optics Assembly Building (OAB) are located at LLNL.
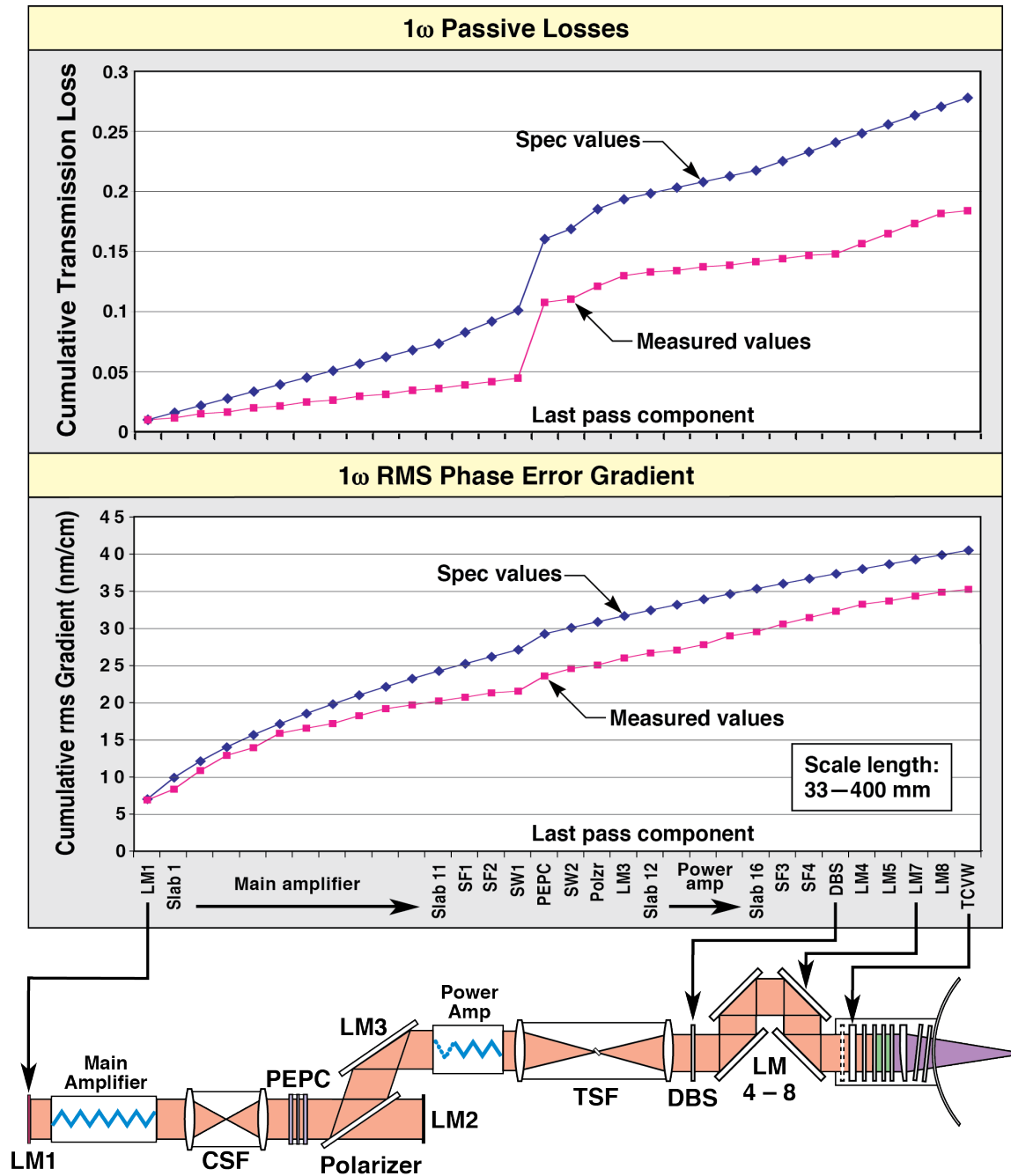
Fig. 8: In general, the majority of NIF optics are significantly better than specifications. This is illustrated here for two critical specifications: (top) the passive optical losses that impact the overall energy delivered, and (bottom) the rms gradient specification that impacts the far-field spot on target. The results show the cumulative contribution of these effects on the final pass

through the laser chain. Note that both the cumulative measured gradient and optical loss are significantly better (lower) than the specification.

Fig. 9: (left) Photograph of a finished amplifier slab (81 cm × 46 cm × 4 cm); note the blue-green edge cladding. (right) Photograph of an amplifier slab line replaceable unit being assembled at LLNL for installation into the NIF laser.
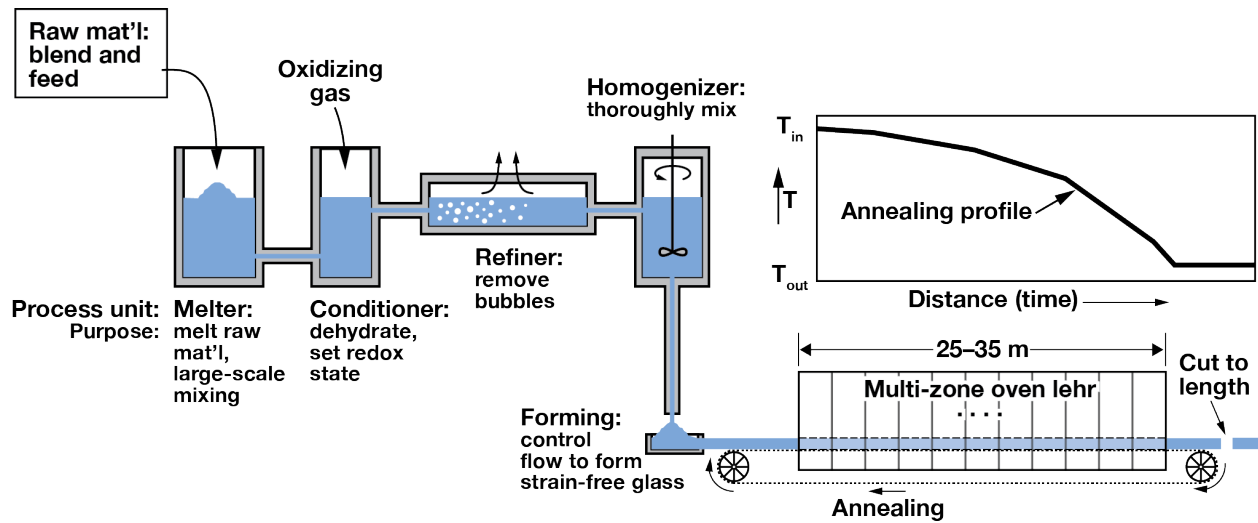
Fig. 10: Schematic representation of the continuous laser glass melting system used to manufacture laser glass by both Hoya and Schott.[36] A plot of the laser glass annealing profile, that is the change in temperature, T, as a function of distance (time) in the lehr, is shown in the top right corner of the figure. T_{in} and T_{out} refer to the input and output temperature of the laser glass in the lehr respectively.
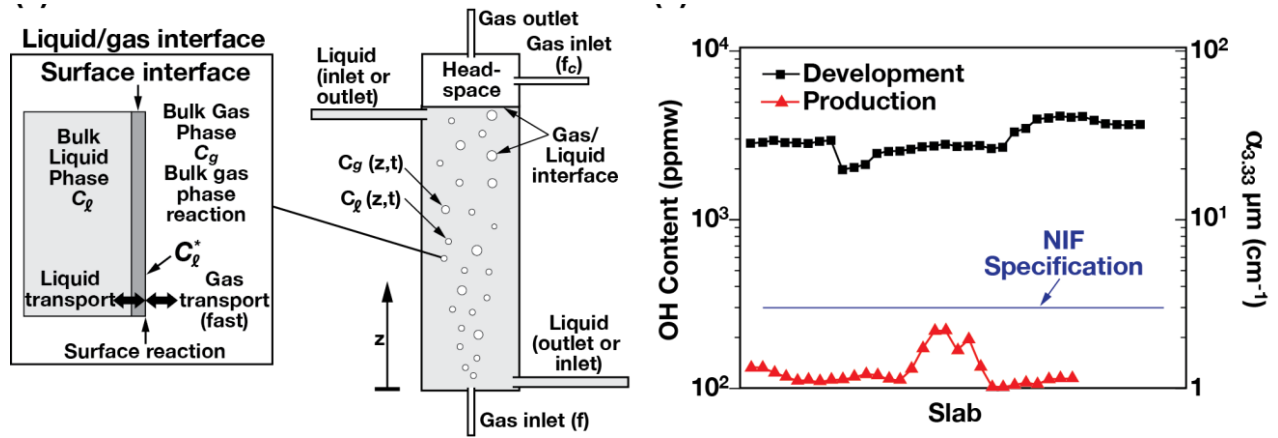
Fig. 11: (left) Physical representation of the time-dependent, one-dimensional dehydroxylation model for OH removal using gas bubbling through a phosphate glass melt. The model treats both inert (e.g. O_2) and reactive (e.g. Cl_2) gases.[46] The subscripts ℓ and g represent model parameters (species) in the liquid and gas phase respectively, C is the concentration of a particular species at time (t) and height (z) in the bubble column, and C^* is the gas/liquid interface concentration. (right) Graph of OH content in parts per million by weight and OH absorption coefficient (of the hydroxyl stretching band at 3.3 µm) for randomly selected laser glass slabs showing a nearly 50-fold reduction in this contaminant comparing an early development run and a production melt campaign.[51]

Fig. 12: (left) Photograph of laser glass leaving the lehr at Hoya and (right) an annealing oven at Schott.

Fig. 13: Photograph of an amplifier being (left) ground and (right) final polished at Zygo Corporation.
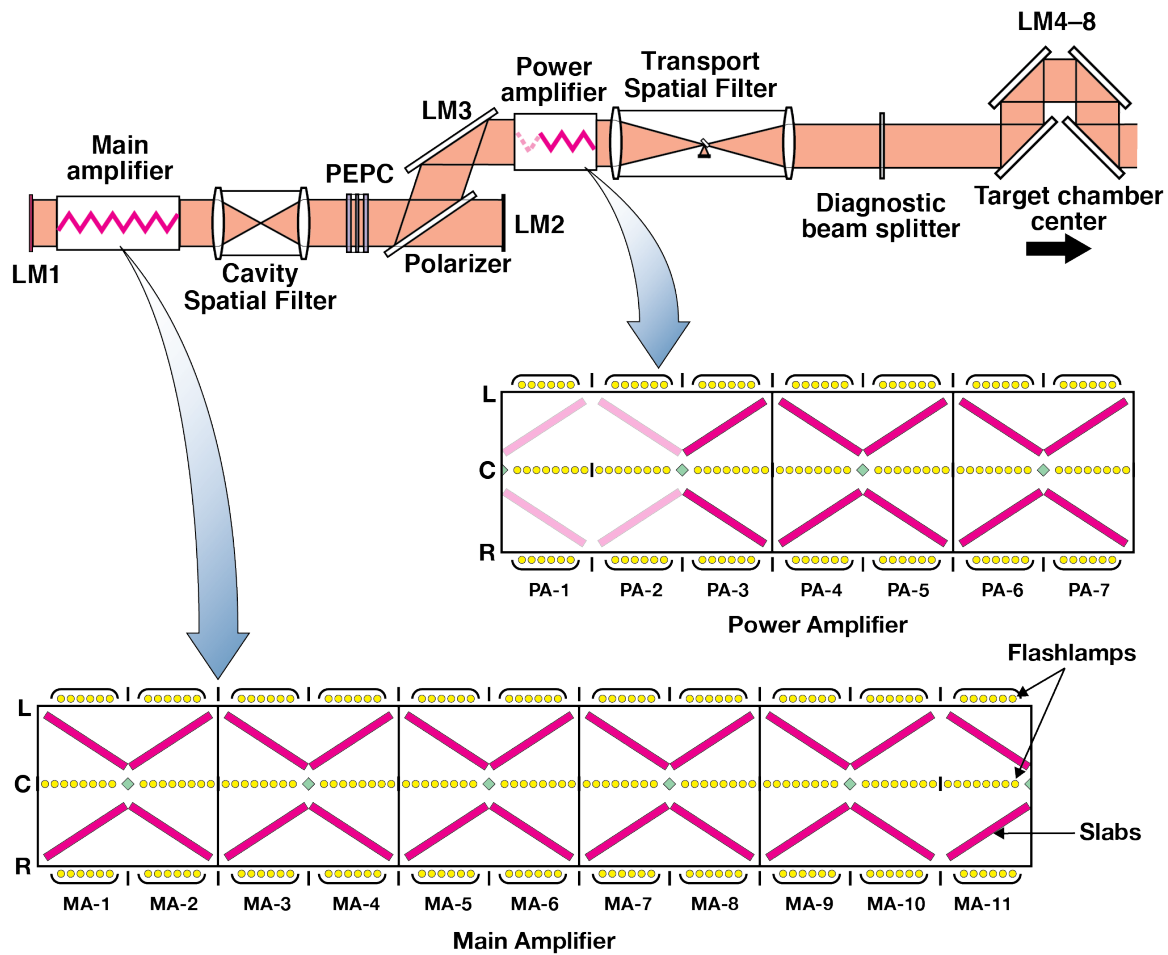
Fig. 14: The lower part of this graphic shows laser slabs in the large 1ω amplifiers as seen when looking down from the top. Note that in this particular view, there are no slabs in the PA-1 and PA-2 positions. In such a configuration the amplifier is in what is referred to as an 11-5 configuration. Adding slabs to locations PA-1 and PA-2 would result in an 11-7 configuration.[41]
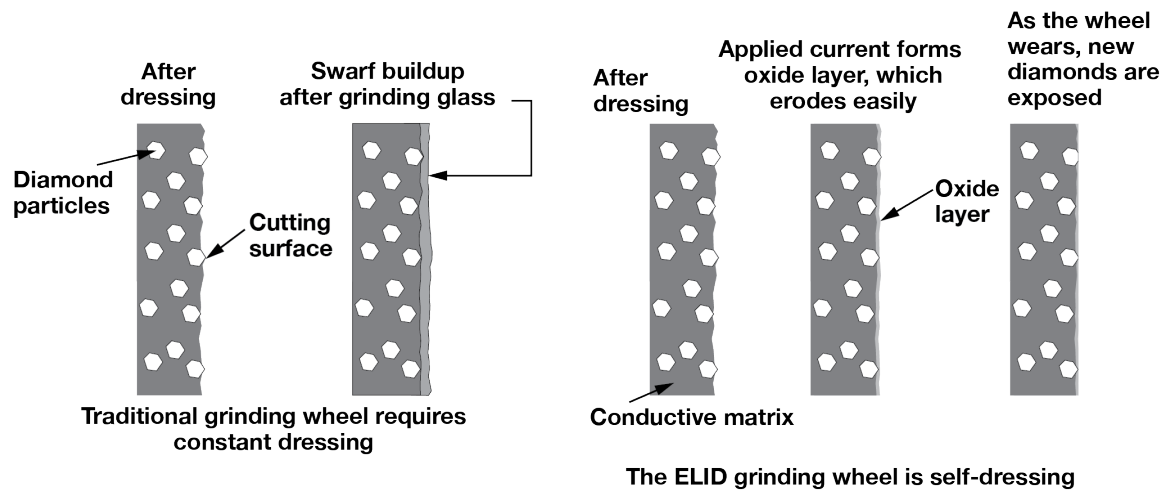
Fig. 15: A comparison of (left) traditional and (right) ELID grinding.
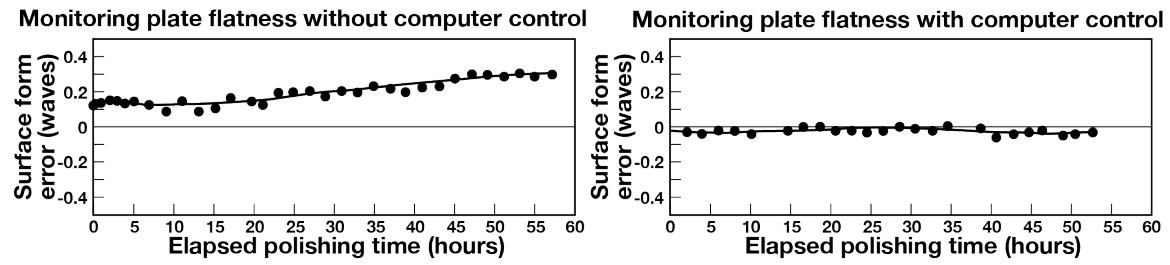
Fig. 16: Surface flatness shown for the 168-in. polishing lap (left) without and (right) with computer and temperature control as a function of time.
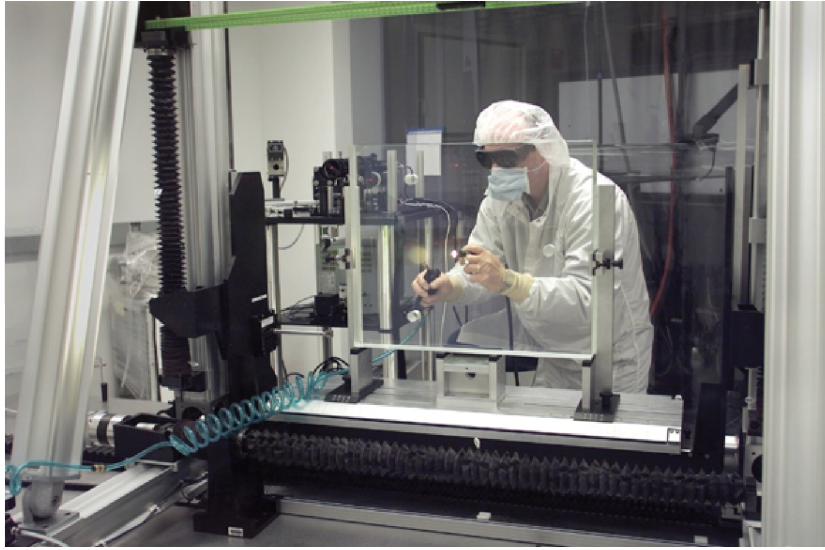
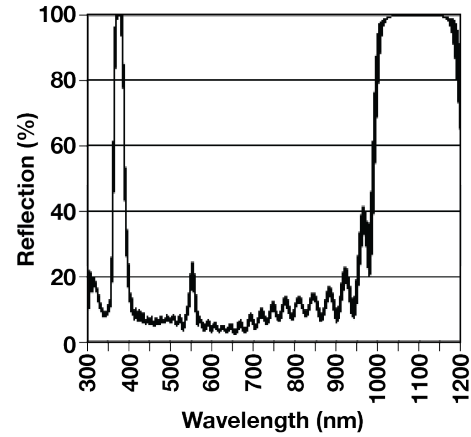Fig. 17: A photograph of a mirror as it is visually inspected for laser damage.

Fig. 18: (left) Laser photometer used for spectral characterization of the entire mirror surface at 1053, 527, and 351 nm. (right) Averaged spectral characteristics of 22 NIF LM-8 transport-mirror coating runs obtained using a broadband spectrometer at an incidence angle of 21.5 and 31.5 degrees, depending on their specific use location, and p polarization. The line width at each wavelength is equal to the standard deviation.
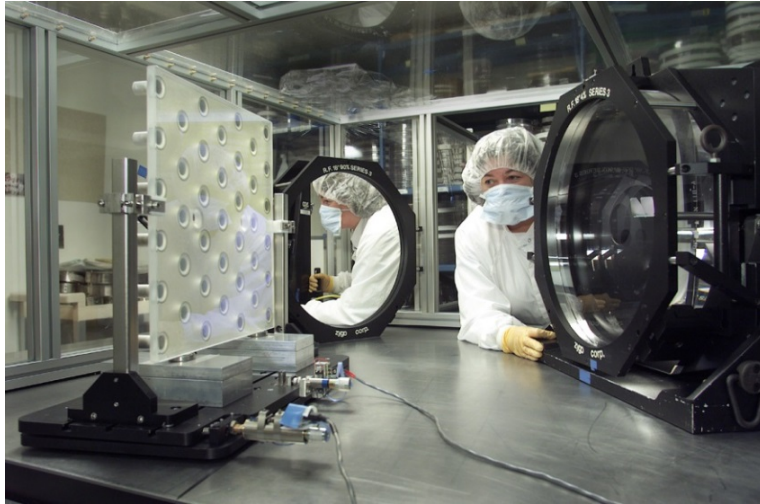
Fig. 19: An 18-in. phase measuring interferometer operating at 1064 nm is shown measuring the reflected wavefront of a deformable mirror phase plate after coating.

Fig. 20: The final two NIF transport mirrors (LM7 and LM8) are darkened by exposure to a cobalt-60 gamma radiation source to prevent laser damage to mounting hardware due to target backscatter (SBS and SRS). The left mirror has been darkened while the mirror on the right has not yet been exposed to radiation.
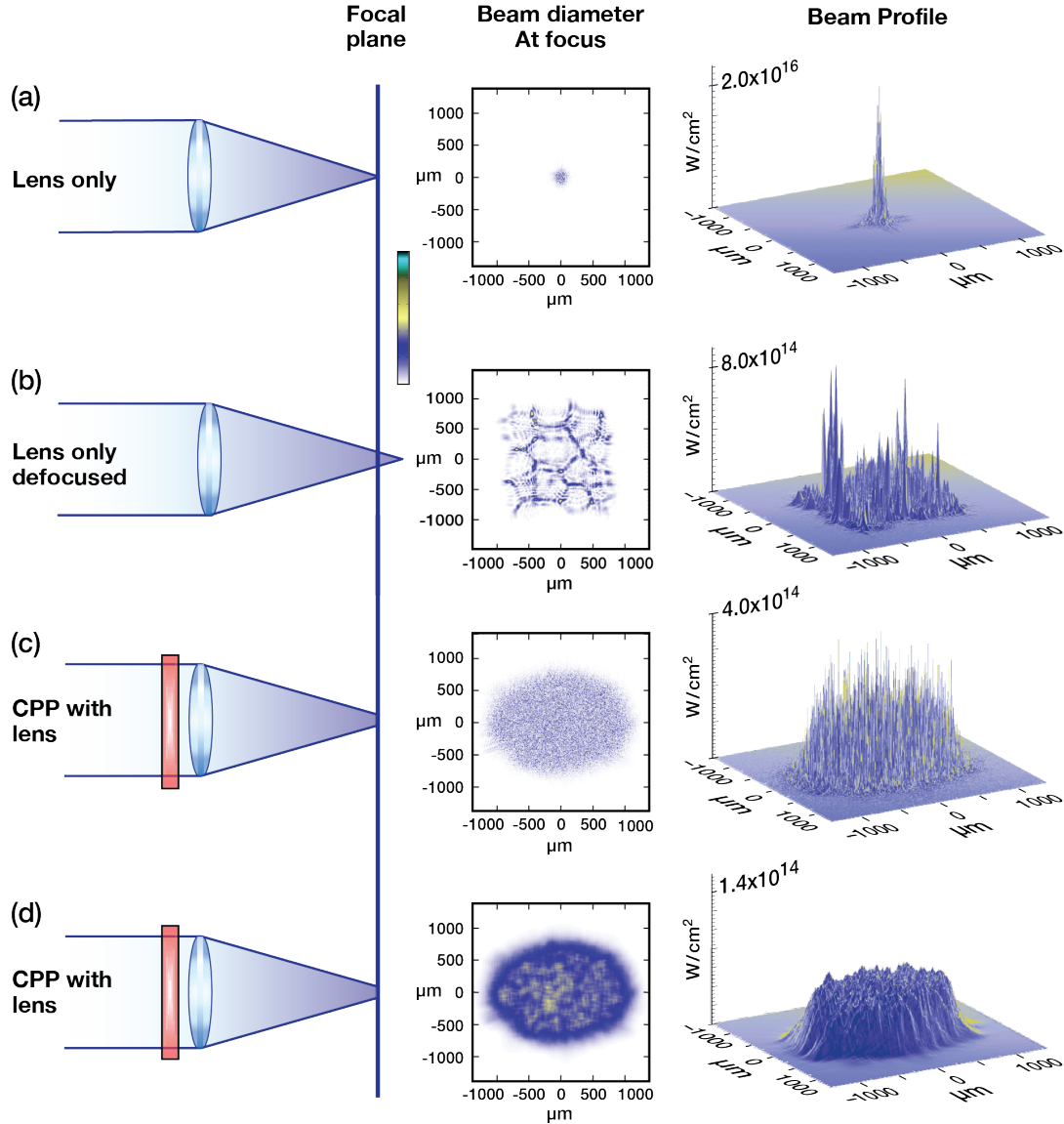
| Focal plane | Beam diameter At focus | Beam Profile |

(a)

Lens only

(b)

Lens only defocused

(c)

CPP with lens

(d)

CPP with lens

Fig. 21: Calculated spatial distributions of the intensity of a typical 1 TW NIF beam, at or near the location of best focus. (a) Calculated focal spot expected for a NIF beam without application of any beam conditioning. This calculation is in good agreement with the focal spot size measurements made for one of the NIF beams in the Precision Diagnostic System (PDS) as NIF was being prepared for full operation.[79] (b) Calculated out-of-focus spot of an unconditioned NIF beam, for a location 3 cm from the location of best focus. At this location, the beam is in the intermediate field, neither in the far field, at focus, or in the near field, as it leaves the output

optics of the laser. Similar out-of-focus images were collected for the Nova laser.[80] (c)

Calculated image of an instantaneous snapshot of a NIF beam at best focus with a CPP in the

FOA. Similar images were also measured for a NIF beam in PDS.[79] (d) Calculated image of (c),

with 92 μm of mathematical beam smoothing applied. Smoothed images such as this are used to

represent the result of smoothing techniques used on NIF, "smoothing-by-spectral dispersion"

(SSD) and the temporal response of the target plasma to the instantaneous profile of the incident
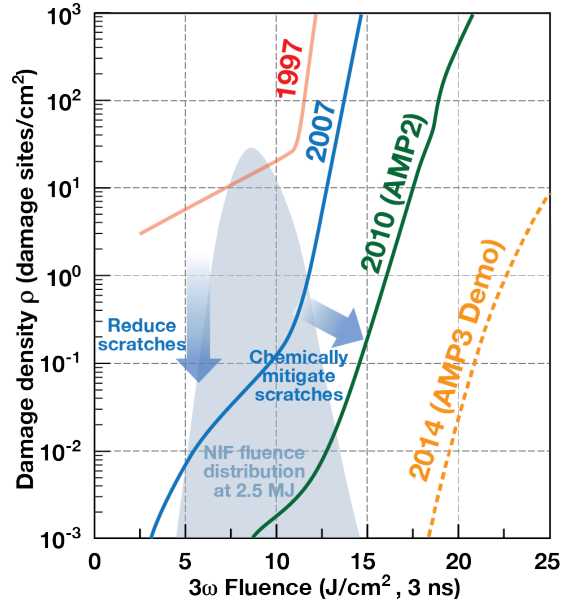
beam.[81]

Fig. 22: Laser damage density as a function of 3ω laser fluence. The different color lines describe the temporal evolution in the optical damage resistance attributable first to improved finishing (see text) and handling technologies (1997–2007), and secondly to the development of a chemically based whole optic mitigation process (2007–2012).[92, 93] The yellow dashed line represents the optical damage performance of sub-scale (50-mm) fused silica optic as reported in Ref. 94. The light-blue shaded area represents a relative fluence distribution typical of a 2.5-MJ, 3ω laser shot.
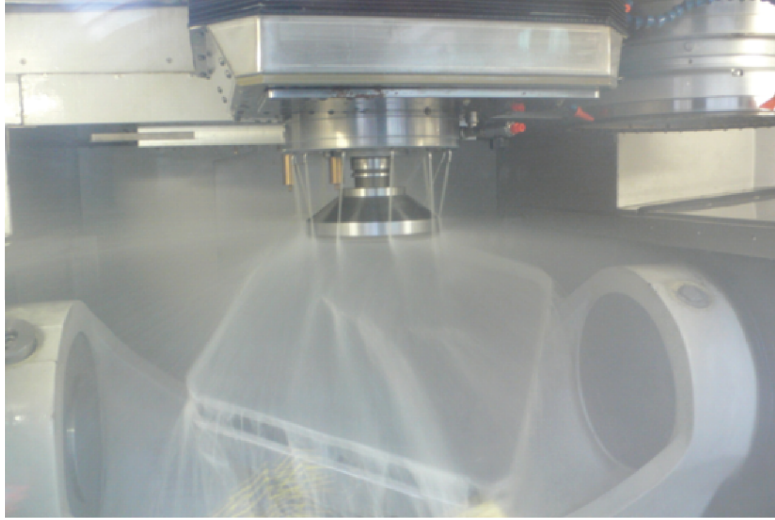
Fig. 23: A fixed-abrasive grinding operation being conducted on a fused silica substrate during production of an off-axis wedged focus lens using a multi-axis machine tool.
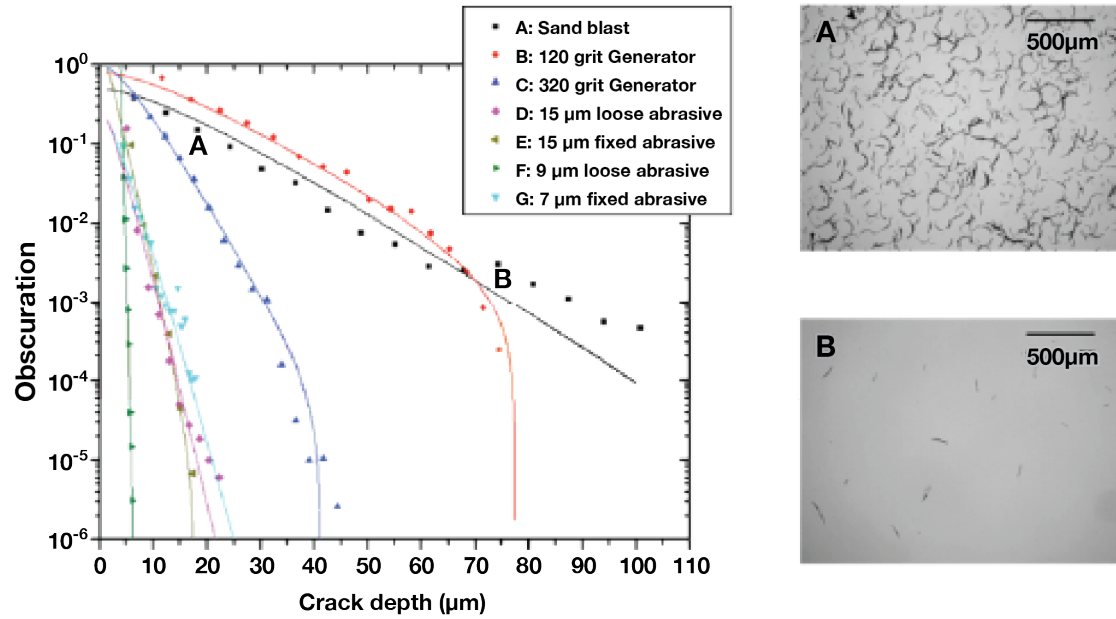
Fig. 24: Distribution of fracture (crack) depths resulting from sandblasting together with examples of fixed- and loose-abrasive grinding operations. The accompanying photomicrographs illustrate the remaining subsurface damage from the sandblasted sample at a depth of 20 μm below the surface (A) and 75 μm below the surface (B).
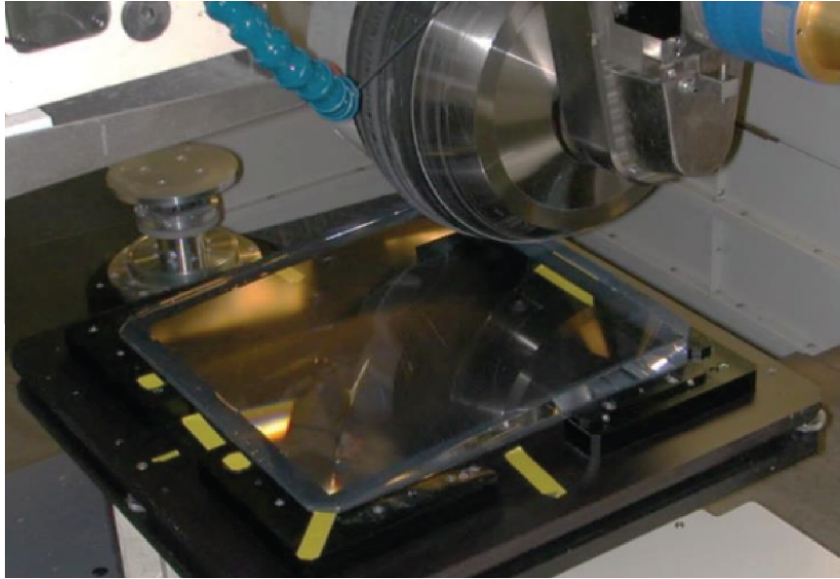
Fig. 25: Small-tool polishing being performed on the aspheric surface of a NIF off-axis WFL using a MRF tool.
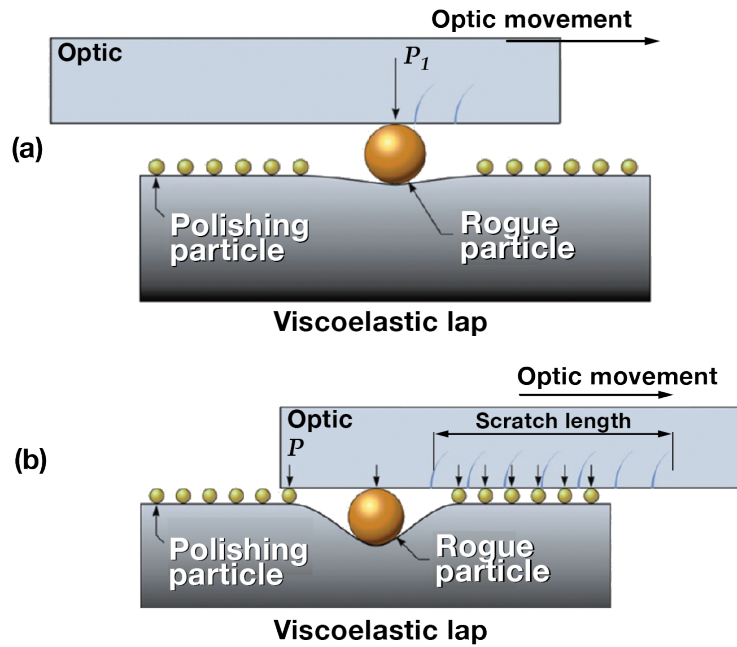
Fig. 26: Schematic illustration of the formation of a fracture (scratch) during polishing. As the optic traverses the polishing lap, particles experience a load that is proportional to their size. (a) The load (P_1) imposed by an anomalously large (rogue) particle may be sufficient to initiate a trailing indentation fracture. (b) The scratch will extend over a distance that is determined by the time that it takes for the rogue particle to settle into the viscoelastic lap to a depth required to distribute the total load over a sufficient number of particles such that the load imposed by any single particle (P) remains below the critical load required to initiate fracture.

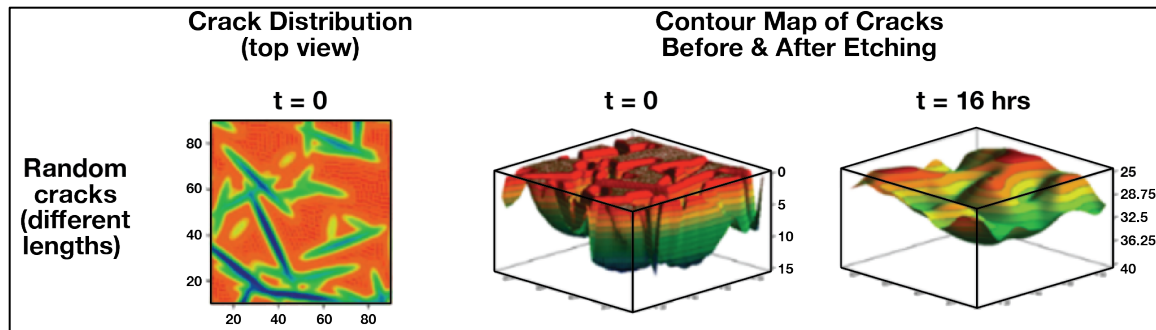Fig. 27: A 3-D, finite, difference etch-model simulation for a random distribution of closely spaced surface fractures prior to and following 16 hours of hydrofluoric acid etching, adapted from Ref. 120. When the density of fractures is sufficiently high, as would be observed on a ground surface, adjacent fractures coalesce with one another. This results in a reduced peak-to-valley roughness relative to the initial fracture depth.
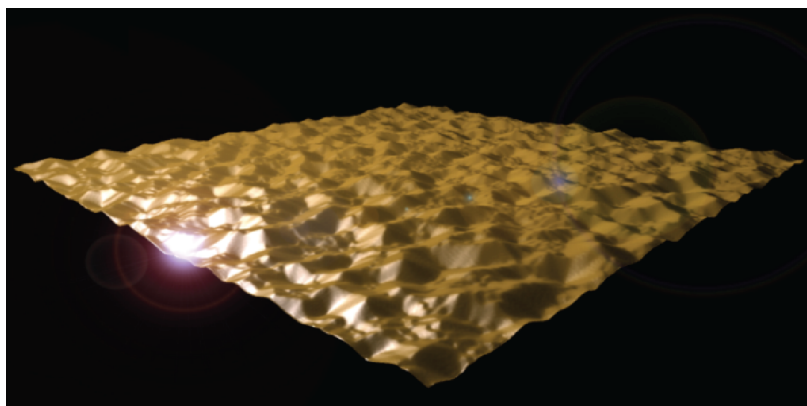
Fig. 28: A computer-designed continuously varying topographical CPP pattern with an 8.6-μm peak-to-valley imprinted onto a 430 mm × 430 mm × 10 mm fused silica substrate.

Fig. 29: Magneto-rheological finishing polishes an optic by creating a sub-aperture polishing tool using a continuously recycled magnetic fluid and an electromagnet. Material is removed in the area where the optic is immersed into the fluid ribbon. Surface polishing is accomplished by rastering or rotating the optic through the fluid.

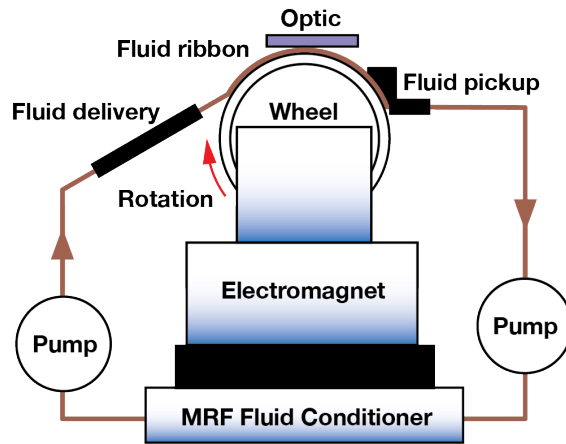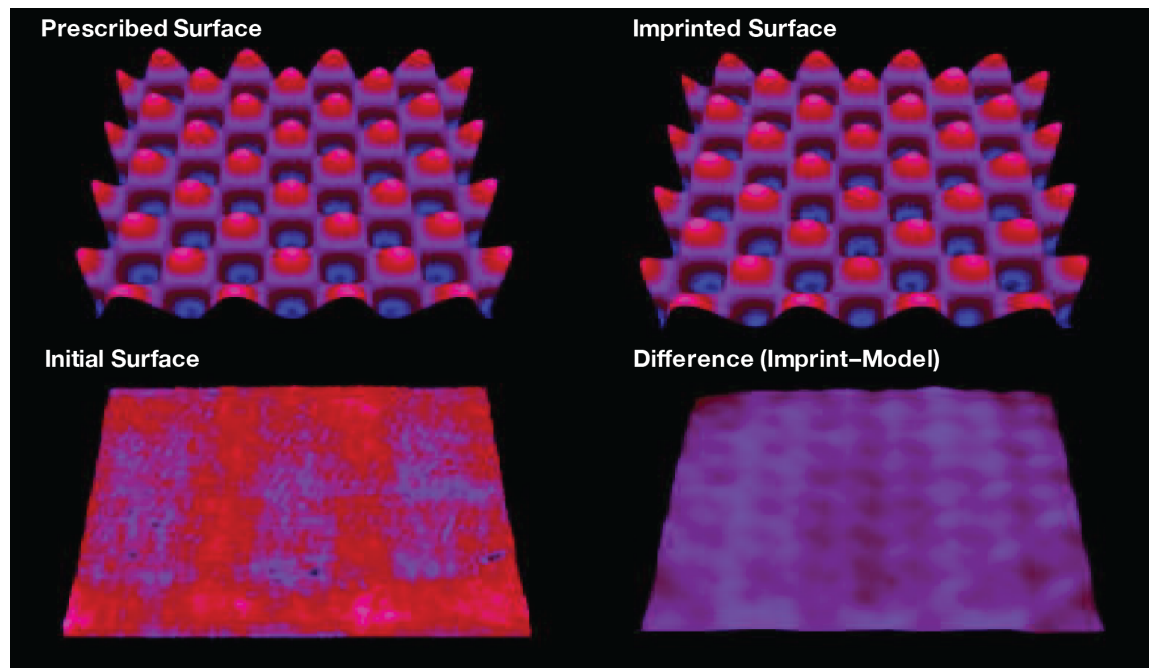Fig. 30: Comparison of an imprinted sinusoidal profile with the original prescribed profile using a 2.8-mm MRF removal function. This comparison includes the prescribed surface (top-left), the surface topography as imprinted (top right), the optical surface before MRF imprinting (bottom left), and the difference between the prescribed and imprinted surfaces (bottom-right). The rms of the difference between the prescribed and imprinted topographies is 12 nm, illustrating the fidelity of the imprinting process.

Fig. 31: Large-aperture Q22-750P2 MRF system used to make NIF CPPs. Shown in the inset are the two wheels, one large (left) and one small (right) used to imprint topographical features down to spatial periods of 1 mm. This machine can polish optics up to 750 mm × 1000 mm.
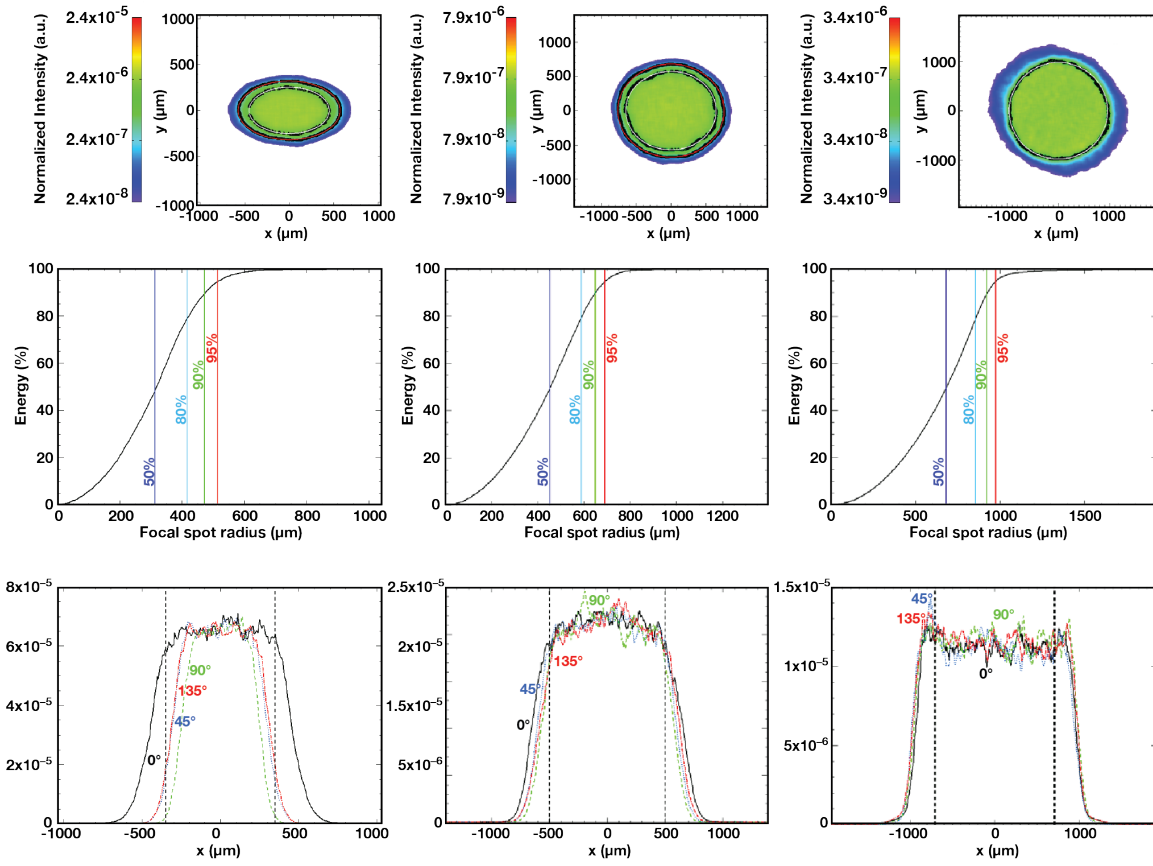
Fig. 32: Typical large-aperture CPPs manufactured and tested at LLNL. 50°outer cone implosion CPP (left), 23°inner cone implosion CPP (center), and 2 mm far-field spot illuminator CPP (right). Far-field representations are smoothed using a moving boxcar average filter over 100 microns. Refer to Table VII for details.
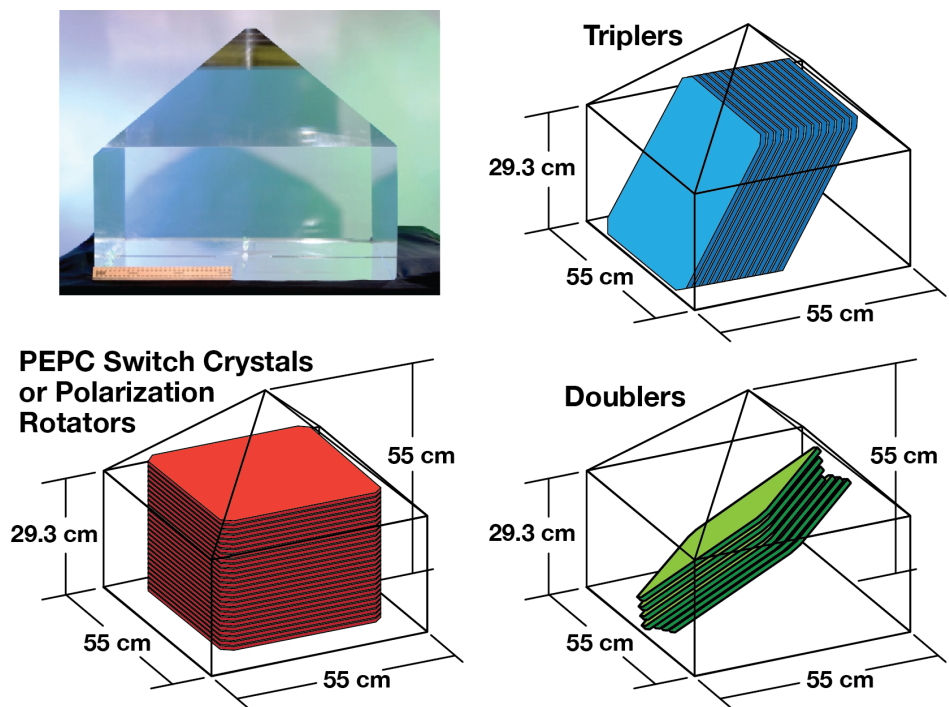
Fig. 33: Orientation of finished NIF crystal optics relative to their parent single-crystal boule.
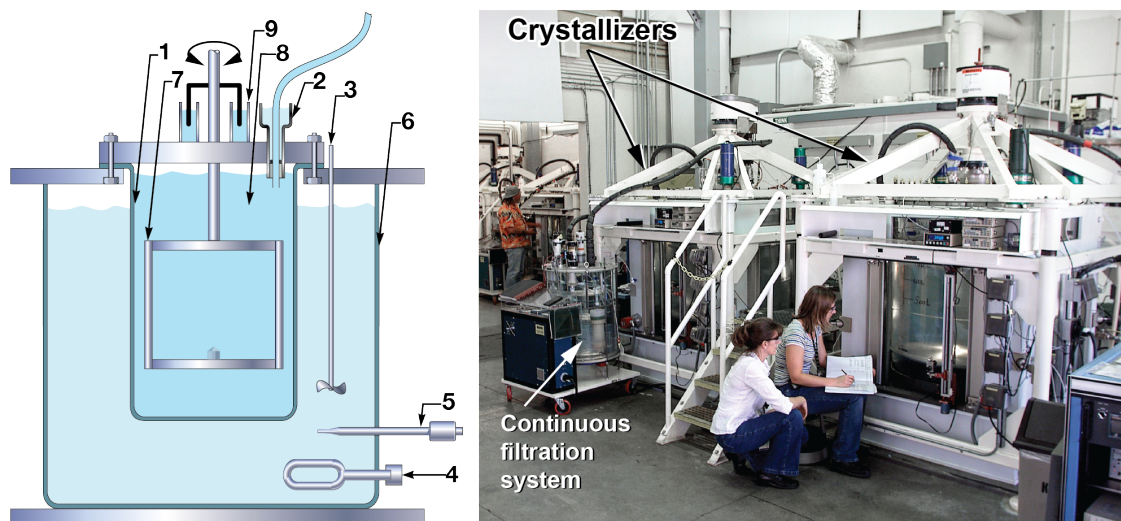
Fig. 34: (left) General schematic of a crystallizer used for rapid crystal growth: (1) growth tank; (2) water-cup seal, used to transport growth solution to and from the external continuous filtration system; (3) stirrer, used to maintain temperature uniformity of the external water bath; (4) heater; (5) thermocouple used as an element of a temperature control loop; (6) external water bath; (7) platform with the seed; (8) growth solution; (9) water-cup seal. (right) 1000-L rapid-growth crystallizers at LLNL.
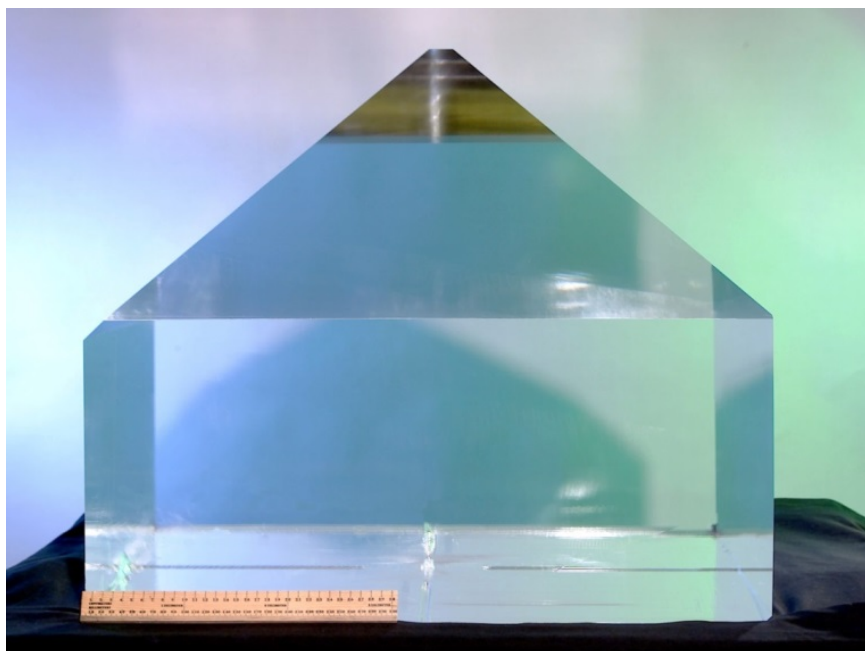
Fig. 35: Single crystal KDP boule harvested in January 2001. At that time, this was the largest

rapid-growth KDP boule produced, with an estimated yield of 14 SHG optics.
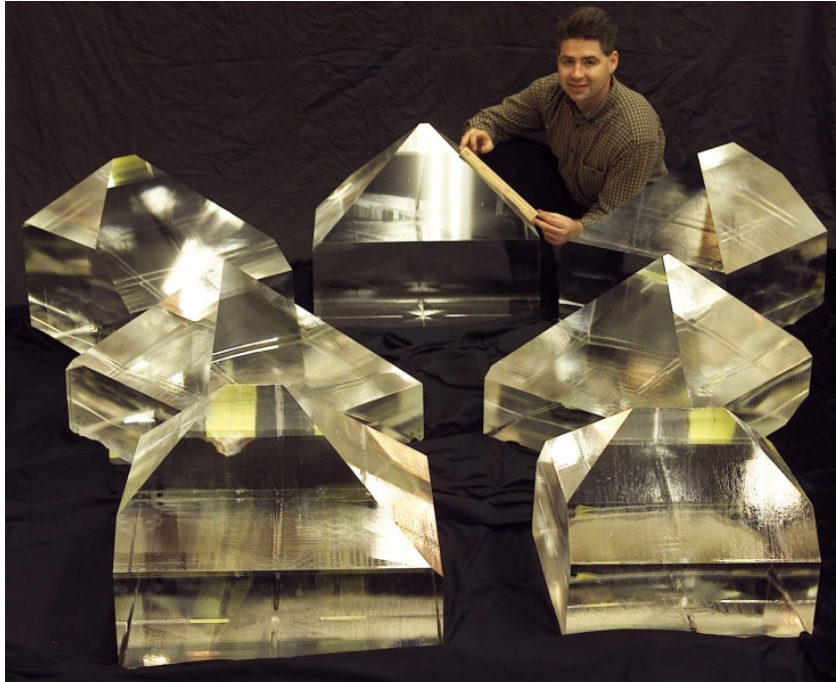
Fig. 36: Large KDP crystals awaiting further cutting and finishing for use as switch crystals,

polarization rotators, or frequency doublers in NIF.
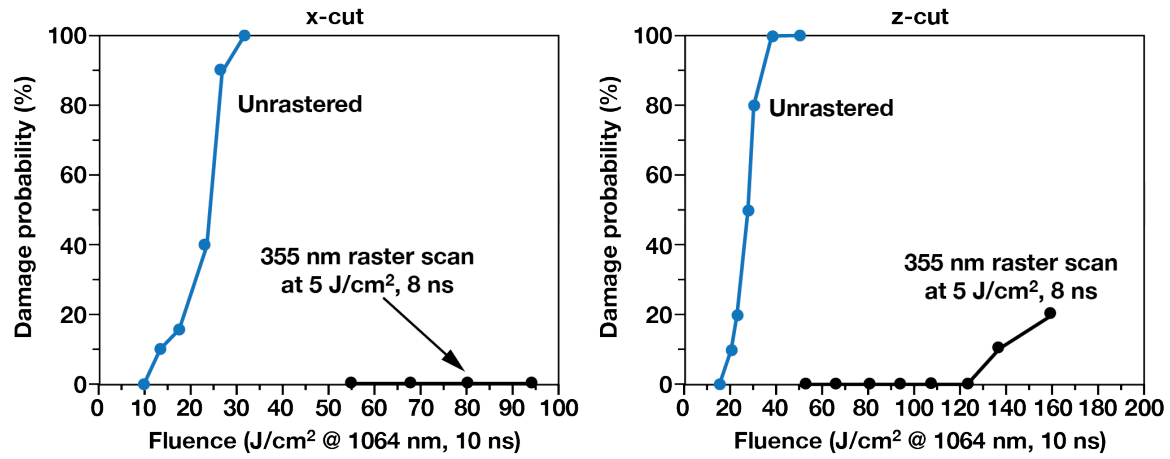
Fig. 37: Plot of the change to the 1ω (1064 nm (10 ns)) S/1 damage probability of x-(left) and z-cut (right) rapid growth DKDP crystals before and after raster scanning at 5 J/cm^2 at 3ω (355 nm, 8 ns). Damage onset for the z-cut PEPC switch crystal after raster conditioning exceeds 120 J/cm^2 at 1064 nm, 10 ns.[160]
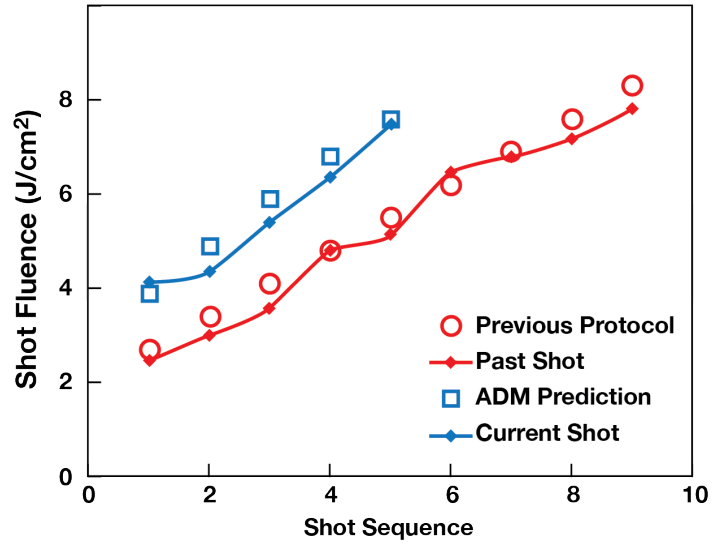
Fig. 38: Comparison of candidate on-line conditioning protocols for NIF. (In red) Baseline 9-shot protocol; (In blue) Improved 5-shot protocol guided by ADM.[174]
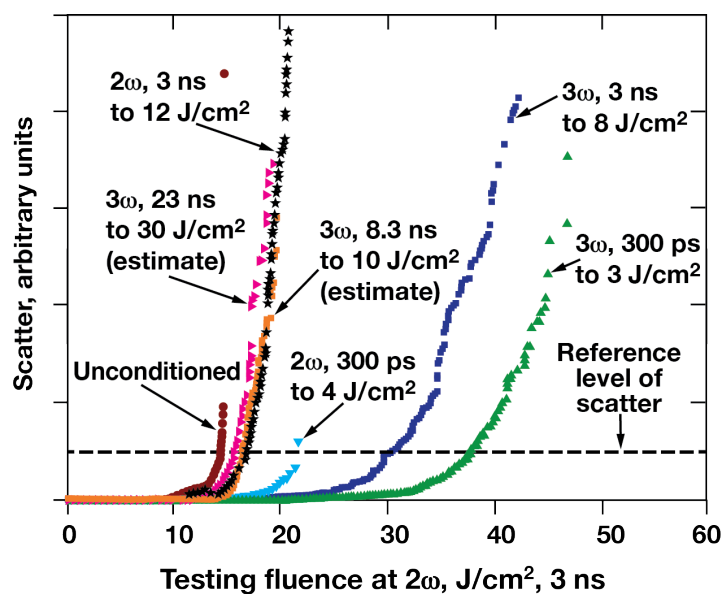
Fig. 39: Ordered pairs of scatter vs. damaging fluence for 2ω 3 ns test pulses. Different regions of doubler cut KDP had previously been conditioned at either 2ω or 3ω, using the pulse durations defined in the graphic. Smaller scatter values are indicative of better conditioning. Note that conditioning wavelength and pulse duration are both important for increasing the damage resistance of doubler material. See Ref. 175 for details of the conditioning and testing procedures.
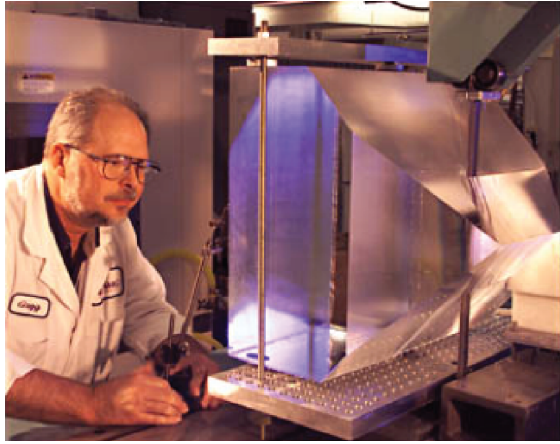
Fig. 40: Bandsaw cutting of a large KDP single-crystal boule.
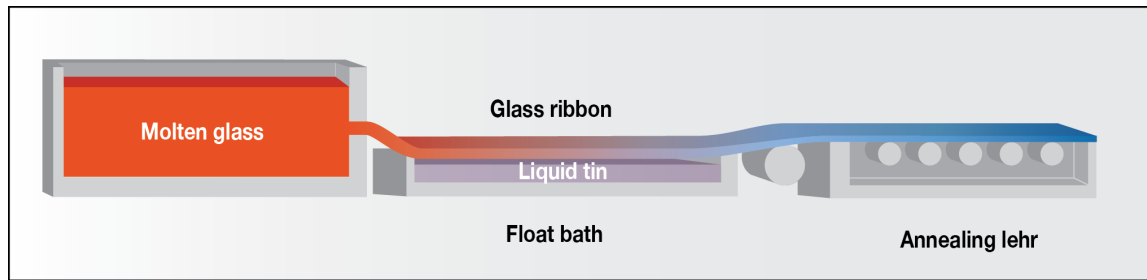
Fig. 41: Borofloat® 33 glass is produced using Schott's unique Microfloat process.[189]

Fig. 42: Class 100 cleanroom DDS production facility.
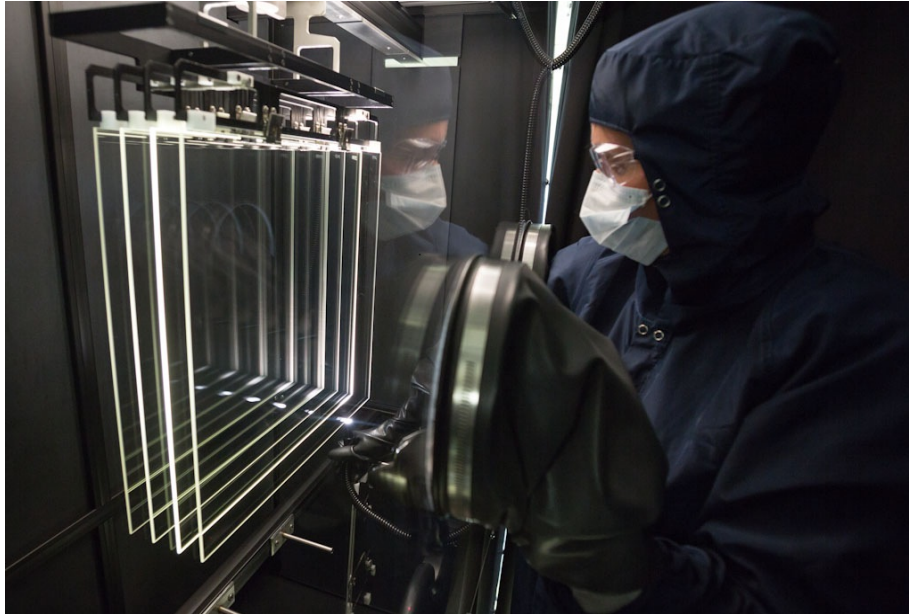
Fig. 43: Inspection of DDS for coating defects.
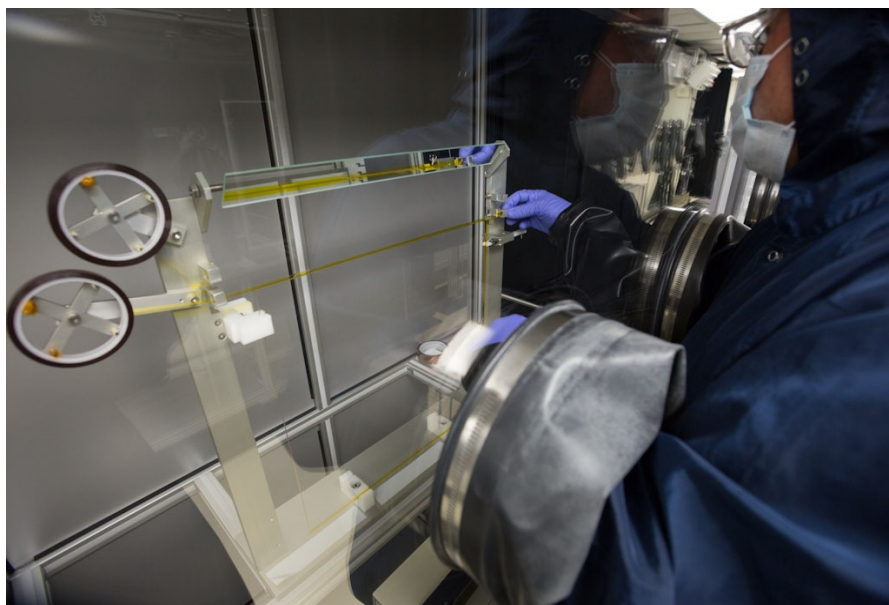
Fig. 44: Kapton® tape application around the DDS.

TABLES

TABLE I: Summary of the optic types, number needed for the 192 beamlines of the NIF, and

key materials used for fabrication. (Wavelength 1ω = 1053 nm and 3ω = 351 nm)

Optic Type	Number Required		Key Material(s)
	1ω	3ω	
Amplifier slabs[a]	3072	0	Nd-doped phosphate glass
Mirrors[b] and polarizers	1600	0	BK7 glass with hafnia-silica (HfO_2/SiO_2) dielectric coating
Lenses, windows, and diffractive optics	1536	576	Fused silica (SiO_2)
Crystals[c]	288	384	Potassium di-hydrogen phosphate (KDP) and deuterated KDP (DKDP)
Disposable debris shields	0	192	Borofloat® 33 glass
Subtotal	6496	1152	
Total	7648		

a – Using the 11/5 amplifier configuration
b – LM6 mirror are only installed on 64 beamlines
c – Polarization rotation crystals are only installed on half the NIF beams

TABLE II: The main suite of metrology tools used to support the production of NIF large optics.

Instrument	Method	Aperture	Measurement	Measurement Definitions or Features
24-in. interferometer	Fizeau interferometry	Full	TWF	2.5 mm–40 cm spatial frequency, peak-to-valley (P-V), transmitted or reflected wavefront (TWF or RWF), rms gradient, power, spectral density (PSD-1).
			RWF	
			PSD-1	
			Homogeneity	ppm sensitivity
			Lens figure	Uses 62 cm interchangeable null optics (calibration spheres).
Crystal Alignment Test System (CATS)	Frequency conversion	Sub	Frequency conversion rocking curves	Microradian-scale determination of frequency conversion curves of SHG and THG crystals relative to proof crystals.
Micro-PMI	White light interferometry	Sub	PSD-2 and Roughness	0.01–2.5 mm spatial frequency, power spectral density (PSD-2 and Roughness).
Edge Light Verification (ELV)	Scatter	Full	TIR scatter by defects	Defect detection by imaging scatter from Total Internal Reflection (TIR) laser light injected through edges of part.
Phase Shifting Diffraction Interferometer (PSDI)	Interferometry	Sub	Phase	Measures phase perturbations from phase defects in bulk materials or coatings. Phase maps used to calculate local downstream beam intensity and fratricide probability.
Line-scan Image Mapping System (Line-scan IMS)	Darkfield imaging	Full	Bulk and surface defects on transmissive optics	Rapid screening of optics for objects requiring higher resolution measurement with PSDI.
Dig Inspection System (DIS)	Bright field microscopy	Sub	Surface defects	Measures size defects up to 1 cm. Primarily used for mechanical dig characterization on frequency conversion crystals.
Modulation Measurement System (MMS)	Diffraction	Sub	Bulk and surface defects on transmissive optics	Measures downstream intensification of diffraction patterns from bulk and surface defects up to 1 cm diameter.
View microscope	Microscopy	Sub	High-resolution microscopy	Automated, high-resolution, stitching microcopy for full-aperture bulk or surface-defect counting and classification.
Automated Disposable Debris Shield (ADDS-View)	Confocal microscopy	Full	mm-scale surface height	Measures surface curvature of disposable debris shield (DDS) glass with submicron resolution over a range of 1 mm.
Coordinate Measuring Machine (CMM) Arm	Contact profilometry	Full	Mechanical surface profile	Measures surface profile of focus lens during intermediate processing.
Bauer Photometer	Laser ratiometry	Full	Scanning small beam	Scanning system at 1053-, 527-, 351-nm transmission and reflection of mirrors from 0–70 degrees.
Broadband Spectrometer	UV-Vis Spectroscopy	Coating witness sample	Spectral	Reflectivity or transmission of coatings as a function of wavelength.
Slab Inspection	Haidinger	Full	Large-scale	Measures cm-scale phase defects on

System (SIS)	interferometry		defects	laser glass slabs.
Inclusion Mapping System (IMS)	Laser scatterometry	Full, scanning	Micron-scale bulk inclusions	Automated system measures micron-scale bulk inclusion in fused silica blanks.
Lens Optical Test System (LOTS)	Fizeau interferometry	Full	TWF	Measure lens focal length using calibration spheres.
Ellipsometer	Ellipsometry	Sub	Polarization change	Measures coating thickness and refractive index using elliptically polarized light.
Diffractive Optic Full-Aperture System Test (DOFAST)	Laser ratiometry	Full	Diffraction grating efficiency	Measures efficiency and uniformity of first order diffraction from grating debris shield (GDS).
DOFAST DDS	Laser ratiometry	Full	Transmission	Measures 351-nm transmission of the disposable debris shield (DDS).

TABLE III: A subset of measurements performed on various optic types by each metrology system. Measurements are shown as shaded boxes in the table. The abbreviation LGA in the table refers to Laser Glass Amplifiers. Other abbreviations for the various optics types are given in Fig. 1 and Appendix A.

Measurement/ Tool	Optic Type									
	LGA	LM/ PL	DBS	SC	SW/ TCVW	CPP	SHG/ THG	SF/ WFL	GDS	DDS
TWF & rms gradient/ Interferometry	▓	PL only	▓	▓	▓	▓	▓	▓	▓	
RWF & rms gradient/ Interferometry		▓	▓							
PSD-1/ Interferometry	▓	▓	▓	▓	▓	▓	▓	▓	▓	
Homogeneity/ Interferometry	▓	▓			▓			▓		
PSD-2 and Roughness (Micro-PMI)	▓	▓	▓	▓			▓			
Conversion crystal tuning/CATS							▓			
Damage detection/ ELV					TCVW only	▓	▓	WFL only	▓	
Damage characterization/ PSDI					TCVW only			WFL only		
Damage detection/ line-scan IMS					TCVW only			WFL only		
Damage characterization/DIS				▓			▓			
Bulk damage density/ view microscope				▓		▓	▓	▓	▓	
DDS sag/ ADDS-View										▓
LM coating reflection & transmission/photometer		▓								
LM coating reflection & transmission/spectrometer		LM only								▓
Laser glass surface profile/SIS	▓									
Focus lens surface profile/CMM arm								WFL only		
Surface defect mapping/IMS					TCVW only	▓	▓	▓	▓	
Lens focal length/LOTS								▓		
Sol-gel coating thickness/ellipsometer			▓	▓	▓	▓	▓	▓	▓	
GDS efficiency/DOFAST									▓	
DDS transmission/ DOFAST DDS										▓
Laser glass damage testing/ LGDT	▓									
Laser conditioning/LAC		▓								

TABLE IV: Reliability data for the high-volume metrology and QA tools from October 2004 through March 2009. Detailed availability data was obtained only for the seven Wyko 24-in interferometers maintained by LLNL. Zygo was responsible for maintenance of the three 24-in and two 18-in Zygo interferometers and equivalent data is not available.

System	Number	Total days	Fully Available	Conditional	Unavailable
24-in. interferometer	7	6370	96.5%	2.3%	1.2%
CATS	1	910	84.8%	7.3%	7.9%
LACS	4	3048	86.7%	7%	6.3%
LGDT	2	1370	93.7%	—	6.3%

TABLE V: Composition given in mol% and properties of Nd-doped phosphate laser glasses LHG-8 and LG-770 (from Ref. 36 with permission).

Composition[a] or property	LHG-8	LG-770
P_2O_5	55–60	58-62
Al_2O_3	3–12	6–10
K_2O	13–17	20–25
BaO	—	—
MgO	0–2	0–2
Nd_2O_2*	<2	<2
OIP (±0.1)	3	3
Optical		
Refractive index[c]		
n_4 (587.3 nm)	1.5296	1.5067
m (1053 nm)	1.5201	1.4991
Non-linear refractive index		
n_2 (10^{-33} esu)	1.12	1.01
γ (10^{-23} m²/W)	3.08	2.78
Abbe number (±0.05)	66.5	68.4
Laser		
Emission cross-section (10^{-29} cm²)(±0.2)	3.6	3.9
Radiative lifetime (zero–Nd)(µs)(±3)	365	372
Judd-Ofelt radiative lifetime (µs)(±10%)	351	349
Emissionband width (nm)(±0.1)	26.5	25.4
Thermal		
Thermal conductivity, 90°C (W/mK)(±0.03)	0.58	0.57
Thermal diffusivity (10^{-7} m²/s)	2.7	2.9
Specific heat, Cp (J/gK)(±0.02)	0.75	0.77
Coeff. thermal expansion, 20–300°C (10^{-7}/K)(±3)	127	134
Glass transition temperature[c], T_5 (°C)(±5)	485	460
Mechanical		
Density (g/cm³)c (±0.01)	2.83	2.59
Poisson's ratio (±0.01)	0.26	0.25
Fracturetoughness (MPa m$^{1/2}$)(±0.02)	0.51	0.43
Hardness (GPa)(±0.10)	3.43	3.58
Young's modulus (GPa)(±1.0)	50.1	47.3

[a]Range in composition values reflect variations due to Nd-doping concentration, melt volatility, & batching variations.

[b]Nd-dopeing levels typically <2 mol% Nd_2O_3 (<5 x 10^{20} Nd ions/cm³); the NIF and LMJ use a doping of 4.2 (±0.1) x 10^{20} ions/cm³

[c]Values may vary slightly with Nd-doping level

TABLE VI. Transmissive fused silica optical elements required for NIF construction.

(Wavelength 1ω = 1053 nm, 2ω = 527 nm, and 3ω = 351 nm)

Optic	Number per beamline	Total Required	Wavelength	Vacuum barrier
PEPC switch window (SW)	2	384	1ω	Yes
Cavity spatial filter lens (CSF)	2	384	1ω	Yes
Transport spatial filter lens (TSF)	2	384	1ω	Yes
Diagnostic beam splitter (DBS)	1	192	1ω	No
Target chamber vacuum window (TCVW)	1	192	1ω	Yes
Continuous phase plate (CPP)	1	192	1ω or 2ω	No
Off-axis wedged focus lens (WFL)	1	192	3ω	No
Grating debris shield (GDS)	1	192	2ω	Yes

TABLE VII: Typical indirect drive ICF CPP performance parameters versus specification for large-aperture CPPs manufactured using MRF.

Parameter	Specification	Measured	Pass/Fail
50-degree outer cone implosion CPP			
80% Encircled Energy Radius (µm)	421.0 ± 15.0	421.8	PASS
90% Encircled Energy Radius (µm)	472.0 ± 15.0	476.2	PASS
95% Encircled Energy Radius (µm)	515.0 ± 15.0	520.8	PASS
Individual Lineout RMS Deviation (%)	5.0	4.2	PASS
2-D RMS Deviation over Central Area (%)	5.0	4.5	PASS
50 % Eccentricity (a = 451.2, b = 252.4)	0.56 ± 0.1	0.56	PASS
23-degree inner cone implosion CPP			
80% Encircled Energy Radius (µm)	594.0 ± 15.0	592.3	PASS
90% Encircled Energy Radius (µm)	652.0 ± 15.0	651.2	PASS
95% Encircled Energy Radius (µm)	696.0 ± 15.0	696.2	PASS
Individual Lineout RMS Deviation (%)	7.0	5.9	PASS
2-D RMS Deviation over Central Area (%)	5.0	4.7	PASS
50% Eccentricity (a = 451.2, b = 252.4)	0.88 ± 0.1	0.88	PASS
2-mm far-field spot illuminator CPP			
80% Encircled Energy Radius (µm)	860.0 ± 15.0	860.0	PASS
90% Encircled Energy Radius (µm)	923.0 ± 15.0	925.4	PASS
95% Encircled Energy Radius (µm)	976.0 ± 15.0	977.1	PASS
Individual Lineout RMS Deviation (%)	6.5	5.6	PASS
2-D RMS Deviation over Central Area (%)	6.5	5.7	PASS
50% Eccentricity (a = 451.2, b = 252.4)	1.02 ± 0.1	1.02	PASS